State Estimation And Control Of Spray Etching Processes.

INFORMATION TO USERS

This manuscript has been reproduced from the microfilm master. UMI films the text directly from the original or copy submitted. Thus, some thesis and dissertation copies are in typewriter face, while others may be from any type of computer printer.

The quality of this reproduction is dependent upon the quality of the copy submitted. Broken or indistinct print, colored or poor quality illustrations and photographs, print bleedthrough, substandard margins, and improper alignment can adversely affect reproduction.

In the unlikely event that the author did not send UMI a complete manuscript and there are missing pages, these will be noted. Also, if unauthorized copyright material had to be removed, a note will indicate the deletion.

Oversize materials (e.g., maps, drawings, charts) are reproduced by sectioning the original, beginning at the upper left-hand corner and continuing from left to right in equal sections with small overlaps. Each original is also photographed in one exposure and is included in reduced form at the back of the book.

Photographs included in the original manuscript have been reproduced xerographically in this copy. Higher quality 6" x 9" black and white photographic prints are available for any photographs or illustrations appearing in this copy for an additional charge. Contact UMI directly to order.

UMI

University Microfilms International
A Bell & Howell Information Company
300 North Zeeb Road, Ann Arbor, MI 48106-1346 USA
313 761-4700 800 521-0600

Order Number 9207016

State estimation and control of spray etching processes

Kao, Alan S., Ph.D.

Lehigh University, 1991

U·M·I

300 N. Zeeb Rd.
Ann Arbor, MI 48106

STATE ESTIMATION AND CONTROL OF SPRAY ETCHING PROCESSES

by

Alan S. Kao

PhD Dissertation
Department of Chemical Engineering
Lehigh University

September 1991

STATE ESTIMATION AND CONTROL OF SPRAY ETCHING PROCESSES

by

Alan S. Kao

A Dissertation Presented to the Graduate Committee of Lehigh University in Candidacy for the Degree of Doctor of Philosophy in Chemical Engineering

Department of Chemical Engineering
Lehigh University

September 1991

This is a blank page

CERTIFICATE OF APPROVAL

Approved and recommended for acceptance as a dissertation in partial fulfillment of the requirements for the degree of Doctor of Philosophy.

Date: 9-10-91

Dr. Harvey G. Stenger, Jr.
Co-Advisor, Chemical Engineering

Dr. Christos Georgakis
Co-Advisor, Chemical Engineering

Dr. Hugo S. Caram
Chemical Engineering

Dr. Richard D. Granata
Chemistry

Dr. Cesar A. Silebi
Chemical Engineering

This is a blank page

ACKNOWLEDGEMENTS

I am grateful to my research advisors, Harvey Stenger and Christos Georgakis, for their continued support and advice. I would also like to thank the members of my committee, Hugo Caram, Cesar Silebi, and Rich Granata, for their interest and helpful comments.

I am grateful to Kathy Covert and John Kurowski from IBM, Endicott. Their assistance during the experimental work and their input throughout my association with IBM have been a tremendous help towards the completion of my graduate work. I'd also like to acknowledge the IBM Corporation for their financial support of my graduate work.

For all of their help with administrative matters and the seemingly endless bouts with the photocopy and fax machines, I thank Carol Biuckie, Shirley Matlock, Barbara Scherer, Pat Conklin, and Carole Marder.

I am indebted (but not in debt) to the Tally Ho, especially to Melissa Snoey and Maggie Hoffert, for being the latter half of "working hard and playing hard".

There are many friends whom I have made during my stay here in Bethlehem, and they are the reason I was able to complete my degree at Lehigh without becoming a complete cynic. I cannot thank them all in the limited space of these pages, but there are a few in particular I'd like to mention. Thanks to

Jim and Jill Bartee, the couple of many musical tastes; Rick and Sharon Goetz, the guardians of Tlaquepaque; Brett Budis, the angry mutant from New Jersey; Lori Fortin, DJ extrordinaire; Yiannis Dimitratos, for his many wonderful ideas; Stefano Carra, for convincing me that soccer is a very average (pronounced *AY-verage*) sport and far more boring than football; and Jai Venkatesan, who I never got to fully appreciate rap music, but who was responsible for many memorable porch parties and good times.

Finally, I am grateful to my parents. For their love, their patience, their support, and for giving birth to me.

Peace.

Mutate, don't stagnate.

---- M. Mothersbaugh

This is a blank page

To my parents

This is a blank page

CONTENTS

ABSTRACT

An investigation to develop a better understanding of the fundamentals behind the operation of spray etching processes revealed several interesting phenomena that explain some of the difficulties encountered during operation. Higher spray pressures are required for the top sides than for the bottom sides in order to achieve equal amounts of etching on each side of the boards being processed. This is due to additional mass transfer limitations that are created when puddles of liquid collect on the top side of the boards.

Another phenomenon observed was an increase in the etch angle, resulting in more vertical sidewalls, as the extent of etch undercut increases. This is believed to be due to the formation of weak recirculating eddies underneath the mask, which inhibit mass transport at the top of the line and allow the bottom line width to "catch up" with the top line width. Therefore, vertical lines can be achieved by overdesigning the mask line widths, but at the expense of line spacing.

The control objectives of the process are to etch a certain bottom line width on both sides of the panels for any board type entering the etch line. Since measurements of the line widths are not available at a rate that is frequent enough to design a sampled-data control system, a process model was developed around which a control system is based. To account for modeling

errors, unmodeled process disturbances, and measurement noise, this deterministic model was combined with a stochastic representation of the poorly known or unknown states and parameters. This was then used to design a Kalman filter for state estimation that combined the process model, all available measurements (regardless of precision or frequency), and information on the state probability distribution.

Several Kalman filter designs were developed and tested with a model developed for the process. A hybrid extended Kalman filter was found to yield biased estimates in the presence of process-model mismatch. This issue was resolved by augmenting the state vector with poorly known parameters and developing a proportional-integral Kalman filter. The same technique was used to develop a reduced order Kalman filter, which treated the bulk tank concentrations as stochastic processes. The resulting filter designs are capable of providing accurate estimates of the etching species concentrations as well as making available frequent estimates of the etch profile characteristics, which are only measured at infrequent intervals. Based on the Kalman filter, a multivariable control strategy was "implemented" on the process model. The control system was able to maintain line widths at a 100 μm setpoint within ±2 μm.

CHAPTER

ONE

INTRODUCTION

1.1 PROBLEM STATEMENT

Despite the widespread use of etching reactors (both wet and dry) throughout the electronics industry, there is still an incomplete understanding of the technology's fundamentals. Thus the operation and design of etching equipment have been heavily empirical. Any attempt to address the demand for improved and more consistent etching performance with tighter geometric tolerances in printed circuit board production will require a better understanding of the fundamentals behind the manufacturing processes. Performance issues to be addressed include determining how the existing equipment and technology can be used to achieve fine line etching with narrower spaces and more vertical wall angles.

Spray etching is the primary means of subtractive circuitization presently used. During the operation of spray etchers, control decisions are made on-line by operators, who periodically examine the quality of a board as it is removed from the etch line. Depending on the quality of the inspected product, adjustments are made to the operating conditions of the etchers according to

rules such as those shown in Table 1. As to the degree of the changes (how much is "↑"?) and the need for changes (for instance, how high is "high"?), this is generally left up to the operators. In fact, the operators may choose to ignore this list of rules completely, electing to follow rules of their own that they have found to give satisfactory production results.

Table 1. Typical Rules For Spray Etcher Operation

BLW (top side)	*BLW* (bottom)	Current *TSP*	Δu_{con}	ΔTSP	ΔBSP
good	good	max	same	same	same
good	good	not max	↑	↑	↑
good	high	max	same	same	↑
good	high	not max	↑	↑	↑↑
good	low	max	same	same	↓
good	low	not max	↑	↑	↓
high	good	max	↓	same	↓
high	good	not max	same	↑	same
high	high	max	↓	same	↓
high	high	not max	same	↑	same
high	low	max	↓	same	↓↓
high	low	not max	same	↑	↓
low	good	max	↑	same	↑
low	good	not max	↑↑	↑	↑↑
low	high	max	↑	same	↑↑
low	high	not max	↑↑	↑	↑↑↑
low	low	max	↑	same	same
low	low	not max	↑↑	↑	↑

Before processing a different product, test panels are often used to determine whether the operating parameters are in need of adjustment before beginning a new job. These boards are subsequently discarded as scrap panels. Different rules and initial settings may have been determined for different product types. Thus much of the decision-making, both during the processing of

a job and between jobs, is left to heuristics and intuition. This intuition cannot be systematically transferred from one operator to another; it can only be developed with time and experience.

Modern printed circuit boards are designed to contain an ever increasing number of contacts and conductors on a limited board area, thus requiring much tighter geometric tolerances. As the trend toward producing smaller line widths with narrower line spacings on printed circuit boards continues, the ability to control the wet etching process becomes extremely important. While the current operating procedures have yielded products of acceptable quality and throughput in the past, there is a drive to further improve consistency and reduce the quantity of discarded scrap panels. This reliance on intuition for etcher operation will not result in satisfactory production yields for the newer products. Being able to control etching behavior requires an understanding of the fundamental mechanisms by which etching occurs.

A more complete understanding of the processes involved in the etching of printed circuit boards will help in:

- designing improved control techniques for the process,
- deciding how products manufactured with these reactors can be improved and if the existing equipment is capable of accomplishing these improvements,
- exploring what new products the existing equipment might be able to produce, and
- understanding how the present equipment could be better designed in the future.

1.2 THE CONCEPT OF "INTELLIGENT" CONTROL

Initial evaluation of this problem of needing to achieve consistent etcher performance regardless of the experience of the operators indicated that this would be an ideal application of knowledge-based or "expert" systems (Winston, 1984, Frost, 1986). Expert systems "capture" the expertise of the operators in the form of rules rather than formal mathematics. They are then able to draw from this knowledge base and make "intelligent" control decisions. Several successful applications of expert systems have been reported, including control of cement kilns (Umbers and King, 1980), traffic junction control (Pappis and Mamdani, 1977), activated sludge wastewater treatment (Tong *et al.*, 1980), space station automation (Biglari *et al.*, 1988), and flight control (Handelman and Stengel, 1988).

The majority of expert system applications involve making a decision from a variety of choices. Presented with a situation that requires a decision, the expert system will use past history and heuristics to determine what choice to make or what additional information to obtain before making a decision. This type of "automated reasoning" is ideally suited for fault diagnosis and troubleshooting.

In situations where more precise control is critical, the "fuzzy" behavior of expert systems may not be appropriate. For these systems, improved control can be achieved through a better understanding of the fundamentals behind the process. From this analysis, a process model can be developed that describes the dynamic behavior of the states of the system. Control of these states is achieved through the monitoring of available measurements, which generally have a degree of noise associated with them. Techniques have been developed for using these noise-corrupted measurements coupled with the best model available for the process in order to determine the "best" estimates of the states

(Gelb *et al.*, 1974, Stengel, 1986). By comparing actual measurements with estimates of the measurements based on the state estimates, the residual is used to improve the estimates. Thus the system begins to "learn" the states, which allows more "intelligent" control of the process.

1.3 STOCHASTIC MODELS, ESTIMATION, AND CONTROL

Processes can generally be described in either a *deterministic* or a *stochastic* sense. Deterministic systems are characterized by a mathematical model, usually in the time domain, that describes the dynamic behavior of the process. This model uses fundamental principles, physical insights, and empirical testing to establish interrelationships between the states of interest, inputs to the system, and outputs from the system. Based on this model and measurement devices for the output variables, decisions can be made determining how the inputs are to be manipulated in order to achieve a desired system response.

Stochastic models address the issue of state variability by representing the states of interest as random processes. Thus, characterization of a system involves not only a mathematical description of the dynamics of the states, but also information about the state probability distribution dynamics. So whereas a deterministic model is only represented by the first central moment, or the *mean* of the process states, a stochastic model is additionally characterized by the second central moment, or the *covariance*, which gives an indication of the spread of the values of the states about the mean.

Useful stochastic models require more effort to develop than do deterministic models. The additional effort is justified in most cases for several reasons (Maybeck, 1979). First of all, deterministic models are never perfect

representations of reality. They generally only depict the characteristics of direct interest to the engineer's purpose and often involve assumptions and simplifications that are necessary to make the model mathematically manageable or to account for unknown local behavior. A second shortcoming of deterministic models is the effect of unmodeled disturbances to the system. Lastly, when basing a control system on a deterministic model, the engineer may be restricted by sensors that provide imperfect (noisy) and incomplete data about the system. These difficulties can be overcome through the enhancement of the deterministic model with a stochastic model and state estimation techniques. The application of these state estimation techniques towards the improved operation and control of spray etching processes is the focus of this work.

1.4 REFERENCES

Biglari, H., C. Cheng, and G. Vachtsevanos, "Fault Tolerant Intelligent Controller for Space Station Subsystems", *Proc. 7th Amer. Contr. Conf.*, **1**, 247 (1988).

Frost, R., *Introduction to Knowledge Base Systems*, Macmillan, New York (1986).

Gelb, A., J. F. Kasper, R. A. Nash, C. F. Price, and A. A. Sutherland, *Applied Optimal Estimation*, MIT Press, Cambirdge, MA (1974).

Handelman, D. A. and R. F. Stengel, "Rule-Based Mechanisms of Learning for Intelligent Adaptive Flight Control", *Proc. 7th Amer. Contr. Conf.*, **1**, 208 (1988).

Maybeck, P. S., *Stochastic Models, Estimation, and Control: Volume 1*, Academic Press, New York (1979).

Pappis, C. P. and E. H. Mamdani, "A Fuzzy Logic Controller for a Traffic Junction", *IEEE Trans. Systems, Man, and Cybernetics*, **SMC-7**, 707 (1977).

Stengel, R. F., *Stochastic Optimal Control*, John Wiley & Sons, New York (1986).

Tong, R. M., M. B. Beck, and A. Latten, "Fuzzy Control of the Activated Sludge Wastewater Treatment Process", *Automatica*, **16**, 659 (1980).

Umbers, I. G. and P. J. King, "An Analysis of Human Decision Making in Cement Kiln Control and the Implications for Automation", *Internat. J. Man-Machine Stud.*, **12**, 11 (1980).

Winston, P. H., *Artificial Intelligence*, 2nd ed., Addison-Wesley, Reading, MA (1984).

CHAPTER

TWO

LOCAL MODELING OF ETCH PROFILES

2.1 PRINTED CIRCUIT BOARD MANUFACTURE

The manufacture of an integrated circuit (IC) or a printed circuit board (PCB) involves a series of chemical process steps, one of which is the removal or *subtractive etching* of a conductor to achieve a desired circuit pattern. The steps immediately preceding etching are:

- applying a coat of photoresist over the surface of an insulating, conducting, or semiconducting film,
- exposing the photoresist to ultraviolet light through a prefabricated mask, which imprints the desired pattern on the resist,
- developing and removing the unexposed resist, which leaves the unwanted material exposed, while the pattern is protected by the photoresist.

This particular process, where the pattern is printed on the board and the unwanted copper is etched away, is a subtractive process known as "print and etch", and is one of the simplest and most commonly used processes used for PCB fabrication (Datta and Romankiw, 1989). The etching is generally accomplished through wet chemical methods, which offer high throughput, low

cost, and high reliability. The metals used for electronic applications include steel, Ni-Fe alloys, copper alloys, and most commonly, copper. Since wet etching techniques often suffer from the problem of isotropic etching, they are generally not used for pattern definition when working with the feature sizes associated with IC production (Schnorr, 1969). For PCB production, the principal method used presently is *spray etching*. Some older technologies used in practice are immersion etching, bubble etching, and splash etching (Duffek and Armstrong, 1979).

Immersion etching, the simplest of the four methods, refers to batch-type reactors filled with etchant solution into which circuit panels are immersed until the etching is complete. Etch rate is enhanced by heating or agitating the solution; however, these techniques still require long process times to achieve the desired amount of etching.

Bubble etchers involve the same type of batch reactors, but with a stream of air being bubbled through the solution. The flow of air aids the circulation of fresh etchant throughout the tank. Additionally, oxygen from the air causes partial etchant regeneration to occur in the reactor, thus increasing the efficiency of the etchant solution. Boards processed by bubble or immersion etchers generally suffer from severe undercutting due to the long contact times of the board with the etching solution. Also, by using batch processes, the effectiveness of the etchant solution decreases with each batch. Therefore the solution must be changed periodically, adding considerable process down time.

In splash or paddle etching, boards are supported vertically while the etchant solution is splashed onto the boards. Paddles or cups attached to a motor driven shaft are used to transport the etchant from a solution reservoir to the boards. Splash etching etches more evenly and minimizes undercut, but can only handle a few boards at a time.

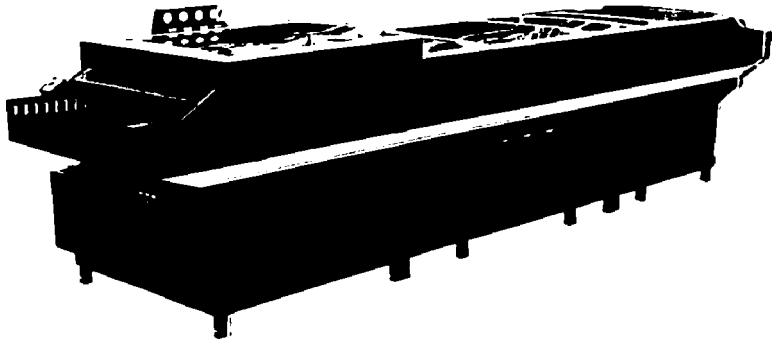

Figure 2.1: Photograph of a horizontal spray etching reactor.
Courtesy of Chemcut

The most commonly used technique is spray etching. A spray etcher consists of an etch chamber and a sump tank, as shown in Figure 2.1. The boards are placed on a conveyer and the etchant is sprayed onto their surfaces as they proceed through the etch chamber. The etchant solution is drawn from the sump tank, which continually receives the overflow from the etch chamber. Spray etchers can be operated with the boards supported either horizontally or vertically and by spraying either one or both sides of the boards. Since spray etchers can keep a fresh supply of etchant on the board surface at all times, more consistent etch rates are possible than with immersion etching reactors. This type of process offers improved etch quality, shorter etching times, and thus, higher throughput.

2.2 PREVIOUS WORK

Several investigators have developed mathematical models for the shape evolution of small dissolving cavities based on fundamental principles of transport and reaction phenomena. These investigations have practical applications in a variety of fields other than the etching of masked device surfaces. These include pitting corrosion, electrochemical machining, and electropolishing.

Alkire *et al.* (1984) studied the effect of fluid flow on mass transfer within small cavities dissolving at high rates. They recognized that the evolution of cavity shape would involve a change in the controlling transport surface. Their work showed that in the early stages of cavity formation, the rate of dissolution is dependent on mass transport by diffusion; however, as the depth increases, a circulating eddy develops in the cavity. The velocity of this eddy will increase as the size of the cavity grows, thereby increasing mass transport by convection to the point where it predominates over diffusion.

Kuiken *et al.* (1986) presented a perturbation solution for the diffusion-controlled etching of a semi-infinite solid partly covered by a protecting photoresist mask. They showed etch rates to be largest close to the mask edge, resulting in a bulging shape in that region. Alkire and Deligianni (1988) experimentally investigated the effect of hydrodynamic conditions on the ability to achieve anisotropic etching. They found the final shape of the etch cavities to be strongly dependent on the aspect ratio, defined as the ratio of the cavity depth to width. Shallow cavities were observed to yield less undercut and more vertical etch angles than narrow cavities. Shin and Economou (1989) examined shape evolution under the combined effects of fluid flow and mass transfer. Their model assumes first order kinetics for the etching reaction. They observed a fourfold increase in etch rate in the presence of fluid flow over the pure

diffusion process. In addition, the etch rate, etch anisotropy, and etch angle showed a strong dependence on etch time as the aspect ratio increased with time during etching.

For all of these cases except that of Kuiken *et al.* (1986), the models are solved via finite element techniques, which give two-dimensional representations of the cavity being formed and the effects of the various operating conditions on the shape evolution of the cavity. Problems with using models such as these for industrial purposes include the need for detailed descriptions of every different board pattern and the hydrodynamics of the spray. Once the board pattern has been defined, the wide range of cavity sizes across the surface and the resulting shape profiles from the rigorous solution will yield a tremendous optimization problem, depending on the overall control objective (minimizing etch undercut, maximizing etch uniformity across the board, maximizing etch rate, etc.). The scope of the present work is to use a simplified representation of the board pattern and avoid the computational burden of a rigorous finite element solution.

The only known experimental investigation of spray etching that has been published is a series of papers by Allen *et al.* (1977-1979). Their work focused on the etching of stainless and mild steel using ferric chloride in a vertical rotary spray etcher and examined the parameters affecting etch rate and etch factor, which they defined as the ratio of the etch depth over the etch undercut. They primarily examined the different profiles obtained from using masks with different line widths. They found etch rates in the vertical direction to vary depending on the spacing between lines; sidewall etching in the lateral direction did not display such a dependence. Under the same conditions, vertical etch rates for mild steel were about 20% faster than for stainless steel.

2.3 ETCH AND REGENERATION CHEMISTRY

While many compounds etch copper at rates that are economical, the problem of preventing attack or contamination of the underlying laminate limits the etchants of industrial interest largely to cupric chloride, ferric chloride, chromic-sulfuric acids, ammonium persulfate, hydrogen peroxide-sulfuric acid, and ammoniacal or alkaline etchant. The most widely used etchants are cupric chloride and the ammoniacal etchants (Datta and Romankiw, 1989). While the ammoniacal etchants have the advantage over cupric chloride of being able to etch copper selectively in the presence of tin and tin/lead resists, cupric chloride can be automatically regenerated from the reaction products, which allows steady state etching conditions and reduces waste generation. PCB manufacturers that use the ammonia-based etchants must feed and bleed their etch sumps from fresh chemical supplies to spent tanks. The spent ammoniacal etchant can be returned to the supplier or disposed.

The net reaction of copper with an aqueous cupric chloride ($CuCl_2$) solution can be written as:

$$CuCl_2 + Cu_{(s)} \rightarrow 2\,CuCl_{(s)} \tag{2.1}$$

The reaction between the cupric chloride and exposed copper results in the formation of a cuprous chloride ($CuCl$) film on the board surface. This layer is insoluble in water, thus its presence inhibits further etching. This film is soluble in excess Cl^-, which complexes with cuprous chloride to form $CuCl_3^{2-}$. Upon addition of excess chlorine to the etchant solution, cupric chloride is rapidly complexed to form the more stable $CuCl_4^{2-}$ ion and the etching reaction proceeds as follows (Sharpe and Garn, 1959, Missel and Murphy, 1969):

$$CuCl_2 + 2\,Cl^- \rightarrow CuCl_4^{2-} \tag{2.2}$$

$$CuCl_4^{2-} + Cu_{(s)} + 2\,Cl^- \rightarrow 2\,CuCl_3^{2-} \qquad (2.3)$$

Since the concentrations of cupric and chloride ions affect etch rate, the control and maintenance of the composition of the etchant stream is very important.

Methods are available for regenerating cupric chloride from the etching reaction products. This improves the efficiency of these etching systems, because the addition of fresh etchant is no longer necessary. Regeneration of cupric chloride from the cuprous complex can be achieved using chlorine, hydrogen peroxide, electrolysis, or air.

The chlorination of cuprous chloride has been the standard regeneration technique in the past because it offered low cost and high reaction rates. The reaction occurs as follows:

$$2\,CuCl_3^{2-} + Cl_2 \rightarrow 2\,CuCl_4^{2-} \qquad (2.4)$$

The primary concern with using chlorination regeneration systems is safety. Adequate ventilation, air scrubbers, leak detection sensors, and safety interlocks are necessary. Additionally, chlorine is one of the chemicals targetted for reduced usage by the Clean Air Act Amendments of 1990. Therefore, there is considerable incentive for finding a suitable replacement.

Electrolytic regeneration involves a plating tank operating at the same time as the spray etcher, with the cupric solution continuously flowing between the two. In the plating reactor, copper is plated on the cathode:

$$Cu^+ + e^- \rightarrow Cu \qquad (2.5)$$

while the regeneration of cupric from cuprous ions occurs on the anode:

$$Cu^{+} \rightarrow Cu^{2+} + e^{-} \tag{2.6}$$

Since two Cu^{+} ions are produced for every Cu^{2+} ion used in the etching reaction, the regeneration will produce one Cu^{2+} to be returned to the etch chamber, while the second cuprous ion is removed as copper in the plating reaction. Electrolytic regeneration is not widely used because it requires a large investment in special equipment and materials and involves high power consumption. It does however offer the benefit of reduced chemical waste.

Regeneration of cupric ions from cuprous ions using hydrogen peroxide is accomplished with the following reaction:

$$2\,CuCl_3^{2-} + H_2O_2 + 2\,HCl \rightarrow 2\,CuCl_4^{2-} + 2\,H_2O \tag{2.7}$$

The reaction with peroxide is highly exothermic. It must therefore be added slowly in small quantities. It is typically used only for backup regeneration purposes.

Regeneration by air in the presence of HCl occurs by the reaction (Sharpe and Garn, 1959, Bloomberg *et al.*, 1991):

$$4\,CuCl_3^{2-} + O_2 + 4\,HCl \rightarrow 4\,CuCl_4^{2-} + 2\,H_2O \tag{2.8}$$

Although air oxidation is slower than chlorination and peroxidation, it is much safer to use and is an attractive alternative to regeneration systems that use Cl_2 or H_2O_2. For this reason, this work focuses on the use of air oxidation for cupric regeneration. To simplify the notation, I will refer to the cupric and cuprous complexes simply as Cu^{2+} and Cu^{+}, respectively.

2.4 LOCAL ETCH RATE EXPRESSION

The local etching reaction is a heterogeneous process that proceeds in two steps: transport of the etching species to the board surface, followed by chemical reaction. Assuming a first order relationship with the etchant species, Cu^{2+} (A), the overall rate of reaction can be written as:

$$r_{etch} = k_{etch}A \tag{2.9}$$

A first order dependence on Cu^{2+} is assumed as a starting point to present the methodology. More complex expressions that account for product inhibition or Cl^- enhancements can be used in a manner similar to that presented here, but not analytically.

The etch rate constant, k_{etch}, is an "effective" reaction rate constant that accounts for the effects of both mass transfer and reaction kinetic limitations. For an immersion-type etching system, the time needed to achieve a certain degree of etching will largely be governed by diffusional limitations. For a spray etching system, the directional projection of the sprays toward the board surface will assist in this mass transport step, thus allowing increased etch rates due to reduced mass transfer limitations.

Shin and Economou (1989) found they could increase the etch rate by fourfold over a pure diffusion situation by adding fluid flow across the surface being etched. Similar behavior is observed when comparing the results of Covert *et al.* (1989) with industrial performance. In their investigation, Covert *et al.* conducted immersion experiments etching copper foil with cupric chloride in an agitated vessel. They obtained vertical etch rates on the order of 3.0 μm/min at 50°C. Comparing these vertical etch rates with those observed on industrial spray etching lines under similar operating conditions, the

experimental data are found to yield significantly lower etch rates. For similar temperatures and etchant compositions, actual etch rates achieved in practice are four to five times greater than those observed in the immersion experiments.

At steady state, the reaction rate is equal to the rate of mass transfer between the bulk solution and the surface:

$$r_{etch} = k_{rxn} A_i = k_L (A - A_i) \tag{2.10}$$

where k_{rxn} represents the first order kinetic rate constant, k_L is the liquid-phase mass transfer coefficient, and A_i refers to the surface concentration of Cu^{2+}. Eliminating A_i and rearranging, the overall reaction rate constant can be written as the sum of two resistances:

$$\frac{1}{k_{etch}} = \frac{1}{k_{rxn}} + \frac{1}{k_L} \tag{2.11}$$

The rate of mass transfer is increased by increasing the spray pressure, since the enhanced liquid velocity will allow better penetration of the boundary layer close to the board surface. Based on these observations, the mass transfer coefficient can be described with a power law function of the spray pressure (SP):

$$k_L = \alpha (SP)^n \tag{2.12}$$

Substitution and rearrangement gives,

$$k_{etch} = \frac{\alpha (SP)^n k_{rxn}}{\alpha (SP)^n + k_{rxn}} \tag{2.13}$$

At high values of spray pressure, where $\alpha(SP)^n \gg k_{rxn}$, the effects of spray pressure will cancel, leaving the limiting case:

$$k_{etch} = k_{rxn} \tag{2.14}$$

This case, where the spray pressure is large enough to overcome any limitations from the mass transport of the etching species to the surface, is surface reaction limited. The other extreme, where $k_{rxn} \gg \alpha(SP)^n$, results in a mass transfer limited reaction rate:

$$k_{etch} = \alpha(SP)^n \tag{2.15}$$

This approach to representing the overall heterogeneous reaction rate as a "lumped" parameter is analagous to interfacial mass transfer, where the overall mass transfer coefficient represents a series of transport steps (Cussler, 1984).

2.5 ETCH PROFILE DEVELOPMENT

The origins of the spray etching process can be traced back to photoengraving, which was invented by William Henry Fox Talbot in 1852 for the production of printing blocks for newspapers and book illustrations (Allen *et al.*, 1977). These blocks were manufactured by adhering a stensiled pattern of photoresist to the metal surface and etching away the exposed area. Because the metal being etched was only protected by the photoresist at the interface between the two materials, the problem of preventing attack on the unprotected sidewalls was an immediate concern. The prevention of etch undercut in the printing industry was accomplished through the manual application of a fusible resin known as Dragon's Blood to the sidewalls. This type of manual control is unsuitable for electronic materials fabrication, so the accepted practice is to

modify the design line widths and spacings in the mask artwork to compensate for undercut.

Figure 2.2 shows the development of a typical etch profile from the time that a board enters the first etch chamber to the time it leaves the etch line. The board enters with a layer of copper plated on both sides and masked with a polymer photoresist. In the etch chamber, vertical etching of the unmasked copper occurs on the bottom walls until the cavity bottom has been cleared, which is known as the breakthrough time (t_{BT}). As the cavity forms and the walls of the cavity become exposed to the etchant solution, lateral etching of the sidewalls also occurs. The top of the sidewalls are etched for a longer period of time than the bottom, resulting in nonvertical sidewalls. From the breakthrough time until the board leaves the etch line, any further etching that occurs is on the sidewalls only.

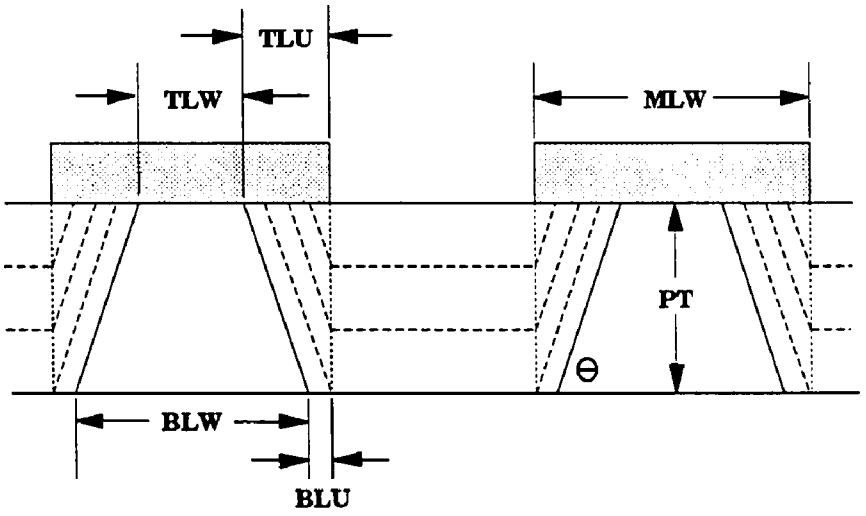

Figure 2.2: Etch Profile Development

This description of the dynamic development of the etch cavity is an ideal

representation of the actual process. In practice, the transferred line spacing at the breakthrough time will not be equal to the spacing on the mask, and the profiles of the sidewalls will be curved instead of straight, as drawn in Figure 2.2. However, it is not the intent of this work to precisely model the development of the etch profile throughout the time the boards are being etched. Instead, what we seek is a reasonable description of the process that can be used to explain the experimental observations of the boards at the end of their processing time.

The design line width on the mask (*MLW*) is specified by the artwork for the board. Similarly, the plating thickness (*PT*) is specified by the plating process that precedes the etching step. As the boards are removed from the etch line, the top (*TLW*) and bottom (*BLW*) line widths can be easily measured under a microscope. From these measurements, information about the etch angle (θ), the amount of top and bottom line undercut (*TLU* and *BLU*), and the degree of lateral relative to vertical etching can be determined.

The goal of this experimental study was to examine the effects of operating conditions on the etch profile parameters: top and bottom line width, etch undercut, and etch angle. The operating conditions considered were conveyor speed (u_{con}), top (*TSP*) and bottom (*BSP*) spray pressure, and redox potential (ORP), which is a measure of the ratio of Cu^{2+} to Cu^{+} in solution, as given by the Nernst equation (Atkins, 1982):

$$E = E' + \frac{RT}{F} ln \frac{[Cu^{2+}]}{[Cu^{+}]} \tag{2.16}$$

where E is the oxidation-reduction potential, E' is the potential at standard conditions, R is the ideal gas constant, T is the temperature in degrees Kelvin,

and F is Faraday's constant.

2.6 EXPERIMENTAL

The etch line consists of three spray etchers in series, connected to a bulk/regeneration system. The circuit boards that we used were 10x15" format panels. The selected pattern had equal line widths across the entire surface (MLW=140 μm), which allows comparison of etch profile development at different locations on the panels without having to account for differences in circuit density. The boards were plated with 1 oz. copper foil, yielding a plating thickness of 36 μm (1.4 mil), and patterned with photoresist to leave 85% of the copper area exposed. The etchant solution was a cupric chloride/hydrochloric acid solution, which is widely used industrially because it offers high etch rates combined with the ability of the etchant species (Cu^{2+}) to be regenerated from the reaction product (Cu^{+}). While the primary etchant species is the cupric ion, the presence of excess HCl is necessary to remove the cuprous product from the surface.

The effects of spray pressure, conveyor speed, and ORP were examined in this study. The experimental conditions are summarized in Table 2-2. The spray pressure and conveyor speed can both be independently set from a control panel. The experimental ORP conditions were achieved by allowing the ORP to rise above the desired value, then feeding "dummy" copper panels through the system to bring the ORP down to the desired value. ORP was measured using a Foxboro 872 Electrochemical Monitor. We weighed the boards before and after they were processed in the etch chambers to determine the amount of copper etched. After weighing, the photoresist was stripped off and the boards were rinsed and dried. Two boards were processed consecutively under each set of

experimental conditions and the average value of the measured parameters was used as the experimental response.

Table 2-2: Summary of Experimental Conditions

Experimental Design				Values			
Boards	*ORP*	*SP*	u_{con}	*ORP* (mV)	*TSP* (psi)	*BSP* (psi)	u_{con} (m/min)
1-2	+1	+1	+1	521.5	30	20	2.00
3-4	+1	+1	0	522.3	30	20	1.75
5-6	+1	+1	−1	523.3	30	20	1.50
7-8	+1	−1	+1	519.4	20	10	2.00
9-10		** discarded **					
11-12	+1	−1	0	526.5	20	10	1.75
13-14	+1	−1	−1	522.6	20	10	1.50
15-16	−1	+1	+1	509.8	30	20	2.00
17-18	−1	+1	0	510.7	30	20	1.75
19-20	−1	+1	−1	513.6	30	20	1.50
21-22	−1	−1	+1	509.2	20	10	2.00
23-24	−1	−1	0	510.3	20	10	1.75
25-26	−1	−1	−1	507.1	20	10	1.50

Following the etching of the boards, we measured the line widths using a Micro-Plan II Image Analysis System (Don Santo Corporation). Groups of four consecutive lines were identified at four separate locations (A-D) across the surface of each side of the board. Location A is close to the leading edge of the board, B and C are both near the center, and D is close to the trailing edge. Top and bottom line widths were measured at two locations on each of the four lines at each of these four locations.

2.7 RESULTS AND DISCUSSION

For each combination of experimental conditions (ORP and spray pressure), boards were etched at three different residence times, which allows us to observe the development of the etch profile with time. In Figures 2.3 and 2.4, schematic representations of the line cross-sections are shown, based on the top and bottom line width measurements. The etch angle can be determined from the line width measurements by the relationship:

$$\theta = tan^{-1} \frac{2(PT)}{BLW-TLW} \tag{2.17}$$

These data are summarized in Table 2-3.

Comparing Figure 2.3*b* with 2.4*a*, there is a distinct difference in etch profile under the same operating conditions between the top and bottom sides of the panels. Considerably more etching occurs on the bottom side. This is in spite of the two cases being identical in all other respects. This can be explained by examining the differences in the hydrodynamics of the etchant solution contacting the two board surfaces.

Puddles were observed forming on the center of the top side of the boards. These inhibit the transport of fresh etchant solution to the surface of the panel. The etchant species are therefore subject to additional mass transport limitations on the top side of the boards resulting from having to diffuse through the liquid layer, thus decreasing the amount of etching activity relative to the bottom side. As a consequence, higher spray pressures are required for the top nozzles than for the bottom nozzles in order to compensate for the increased mass transfer limitations. This is shown in Figure 2.4*b*, which shows the top side profile at a higher spray pressure (30 psi). This profile is seen to approach the bottom side profile at 20 psi (Figure 2.3*b*).

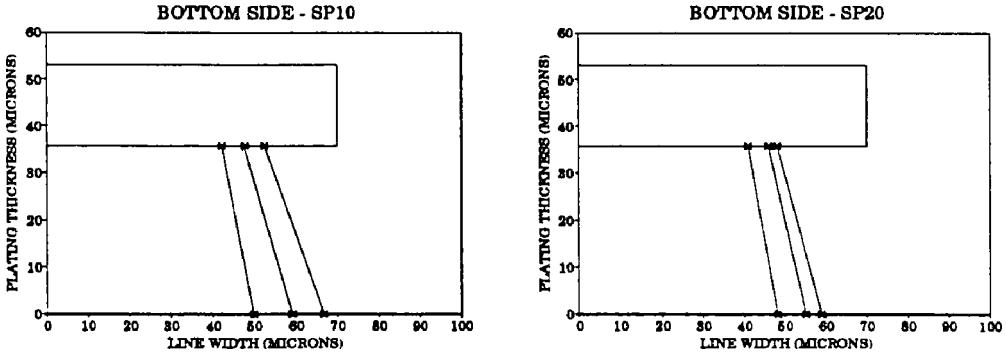

(a) *(b)*

Figure 2.3: Top and Bottom Line Undercut, Bottom Side
(a) Spray Pressure = 10 psi
(b) Spray Pressure = 20 psi

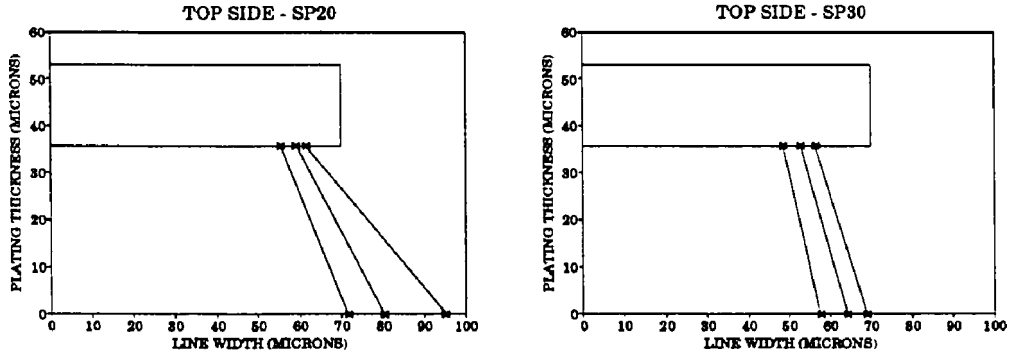

(a) *(b)*

Figure 2.4: Top and Bottom Line Undercut, Top Side
(a) Spray Pressure = 20 psi
(b) Spray Pressure = 30 psi

A change in etch angle with etch line residence time is most clearly noticeable in Figure 2.4*a*. Figures 2.5*a* and *b* show the change in line width difference (*BLW–TLW*) that results from different residence times in the etch line. The line widths and the line width differences are significantly smaller

Table 2-3. Summary of Average Etch Profile Data

Boards	Bottom Side			Top Side		
	TLW (μm)	*BLW* (μm)	θ (deg)	*TLW* (μm)	*BLW* (μm)	θ (deg)
			BSP=20, *TSP*=30 psi			
1-2	96	118	73	114	138	71
3-4	92	110	75	106	129	72
5-6	82	97	78	97	116	76
15-16	94	117	72	108	138	67
17-18	90	108	76	105	128	72
19-20	80	94	79	96	112	77
			BSP=10, *TSP*=20 psi			
7-8	105	133	69	123	190	47
11-12	96	118	73	118	161	59
13-14	85	100	78	111	143	66
21-22	105	136	67	123	196	44
23-24	97	122	71	118	171	54
25-26	89	108	75	114	150	63

when the residence time is longer. This implies that more vertical sidewalls can be achieved by overetching the desired features. Therefore, the practice that has been adopted in industry is to overdesign the line widths for the mask such that the desired line width on the board can be produced with more vertical walls.

The dynamic behavior of the etch angle is due to the formation of weak recirculating eddies in the undercut regions immediately beneath the etch mask (Alkire and Deligianni, 1988). These eddies inhibit diffusion in the lateral

(a) Residence time = 2.13 min

(b) Residence time = 2.84 min

Figure 2.5: Effect of Residence Time on Line Width Difference

direction of etchant species to the sidewalls near the top of the line being etched, thus allowing increased lateral etching close to the bottom of the line. This results in more vertical walls as the degree of etch undercut increases. As Figures 2.3*a* and *b* indicate, the effects of these recirculating eddies are much less apparent on the bottom side, where the etch angle does not change appreciably with time, even at low spray pressures. Figure 2.4*b* shows that high spray pressures result in a primary circulatory eddy within the etch cavity that is dominant enough to prevent the formation of the weak secondary eddies, thus reducing the change in etch angle with time.

It is expected that this mass transfer effect will vary depending on the spray pressure. For the bottom side, the relationship between the top (*TLU*) and bottom line undercut (*BLU*) is linear and independent of spray pressure, as shown in Figure 2.6*a*. On the top side of the boards, there is a slight dependency of the slope of the line with spray pressure, as Figure 2.6*b* shows, but it is not a significant effect over the range of spray pressures investigated. The slopes of these lines represent the ratio of the lateral etch rate at the top (r_{LET}) to the rate at the bottom of the line (r_{LEB}).

$$\frac{dTLU}{dBLU} = \frac{r_{LET}}{r_{LEB}} = \begin{cases} 0.61 & \text{(Top Side)} \\ 0.32 & \text{(Bottom Side)} \end{cases} \tag{2.18}$$

On the bottom side of the panels, the average lateral etch rate at the top of the line and the average vertical etch rate are related by the breakthrough time, t_{BT}. The breakthrough time is defined as the time when the plating thickness has been cleared. On the bottom side, the top line undercut at the breakthrough point, TLU_{BT}, was determined from the y-intercept of Figure 2.6*a* to be 15.6 μm, regardless of spray pressure. From Figure 2.6*b*, TLU_{BT} on the top

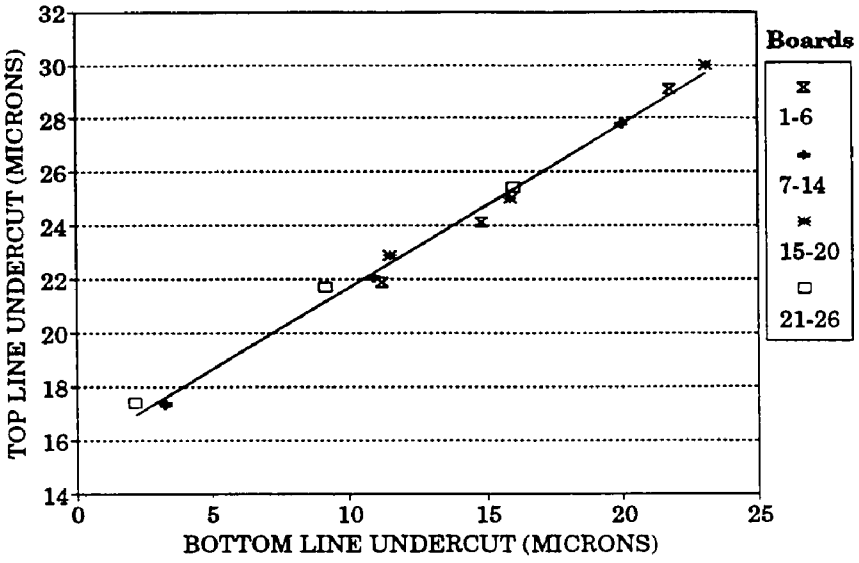

(a) Bottom Side

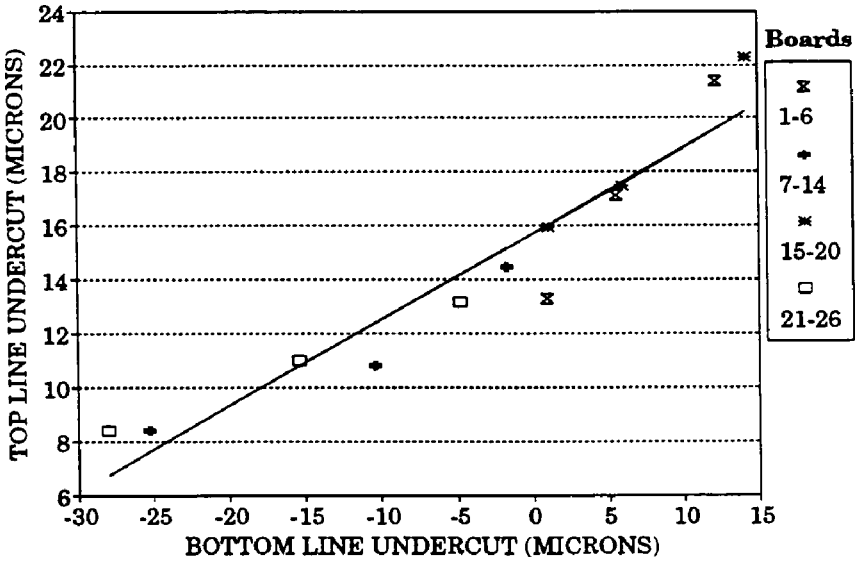

(b) Top Side

Figure 2.6: Relationship between Top and Bottom Line Undercut

side is 15.7 μm. The average lateral etch rate at the top of the line is:

$$r_{LET} = \frac{TLU_{BT}}{t_{BT}} \tag{2.19}$$

The breakthrough time also defines the average vertical etch rate:

$$r_{VE} = \frac{PT}{t_{BT}} \tag{2.20}$$

Combining these two equations,

$$\frac{r_{LET}}{r_{VE}} = \frac{TLU_{BT}}{PT} = 0.44 \quad \text{(Both Top and Bottom Sides)} \tag{2.21}$$

From the data summarized in Table 2-3, the average lateral etch rates at the top of the lines, r_{LET}, and the "effective" lateral etch rate constant, k_{LET}, can be easily calculated for both sides of the boards. Because of the spray pressure functionality of the mass transfer limitations, as defined in Equation (2.12), the etch rate, and hence the etch rate constant, will depend on spray pressure. From the etch rate vs. spray pressure data, the best-fit values for the parameters α, n, and k_{rxn} can be determined.

Using Equation (2.13) at two different spray pressures to eliminate k_{rxn},

$$\alpha_{LET} = \left(\frac{k_{LET1}k_{LET2}}{k_{LET2} - k_{LET1}}\right)\left(\frac{(SP_2)^n - (SP_1)^n}{(SP_1)^n(SP_2)^n}\right) \tag{2.22}$$

Combining Equations (2.22) and (2.13),

$$k_{rxn} = \frac{\alpha_{LET}(SP)^n k_{LET}}{\alpha_{LET}(SP)^n - k_{LET}} \tag{2.23}$$

which can be used to relate the other etch rates to the lateral etch rate at the top of the line using Equations (2.18) and (2.21).

$$\alpha_{VE} = \frac{k_{LET}k_{rxn}}{(0.44k_{rxn} - k_{LET})(SP)^n} \tag{2.24}$$

$$\alpha_{LEB} = \frac{k_{LET}k_{rxn}}{(\beta k_{rxn} - k_{LET})(SP)^n} \tag{2.25}$$

where β is equal to 0.61 for the top side and 0.32 for the bottom side of the boards. The final parameters that were found to fit the data best are summarized in Table 2-4. Notice that the dependency on spray pressure is greater for the top side (n=1.39) than for the bottom side (n=0.29). To reemphasize a point made earlier, this is due to the increased mass transfer limitations caused by the collection of puddles on the top side, which are not present on the bottom side. Therefore the top spray pressure has the additional effect of aiding the penetration of the liquid layer on the board surface while assisting the transport of the etching species to the exposed copper.

Table 2-4. Summary of Local Etch Rate Parameters

Parameter	Bottom Side	Top Side
n	0.29	1.39
α_{LEB}	4.04*E*–04	2.47*E*–05
α_{LET}	2.00*E*–04	2.70*E*–06
α_{VE}	7.27*E*–04	8.08*E*–06
k_{rxn} = 16.2*E*–04 (cm/min/(mol/l))		

2.8 REFERENCES

Alkire, R. C., D. B. Reiser, and R. L. Sani, "Effect of Fluid Flow on Removal of Dissolution Products from Small Cavities", *J. Electrochem. Soc.*, **131**(12), 2795 (1984).

Alkire, R. C. and H. Deligianni, "The Role of Mass Transport on Anisotropic Electrochemical Pattern Etching", *J. Electrochem. Soc.*, **135**(5), 1093 (1988).

Allen, D. M., D. F. Horne, and G. W. W. Stevens, "Quantitative Examination of Photofabricated Profiles, Part 1: Design of Experiments", *J. Photog. Sci.*, **25**, 254 (1977).

Allen, D. M., D. F. Horne, and G. W. W. Stevens, "Quantitative Examination of Photofabricated Profiles, Part 2: Photoetched Profiles in Stainless Steel", *J. Photog. Sci.*, **26**, 72 (1978).

Allen, D. M., D. F. Horne, and G. W. W. Stevens, "Quantitative Examination of Photofabricated Profiles, Part 3: Measurement of Etch Factor", *J. Photog. Sci.*, **26**, 242 (1978).

Allen, D. M., D. F. Horne, and G. W. W. Stevens, "Quantitative Examination of Photofabricated Profiles, Part 4: Photoetched Profiles in Mild Steel", *J. Photog. Sci.*, **27**, 181 (1979).

Atkins, P. W., *Physical Chemistry*, 2nd ed., W. H. Freeman and Company, San Francisco (1982).

Blumberg, L. R., D. D. Coolbaugh, J. A. Kurowski, and E. A. Stromecki, "Continuous Regeneration of Acid Solution", Patent No. 5,013,395 (1991).

Covert, K. L., D. N. Light, and R. W. Keesler, "Etch Rate of Copper in Acidic Cupric Chloride: A Designed Experiment", IBM Technical Report TR 01.B275 (1989).

Cussler, E. L., *Diffusion: Mass Transfer in Fluid Systems*, Cambridge University Press, New York (1984).

Datta, M. and L. T. Romankiw, "Application of Chemical and Electrochemical Micromachining in the Electronics Industry", *J. Electrochem. Soc.*, **136**(6), 285 (1989).

Duffek, E. F. and E. Armstrong, "Etching", In *Printed Circuits Handbook*, 2nd ed., C.F. Coombs (Ed.), McGraw-Hill(1979).

Kuiken, H. K., J. J. Kelly, and P. H. L. Notten, "Etching Profiles at Resist Edges: I. Mathematical Models for Diffusion-Controlled Cases", *J. Electrochem. Soc.*, **133**(6), 1217 (1986).

Missel, L. and P. D. Murphy, "Steady State Etching of Copper: Cupric Chloride-Sodium Chloride Baths", *Metal Finishing*, **58**, 47 (1969).

Schnorr, D. P., "Design and Application of Rigid and Flexible Printed Wiring", In *Handbook of Electronic Packaging*, C.A. Harper (Ed.), McGraw-Hill(1969).

Sharpe, L. H. and P. D. Garn, "Regenerable Etchant for Copper", *Ind. Eng. Chem.*, **51**, 293 (1959).

Shin, C. B. and D. J. Economou, "Effect of Transport and Reaction on the Shape Evolution of Cavities during Wet Chemical Etching", *J. Electrochem. Soc.*, **136**(7), 1997 (1989).

This is a blank page

CHAPTER

THREE

DYNAMIC GLOBAL MODELING

3.1 MODEL DEVELOPMENT

For larger scale processing, several spray etchers can be run in series. Rather than regenerate the etchant species at each individual sump tank, a bulk regeneration system may be employed. In this process, the overflow streams from several sump tanks are routed to a central bulk tank. This bulk tank is where the regeneration of the etchant Cu^{2+} from Cu^{+} occurs. The regenerated etchant is then fed back from the bulk tank to the sump tanks on the etch lines. A schematic diagram of the case system used is shown in Figure 3.1.

Dynamic mass balances can be written around each of the etchers (E_i), each sump tank (S_i), the bulk tank (B), and the regenerator (R) for Cu^{2+} (A) and Cu^{+} (B), where i=1, $\cdots$, N and N is the number of etcher/sump tanks in the system. The copper ions actually exist in solution as cupric and cuprous complexes, complexing with free Cl^{-} ions. However, since Cl^{-} is not consumed in either the etching or the regeneration reaction, its concentration is assumed to be constant.

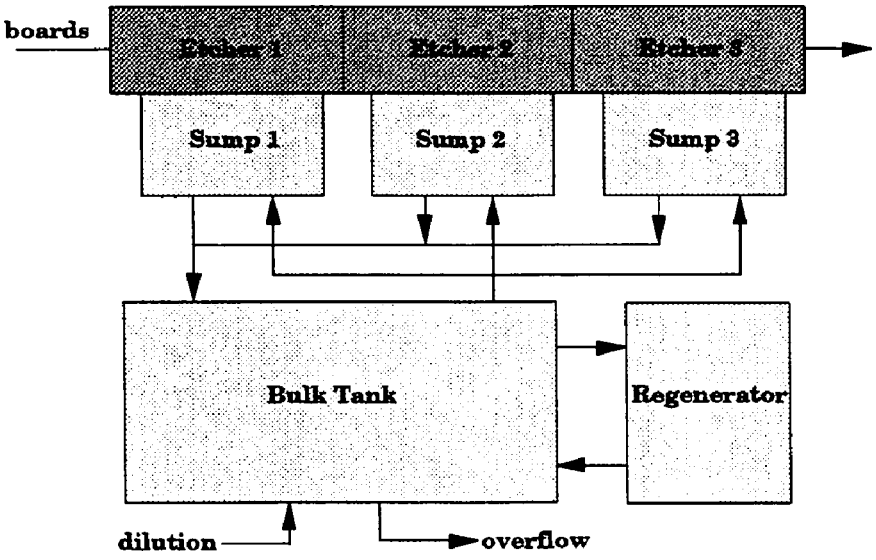

Figure 3.1: Overall Spray Etching System

Assuming all tanks are well-mixed, the mass balance for either component at any location j (etcher, sump tank, bulk tank, or regenerator) can be written as follows:

Etchers:

$$\gamma_{Ei} V_{Ei} \frac{dA_{Ei}}{dt} = F_{EiSi} (A_{Si} - A_{Ei}) - N_A \tag{3.1}$$

$$\gamma_{Ei} V_{Ei} \frac{dB_{Ei}}{dt} = F_{EiSi} (B_{Si} - B_{Ei}) + 2 N_A \tag{3.2}$$

Sump Tanks:

$$V_{Si} \frac{dA_{Si}}{dt} = F_{EiSi} (A_{Ei} - A_{Si}) + F_{BSi} (A_B - A_{Si}) \tag{3.3}$$

$$V_{Si} \frac{dB_{Si}}{dt} = F_{EiSi} (B_{Ei} - B_{Si}) + F_{BSi} (B_B - B_{Si}) \tag{3.4}$$

Bulk Tank:

$$V_B \frac{dA_B}{dt} = \sum_{i=1}^{N} F_{BSi}(A_{Si}-A_B) + F_{BR}(A_R-A_B) + F_D(A_D-A_B) \tag{3.5}$$

$$V_B \frac{dB_B}{dt} = \sum_{i=1}^{N} F_{BSi}(B_{Si}-B_B) + F_{BR}(B_R-B_B) + F_D(B_D-B_B) \tag{3.6}$$

Regenerator:

$$V_R \frac{dA_R}{dt} = F_{BR}(A_B-A_R) + r_{regen}V_R \tag{3.7}$$

$$V_R \frac{dB_R}{dt} = F_{BR}(B_B-B_R) - r_{regen}V_R \tag{3.8}$$

where V_j is the volume of unit j, A_j is the concentration of A in unit j, F_{jk} is the volumetric flow rate between location j and k, and r_{regen} is the molar regeneration rate. N_A is the rate of cupric ions going into the etching reaction, which is determined by the amount of vertical and lateral etching occurring across the length of each etch chamber. This molar reaction rate is a function of the amount of exposed area, which is determined by the artwork on the panel. F_D and A_D refer to the flow rate and species composition of the dilution stream from the external *HCl* tank, which is used to maintain constant specific gravity in the bulk tank. The term γ_{E_i} is a function of operating parameters (spray nozzle type and position, nozzle pressure, spray direction, etc.) representing the ratio of the volume of liquid on the board surface to the tank volume of the etch chamber.

The volume of the liquid in the etch chamber at any time is much less than the tank volumes anywhere else in the system. The model can therefore be simplified by assuming the etchers to be at pseudo-steady-state, which implies the concentrations in the etcher change instantaneously. By setting the time

derivatives in Equations (3.1) and (3.2) equal to zero, the sump tank balances become:

$$V_{Si}\frac{dA_{Si}}{dt} = -N_A + F_{BSi}(A_B - A_{Si}) \tag{3.9}$$

$$V_{Si}\frac{dB_{Si}}{dt} = 2N_A + F_{BSi}(B_B - B_{Si}) \tag{3.10}$$

This pseudo-steady-state assumption eliminates the unknown parameter γ_{E_i}.

The model can be expressed in terms of dimensionless variables by normalizing the concentrations with respect to a reference Cu^{2+} concentration, and normalizing the flow rates and tank volumes with respect to the appropriate bulk tank characteristics:

Sump Tanks:

$$V^*_{Si}\frac{dA^*_{Si}}{d\tau} = -Da_{Ei}N^*_A + F^*_{BSi}(A^*_B - A^*_{Si}) \tag{3.11}$$

$$V^*_{Si}\frac{dB^*_{Si}}{d\tau} = 2Da_{Ei}N^*_A + F^*_{BSi}(B^*_B - B^*_{Si}) \tag{3.12}$$

Bulk Tank:

$$\frac{dA^*_B}{d\tau} = \sum_{i=1}^{N} F^*_{BSi}(A^*_{Si} - A^*_B) + F^*_{BR}(A^*_R - A^*_B) + F^*_D(A^*_D - A^*_B) \tag{3.13}$$

$$\frac{dB^*_B}{d\tau} = \sum_{i=1}^{N} F^*_{BSi}(B^*_{Si} - B^*_B) + F^*_{BR}(B^*_R - B^*_B) + F^*_D(B^*_D - B^*_B) \tag{3.14}$$

Regenerator:

$$V_R^* \frac{dA_R^*}{d\tau} = F_{BR}^* (A_B^* - A_R^*) + Da_R R_{regen} V_R^* \tag{3.15}$$

$$V_R^* \frac{dB_R^*}{d\tau} = F_{BR}^* (B_B^* - B_R^*) - Da_R R_{regen} V_R^* \tag{3.16}$$

where A_j^* and B_j^* refer to cupric and cuprous ion concentrations in unit j normalized by a reference cupric concentration, A_{ref}, V_j^* is the volume of unit j normalized by the bulk tank volume, and F_{ij}^* is the volumetric flow rate between units i and j normalized by the total flow rate leaving the bulk tank, F_B, which is defined as,

$$F_B \equiv \sum_{i=1}^{N} F_{BSi} + F_{BR} + F_D \tag{3.17}$$

The dimensionless time, τ, is normalized by the residence time of solution in the bulk tank, $t_B \equiv V_B/F_B$. N_A^* is the rate of cupric ion depletion expressed in terms of dimensionless etch rates, and R_{regen} is the dimensionless regeneration rate. Da_E and Da_R are the Damkoehler numbers associated with the etching reaction and the regeneration reaction; the Damkoehler number represents the ratio of the residence time of the solution in the bulk tank over a reference reaction time. These dimensionless variables will be defined as we develop the local reaction mechanisms for the etching and regeneration steps.

3.2 REGENERATOR MODEL

The concentration of A entering the bulk tank from the regenerator, A_R, is determined from a pseudo-steady state mass balance around the regenerator. The regenerator is assumed to be a mixed tower filled with packing, with a liquid stream pumped from the bulk tank up through the bottom of the tower, the exit stream from the top being directed back into the bulk tank. Chlorine gas or oxygen flows cocurrently with the liquid stream upward through the tower. This system is similar to the air regeneration system described by Blumberg *et al.* (1991). Regeneration occurs when the reactant (R) from the gas is absorbed into the liquid stream, where it reacts irreversibly with Cu^+ to form the etchant species Cu^{2+}:

$$R_{(G)} \rightarrow R_{(L)} \tag{3.18}$$

$$R_{(L)} + Cu^+ \rightarrow Cu^{2+} + \text{byproducts} \tag{3.19}$$

Equation (3.19) is a generalization of either Equation (2.4) or (2.8). When using either chlorine or oxygen as the reactant R, the absorption reaction is typically the rate limiting step.

Studies have been published that analyze the rates of absorption into water for chlorine (Brian *et al.*, 1962) and oxygen (Jhaveri and Sharma, 1967). Both use penetration theory solutions (Danckwerts, 1955) to account for the effects of simultaneous chemical reaction on gas absorption. Data from Jhaveri and Sharma (1967) show that the rate of absorption of oxygen in aqueous solutions of cupric chloride can be written:

$$r_{abs} = (k_{regen} D_L)^{1/2} [Cu^+][O_2]_0 a_e \tag{3.20}$$

where k_{regen} is the reaction rate constant, D_L is the liquid-phase diffusion

coefficient of O_2 in water, $[O_2]_0$ represents the liquid phase oxygen concentration at the gas-liquid interface, and a_e is the effective mass transfer area. The oxygen concentration at the interface is related to the bulk gas phase composition by Henry's Law:

$$[O_2]_0 = C_0 \frac{y_{O_2} P}{H} \tag{3.21}$$

where C_0 is the liquid molar volume, y_{O_2} is mole fraction of oxygen in the gas, P is the pressure, and H is the Henry's Law constant.

Assuming the residence time of the liquid in the regenerator is small compared to the bulk tank, steady state mass balances for liquid-phase cupric/cuprous ions and gas-phase oxygen around the regeneration tower can be used:

$$\frac{F_{RS}}{S_R}\frac{d[Cu^{2+}]}{dz} = -\frac{F_{RS}}{S_R}\frac{d[Cu^{+}]}{dz} = 4r_{abs} \tag{3.22}$$

$$\frac{d}{dz}(Gy_{O_2}) = -r_{abs} \tag{3.23}$$

where z is the distance through the regenerator, S_R is the cross-sectional area of the tower, G is the gas molar flux, and y_{O_2} is the mole fraction of oxygen in the gas stream. A mass balance on the nitrogen in the air stream gives a relationship between the oxygen mole fraction and the gas molar flow rate:

$$\frac{G}{G_0} = \frac{1 - y_{O_2,0}}{1 - y_{O_2}} \tag{3.24}$$

where G_0 and $y_{O_2,0}$ are the entering gas molar flux and oxygen mole fraction,

respectively. Using this relationship, Equation (3.23) can be rewritten:

$$G_0 \frac{1 - y_{O_2,0}}{(1 - y_{O_2})^2} \frac{dy_{O_2}}{dz} = -r_{abs} \tag{3.25}$$

Substituting Equation (3.25) into the Cu^+ balance in Equation (3.22) and integrating y_{O_2} with respect to $[Cu^+]$ gives:

$$y_{O_2} = \frac{4G_0 S_R y_{O_2,0} + F_{RS}([Cu^+] - [Cu^+]_0)}{4G_0 S_R + F_{RS}([Cu^+] - [Cu^+]_0)} \tag{3.26}$$

Combining Equations (3.26) and (3.21) with (3.20) and substituting into the Cu^+ balance of Equation (3.22), we can now integrate $[Cu^+]$ with respect to z. Assuming a small change in liquid Cu^+ concentration and a linear pressure profile across the tower,

$$\frac{[Cu^+]_R}{[Cu^+]_B} = 1 - k_R \frac{V_R}{F_{RS}} \tag{3.27}$$

with,

$$k_R = 2(k_{regen} D_L)^{1/2} a_e \frac{C_0}{H} y_{O_2,0} \varepsilon (P_0 + P_{atm}) \tag{3.28}$$

where P_0 is the entering pressure. Combining this relationship with the steady state case of Equation (3.8), we get:

$$r_{regen} = k_R B_B \tag{3.29}$$

or, by normalizing with respect to A_{ref}, we can define the dimensionless

regeneration rate and its associated Damkoehler number:

$$R_{regen} = \frac{k_R B_B}{k_R A_{ref}} = B_B^* \tag{3.30}$$

$$Da_R = \frac{V_B k_R}{F_B} \tag{3.31}$$

with k_R defined by Equation (3.28).

3.3 OPEN LOOP MODEL

The etch angle is determined from the plating thickness, and the top and bottom line widths:

$$\theta = tan^{-1} \frac{2(PT)}{BLW - TLW} \tag{3.32}$$

The breakthrough time can be determined by integrating the vertical etch rate expression with time until the etch depth is equal to the plating thickness:

$$\int_0^{t_{BT}} r_{VE}(t)\, dt = PT \tag{3.33}$$

In order to quantify the term N_A in Equations (3.9) and (3.10), we need expression for the relating the local etch rates and the board characteristics. To determine this rate of cupric ion depletion, the contributions due to vertical and lateral etching were calculated separately. Each etch chamber was divided into M discrete regions and the etch profile was computed for each of these locations. The fraction of the board surface area that is masked, ε_M, is known from the artwork for the board. The rate of copper removal by vertical etching from each

side of a board can be determined for the ith discrete region,

$$N_{VEi} = (r_{VE})(BW)(1-\varepsilon_M)(\Delta z)\frac{\rho}{MW} \tag{3.34}$$

where BW is the board width and Δz is the length of each of the M discrete regions in the etch chamber. In the vertical direction, etching will occur until the plating thickness has been reached at the breakthrough point. Beyond this point, no further vertical etching occurs.

In order to determine the amount of lateral etching that occurs, however, we need to know the wall surface area. The mask line widths across the panel are generally known, so an average line width can be determined. However, the perimeter of the masked region is not always available. In the absence of this information, we will approximate the artwork as a series of parallel lines extending across the length of the circuit board. Each of these lines will have a nominal line width equal to the average mask line width, MLW. Knowing the total mask area and the area of each line across the panel, the line spacing is easily calculated. The number of lines across the length of each board is:

$$n_L = \frac{\varepsilon_M(BW)}{MLW} \tag{3.35}$$

Multiplying the area of the exposed sidewall by the lateral etch rate gives the rate that copper is being removed from one side of a line on the board in that discrete region. For the two sides of each line, the contribution of the lateral etching to the rate of Cu^{2+} depletion is,

$$N_{LEi} = (r_{LE})(2n_L)\frac{d_{i-1}+d_i}{2}(\Delta z)\frac{\rho}{MW} \tag{3.36}$$

where d_{i-1} and d_i represent the etch depths at the beginning and the end of the ith discrete region in the etch chamber, determined from the vertical etch rates. Beyond the breakthrough point, both of these depths are equal to the plating thickness.

The summation of the vertical and lateral contributions at each discrete location along each etch chamber, defined by Equations (3.34) and (3.36), gives the rate of cupric ion depletion for each side of the board. Therefore the total reaction rate is,

$$N_A = 2\sum_{i=1}^{M}(N_{VEi}+N_{LEi}) \tag{3.37}$$

The dimensionless rate of Cu^{2+} depletion is defined by normalizing the concentration of Cu^{2+} in the etch rate expression with A_{ref} and defining the Damkoehler number,

$$Da_E = \frac{V_B k_{etch} a}{F_B}\frac{\rho}{MW} \tag{3.38}$$

where a represents the area being etched and k_{etch} is defined by Equation (2.13)

Because of the differences between the vertical and lateral etch rates on either side of the boards, different Damkoehler numbers are defined for each type of etching. For vertical etching, the appropriate Damkoehler number based on the area subject to vertical etching for sump tank i is:

$$Da_{VEi} = \frac{V_B}{F_B}(k_{VE,TS}+k_{VE,BS})(L_{Ei})(BW)(1-\varepsilon_M)\frac{\rho}{MW} \tag{3.39}$$

where the etch rate constants depend on the spray pressures and the side of the

board. The subscripts *TS* and *BS* are used to distinguish between when the etch rate parameters for the top side or the bottom side are used, respectively, for calculating the effective etch rate constant. For lateral etching, the appropriate Damkoehler number for sump tank *i* is:

$$Da_{LEi} = \frac{V_B}{F_B}(k_{LE,TS}+k_{LE,BS})(2n_L)(L_{Ei})(PT)\frac{\rho}{MW} \tag{3.40}$$

The dimensionless parameters used are given in Table 4.

Table 4: Summary of Dimensionless Model Parameters

Parameter	Value	Parameter	Value
V^*_{Si}	0.08	F^*_{BSi}	0.137
V^*_R	0.60	F^*_{BR}	0.584
		F^*_D	0.005
Da_R	0.28		
Da_{VEi}	10.8		
Da_{LEi}	1.31		

The global model was run to simulate the experimental conditions of the previous section. Figures 3.2*a* and 3.3*a* compare the top and bottom line widths on the bottom side for conveyor speeds of 1.75 (t=0–10 min), 1.5 (t=10–20 min), and 2.0 m/min (t=20–30 min), respectively, with a bottom spray pressure of 20 psi. The results for the lower spray pressure (*BSP*=10 psi) are given in Figures 3.4*a* and *b*. In each of these figures, the corresponding experimental data (at different regions on the board surface) were also plotted. The discrepency between the model and the data, most noticable at the lowest conveyor speed

(longest residence times), results from scatter in the experimental etch rates. The model uses an average lateral etch rate, dependent on spray pressure and etchant concentration but independent of conveyor speed, while the experimentally observed etch rates varied by ±1 μm/min.

The steady state etch profiles across the etch line for each conveyor speed are shown in Figures 3.2*b* and 3.3*b*. The top line width starts with a nominal value equal to the mask line width at the entrance to the first etch chamber. The value of *TLW* steadily decreases as the boards proceed through the reactors. The bottom line width will remain equal to *MLW* until the plating thickness has been etched through. At this point, lateral etching at the bottom begins and continues until the board leaves the last etcher. Thus, there is a steady decrease in *BLW* from the breakthrough point until the end of the residence time. Again, the actual bottom line width at the breakthrough point will probably be greater than the mask line width, whereas we have depicted the line widths to be equal. This comes from the representation of the dynamic etch profile development that we selected, as given in Figure 2.2.

Any change in board speed will change the slope of the *TLW* profile across the reactor length (Figure 3.2*a*), which shifts the nominal value of the exit *TLW* accordingly (Figure 3.2*b*). The decrease in board speed increased the slope of the *TLW* profile, while the *BLW* profile shifted to the left (due to the resulting change in breakthrough time) as well as changing slope slightly.

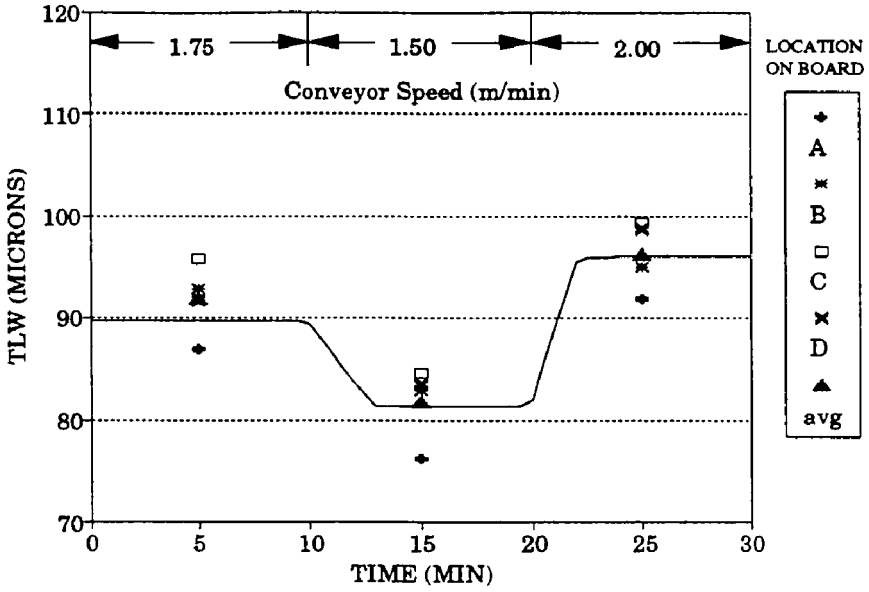

(a) Exit Top Line Width

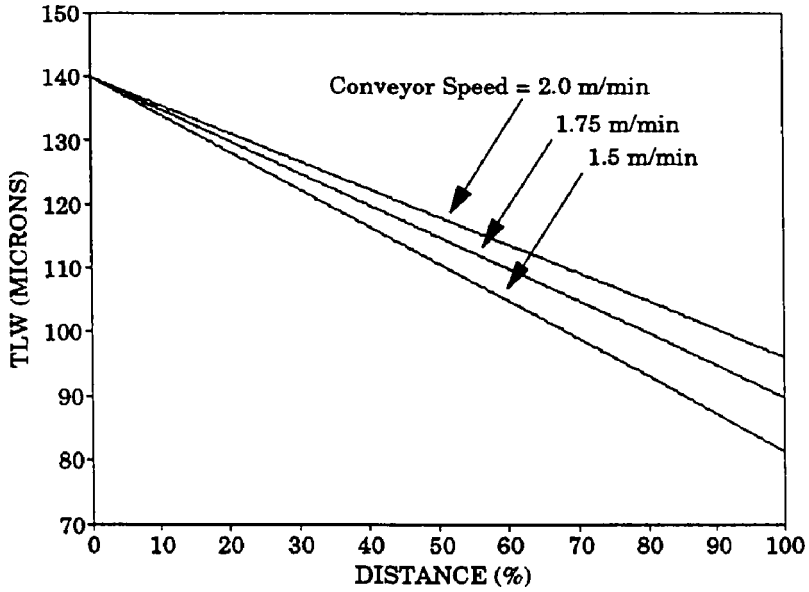

(b) TLW Profile Across Etch Line

Figure 3.2: Top Line Width Profiles, Bottom Side, *BSP*=20 psi

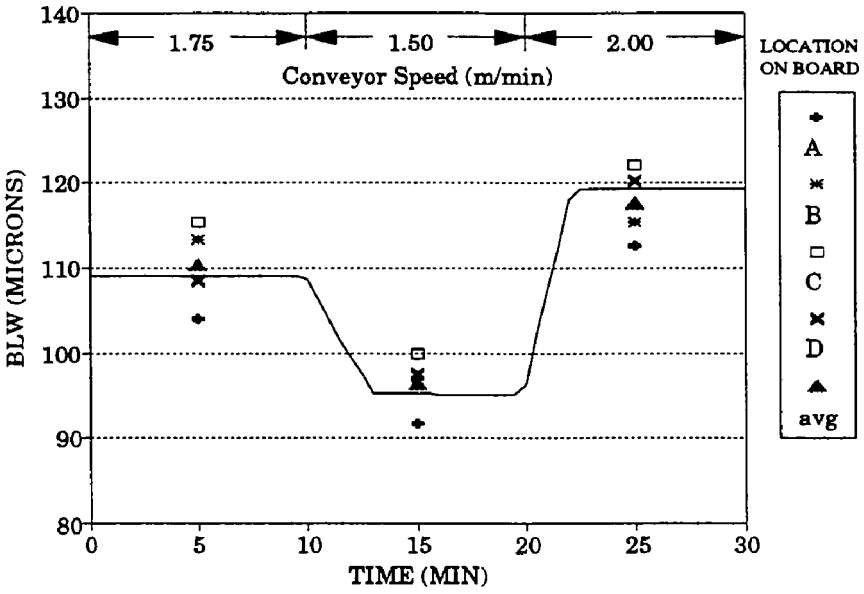

(*a*) Exit Bottom Line Width

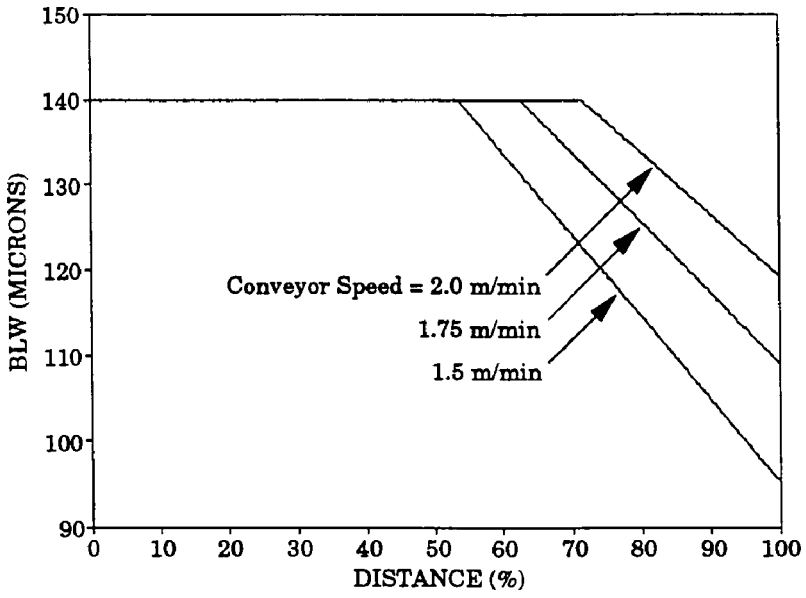

(*b*) *BLW* Profile Across Etch Line

Figure 3.3: Bottom Line Width Profiles, Bottom Side, *BSP*=20 psi

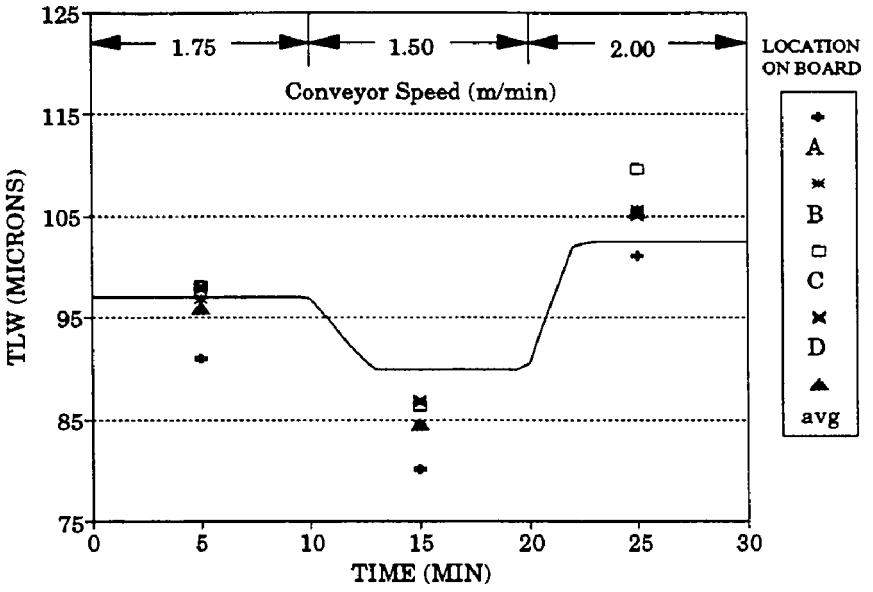

(*a*) Exit Top Line Width

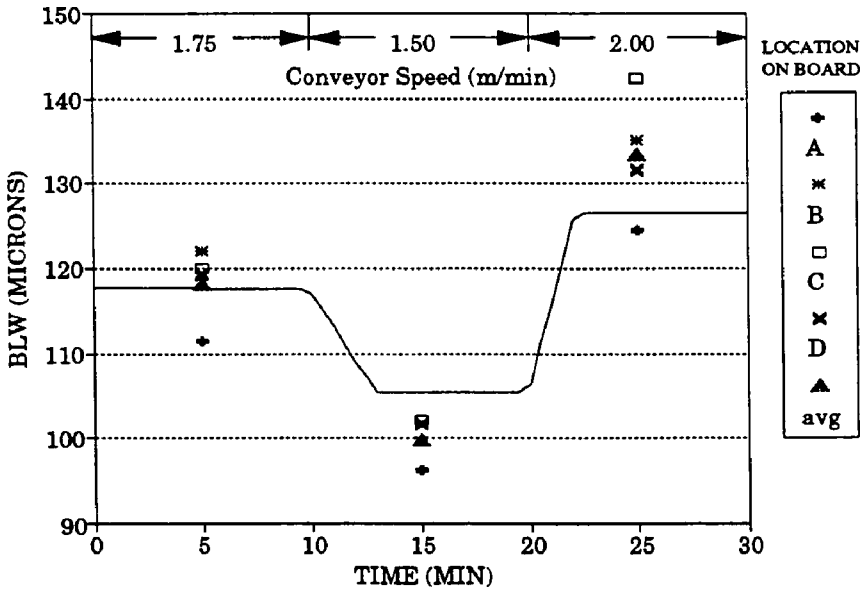

(*b*) Exit Bottom Line Width

Figure 3.4: Line Width Profiles, Bottom Side, *BSP*=10 psi

3.4 DYNAMIC ANALYSIS

In order to ensure controllable etching behavior, we must first examine the dynamic characteristics of the etching species concentrations, so a method for maintaining a consistent sump tank composition can be developed. This will then allow us to design the control system for achieving a desired etch quality with the knowledge of what the etchant concentrations available will be.

Using the model developed in the previous section, the responses of the cupric and cuprous ion concentration profiles from steady state operation to a step change in board area are shown in Figures 3.5*a* and *b*. Several observations are worthy of note. Of particular interest are the significant difference (several orders of magnitude) in the time $[Cu^{+}]$ reaches its new steady state compared to $[Cu^{2+}]$ and the inverse response in the $[Cu^{2+}]$ profile.

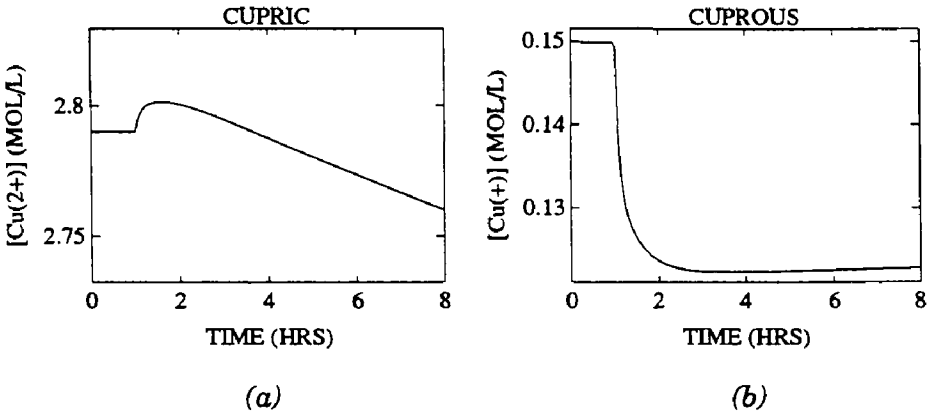

Figure 3.5: Response of $[Cu^{2+}]$ (*a*) and $[Cu^{+}]$ (*b*) to step change in board area

To explain the first observation, consider the simple case of a mixed tank with a first order $A \rightarrow B$ reaction occuring. For this example, the mass balances are:

$$V\frac{dA}{dt} = F(A_f - A) - kAV \tag{3.41}$$

$$V\frac{dB}{dt} = F(B_f - B) + kAV \tag{3.42}$$

where V is the tank volume, F is the volumetric flow rate, k is the reaction rate constant, and the subscript f refers to feed concentrations of A and B. Notice that the concentration of B is dependent on both A and B, whereas the concentration of A is a function of A only. The open loop transfer functions for the two species are:

$$\bar{A}(s) = \left[\frac{K_1}{1+\tau_1 s}\right]\bar{A}_f(s) \tag{3.43}$$

$$\bar{B}(s) = \left[\frac{1}{1+\tau_2 s}\right]\bar{B}_f(s) + \left[\frac{K_1}{1+\tau_1 s}\right]\left[\frac{K_2}{1+\tau_2 s}\right]\bar{A}_f(s) \tag{3.44}$$

where,

$$K_1 = \frac{F}{F+kV}, \qquad K_2 = \frac{kV}{F},$$

$$\tau_1 = \frac{V}{F+kV}, \qquad \text{and} \qquad \tau_2 = \frac{V}{F}.$$

Depending on the relationship between the time constants, τ_1 and τ_2, the dynamic response of the two concentration profiles to a step change in A_f can be drastically different. Figures 3.6*a* and *b* show the effect of increasing the difference between the time constants. From the definitions of the time constants, this difference in τ_2/τ_1 can be achieved through differences between the reaction rate constant and the liquid flow rate.

Now consider a simplified spray etching system, consisting of one

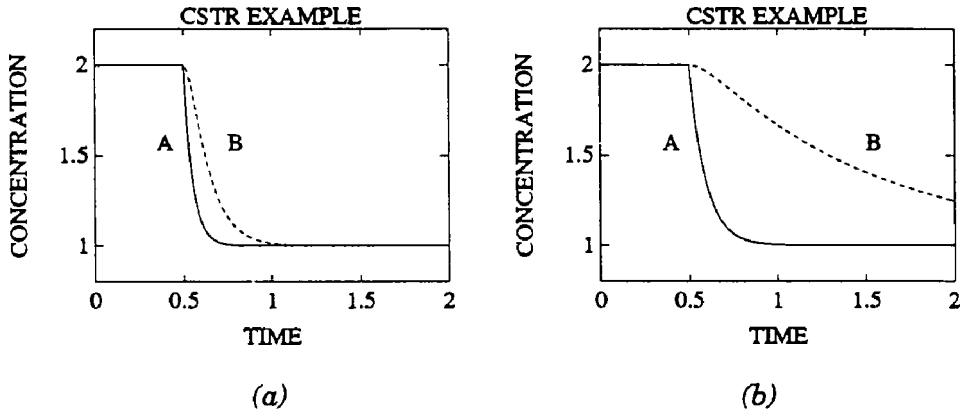

Figure 3.6: Response of exit stream composition to step change in reactant feed concentration A_f (*a*) $\tau_2/\tau_1 = 3$, (*b*) $\tau_2/\tau_1 = 21$

etcher/sump with a regenerator directly connected to the sump tank. Including a dilution and overflow stream with the sump tank and assuming pseudo-steady state in the etch chamber and the regenerator, the mass balances for Cu^{2+} (A) and Cu^{+} (B) are:

$$V_S \frac{dA_S}{dt} = -N_A + k_R B_S V_R - F_D A_S \tag{3.45}$$

$$V_S \frac{dB_S}{dt} = 2N_A - k_R B_S V_R - F_D B_S \tag{3.46}$$

Approximating the etch rate term, N_A, as a step change, u, when the board area is changed, the open loop transfer functions in the Laplace domain for the cupric and cuprous ion concentrations are:

$$\bar{A}_S(s) = \left[\frac{-K_1(s - z_1)}{(s - p_1)(s - p_2)}\right] \bar{u}(s) \tag{3.47}$$

$$\bar{B}_S(s) = \left[\frac{2K_1}{s - p_1}\right] \bar{u}(s) \tag{3.48}$$

where,

$$K_1 = \frac{1}{V_S}, \qquad z_1 = \frac{k_R V_R - F_D}{V_S},$$

$$p_1 = \frac{-(k_R V_R + F_D)}{V_S}, \quad \text{and} \quad p_2 = \frac{-F_D}{V_S}.$$

Both A_S and B_S have one pole in common, p_1. The reason for the sluggish dynamics in $[Cu^{2+}]$ (Figures 3.5*a* and *b*) can therefore be explained by a value of the dominant pole, p_2, that is much closer to zero than p_1 is. The dynamic response of the system can be made faster by forcing this pole to be more negative, which is accomplished by increasing the dilution stream flow rate, F_D.

The inverse response in the $[Cu^{2+}]$ profile (Figure 3.5*a*) is explained by a right-half-plane zero, z_1. This can be eliminated also by increasing F_D. The problem with increasing the flow rate of the dilution stream is that it will increase the rate of the overflow stream, which is not economical since this will increase the amount of waste. It therefore appears that in order to minimize waste production, the increased dynamic performance of the system must be sacrificed.

3.5 REFERENCES

Blumberg, L. R., D. D. Coolbaugh, J. A. Kurowski, and E. A. Stromecki, "Continuous Regeneration of Acid Solution", Patent No. 5,013,395 (1991).

Brian, P. L. T., J. E. Vivian, and A. G. Habib, "The Effect of the Hydrolysis Reaction Upon the Rate of Absorption of Chlorine into Water", *AIChE J.*, **8**, 205 (1962).

Danckwerts, P. V., "Gas Absorption Accompanied by Chemical Reaction", *AIChE J.*, **1**, 456 (1955).

Jhaveri, A. S. and M. M. Sharma, "Kinetics of Absorption of Oxygen in Aqueous Solutions of Cupric Chloride", *Chem. Eng. Sci.*, **22**, 1 (1967).

CHAPTER

FOUR

STATE ESTIMATION

4.1 INTRODUCTION

Some of the most important issues when addressing problems in stochastic control include prediction of random signals, separating random signals from random noise, and detecting signals of known forms (pulses, sinusoids) in the presence of random noise. The pioneering work of Kolmogorov (1941) and Wiener (1949) led to the development of the Wiener-Hopf integral equation. The solution of this integral equation is accomplished through spectral factorization, with the optimal filter being specified from its impulse response. This was recognized by many to not be a simple task and numerous alternative techniques of approaching the optimal filtering problem have since been proposed.

The classic papers by Kalman (1960) and Kalman and Bucy (1961) have produced one of the most useful theoretical and computationally feasible approaches to practical problems of estimation, filtering, and prediction. Their work avoided the direct solution to the Wiener-Hopf integral equation by using orthogonal projection to convert it into a nonlinear differential equation. The

solution of this equation yields the covariance matrix of the minimum filtering error, which contains all the information necessary for the design of the optimal filter. This approach produced the *Duality Principle*, which shows that the solutions of the optimal estimation problem and the optimal regulator problem are equivalent under the duality relations, thus providing a link between stochastic filter theory and deterministic control theory.

The result of their work was the introduction of the *Kalman filter*. A Kalman filter is simply an optimal recursive data processing algorithm. When properly designed, a Kalman filter is able to use all available measurements, regardless of their precision, to estimate the current value of the states of interest in a manner where the error is statistically minimized. Information that must be given to the estimator includes:

- the system and measurement dynamics (deterministic model),
- statistical descriptions of the system and measurement noise and the dynamic model uncertainty (covariance), and
- any available information about the initial conditions.

The recursive nature of the Kalman filter is advantageous because the filter will not require that all previous data be kept in storage and reprocessed each time a new measurement is taken.

The Kalman filter has been used in many applications for aerospace-related problems, such as satellite navigation (Battin and Levine, 1970) and missile trajectory estimation, in analytical chemistry for parameter estimation (Rutan and Brown, 1984), and is finding increased usage in the chemical engineering community working with such diverse areas as fixed-bed reactor control (Vakil *et al.*, 1973), emulsion polymerization (MacGregor *et al.*, 1986, Dimitratos *et al.*, 1989), biotechnology (Ramirez, 1987, Chattaway and

Stephanopoulos, 1989), optical photolithography (Carroll and Ramirez, 1990), and hazardous state detection (King and Gilles, 1990) as well as other chemical reactor control applications (Seinfeld, 1970, Wells, 1971, Kirparissides *et al.*, 1981). Because of its recursive structure and the increased availability of PCs and workstations with improved computational capabilities, the Kalman filter is ideally suited for on-line implementation for process monitoring and control.

4.2 KALMAN FILTER FUNDAMENTALS

As the Kalman filter has been carefully examined for its limitations and applicabilities by the scientific community, several alternative derivations have been presented. The following presentation of the linear case is a brief overview, based on several different approaches (Athans and Tse, 1967, Barham and Humphries, 1970, Rhodes, 1971), resulting in a less mathematically rigorous derivation than the original, but one that has an intuitive appeal for understanding the underlying theory. More complete treatments of the theory can be found in Gelb *et al.* (1974), Maybeck (1979), or Stengel (1986).

4.2.1 Optimum Combination of Independent Estimates

The objective of a Kalman filter is to combine two independent estimates of a state vector to form a weighted average. One of the estimates uses a process model to propagate the previous best estimate of the states across some sampling interval. This model is based on fundamental principles and equations of motion. The other estimate is obtained from measurements. The weighting factor is selected to yield a mean with minimum variance and hence maximum probability.

First consider the single-dimension case, where x_1 and x_2 represent two

independent estimates of a quantity x with variances σ_1^2 and σ_2^2, respectively. How can these two estimates be combined to form the best (minimum variance) estimate of x?

This can be determined through elementary statistical principles. Let the weighted mean, $\bar{x}$, be defined as:

$$\bar{x} = (1-w)x_1 + wx_2 \tag{4.1}$$

where w is a weighting factor. The expected value (mean) of x is given by,

$$E\{x\} = E\{\bar{x}\} = (1-w)E\{x_1\} + wE\{x_2\} \tag{4.2}$$

where $E\{\cdot\}$ refers to the expected value. By requiring that $E\{x\}=E\{\bar{x}\}$, $\bar{x}$ will be an unbiased estimate of x. The variance (σ^2) of the quantity $\bar{x}$ is defined by,

$$\sigma^2 = E\{[\bar{x} - E\{\bar{x}\}]^2\} \tag{4.3}$$

Since x_1 and x_2 are independent estimates, $[x_1-E\{x_1\}]$ and $[x_2-E\{x_2\}]$ are uncorrelated:

$$[x_1-E\{x_1\}][x_2-E\{x_2\}]^T = 0 \tag{4.4}$$

Substituting Equation (4.1) into (4.3),

$$\sigma^2 = (1-w)^2E\{[x_1-E\{x_1\}]^2\} + w^2E\{[x_2-E\{x_2\}]^2\} \tag{4.5}$$

or

$$\sigma^2 = (1-w)^2\sigma_1^2 + w^2\sigma_2^2 \tag{4.6}$$

In order to choose a value for w that minimizes the variance, Equation (4.6) can

be differentiated with respect to w:

$$\frac{\partial \sigma^2}{\partial w} = -2(1-w)\sigma_1{}^2 + 2w\sigma_2{}^2 = 0 \tag{4.7}$$

which is solved to yield the optimum value of the weighting factor:

$$w = \frac{\sigma_1{}^2}{\sigma_1{}^2 + \sigma_2{}^2} \tag{4.8}$$

Substituting into Equation (4.1),

$$\bar{x} = \frac{\sigma_2{}^2 x_1 + \sigma_1{}^2 x_2}{\sigma_1{}^2 + \sigma_2{}^2} \tag{4.9}$$

and into Equation (4.6),

$$\sigma^2 = \frac{\sigma_1{}^2 \sigma_2{}^2}{\sigma_1{}^2 + \sigma_2{}^2} \tag{4.10}$$

If x_2 is considered to be a measurement used to improve an updated estimate x_1, we rewrite Equation (4.9) as,

$$\bar{x} = x_1 + w(x_2 - x_1) \tag{4.11}$$

and, using Equation (4.8) to express σ_2 in terms of w and σ_1, (4.10) can be rewritten as,

$$\sigma^2 = \sigma_1{}^2(1-w) \tag{4.12}$$

These two equations show $\bar{x}$ being initially estimated as x_1 and subsequently

"updated" through the measurement, given by x_2. They also show the resulting change in the variance. Thus the weighted mean procedure can be separated into a prediction process followed by a correction process.

4.2.2 Linear State Estimation

Consider an nth order linear and time-varying dynamic system:

$$\dot{\mathbf{x}}(t) = \mathbf{A}(t)\mathbf{x}(t) + \mathbf{w}(t) \tag{4.13}$$

where $\mathbf{x}$ represents the state vector and $\mathbf{w}$ is a vector-valued white-noise Gaussian input with zero mean:

$$E\{\mathbf{w}(t)\} = \mathbf{0} \tag{4.14}$$

and covariance matrix, $\mathbf{Q}$,

$$E\{\mathbf{w}(t)\mathbf{w}^T(\tau)\} = \mathbf{Q}(t)\delta(t-\tau) \tag{4.15}$$

where $E\{\cdot\}$ refers to the expected value and $\delta(\cdot)$ is the Dirac delta function. The covariance matrix $\mathbf{Q}$ must be symmetric positive semidefinite.

Noise-corrupted outputs can be represented as functions of the states by the vector $\mathbf{z}$:

$$\mathbf{z}(t) = \mathbf{H}(t)\mathbf{x}(t) + \mathbf{n}(t) \tag{4.16}$$

where $\mathbf{n}$ is a Gaussian white-noise process with zero mean:

$$E\{\mathbf{n}(t)\} = \mathbf{0} \tag{4.17}$$

and covariance matrix, $\mathbf{R}$,

$$E\{\mathbf{n}(t)\mathbf{n}^T(\tau)\} = \mathbf{R}(t)\delta(t-\tau) \tag{4.18}$$

with $\mathbf{R}$ being a symmetric positive definite matrix. The vectors $\mathbf{w}$, $\mathbf{n}$, and $\mathbf{x}(t_0)$ are all assumed to be independent. By being represented as "white noise" processes, $\mathbf{w}$ and $\mathbf{n}$ are assumed to be uncorrelated in time. What this means is that knowledge of the value of the noise at one time is of no use when predicting its value at any other time.

Now consider the multi-dimentional case of what was presented in the previous section. Let $\mathbf{x}_1$ and $\mathbf{x}_2$ are two vectors of order n that represent independent estimates of the state vector $\mathbf{x}$. The weighted mean of $\mathbf{x}_1$ and $\mathbf{x}_2$ can be written as,

$$\bar{\mathbf{x}} = (\mathbf{I}-\mathbf{W})\mathbf{x}_1 + \mathbf{W}\mathbf{x}_2 \tag{4.19}$$

or

$$\bar{\mathbf{x}} = \mathbf{x}_1 + \mathbf{W}(\mathbf{x}_2-\mathbf{x}_1) \tag{4.20}$$

where $\mathbf{W}$ is an arbitrary $n\times n$ weighting matrix. Again, if $\mathbf{x}_2$ is considered to represent measurements of $\mathbf{x}_1$, we can define a measurement vector that is a linear combination of the states,

$$\mathbf{z}_2 = \mathbf{H}\mathbf{x}_2 \tag{4.21}$$

where $\mathbf{H}$ is an $m\times n$ matrix that operates on $\mathbf{x}$. Note that the number of measurements does not need to equal the number of states being estimated. Since $\mathbf{W}$ is an arbitrary matrix, we can select it to have the structure $\mathbf{W}=\mathbf{KH}$, where $\mathbf{K}$ is another arbirary weighting matrix. Rewriting Equation (4.20) in terms of $\mathbf{K}$,

$$\bar{\mathbf{x}} = \mathbf{x}_1 + \mathbf{K}(\mathbf{z}_2 - \mathbf{H}\mathbf{x}_1) = (\mathbf{I} - \mathbf{K}\mathbf{H})\mathbf{x}_1 + \mathbf{K}\mathbf{z}_2 \tag{4.22}$$

The covariance of $\bar{\mathbf{x}}$ is defined as,

$$\bar{\mathbf{P}} = E\{[\bar{\mathbf{x}} - E\{\bar{\mathbf{x}}\}][\bar{\mathbf{x}} - E\{\bar{\mathbf{x}}\}]^T\} \tag{4.23}$$

which, when combined with Equation (4.22) and recalling that $\mathbf{x}_1$ and $\mathbf{z}_2$ are uncorrelated, becomes:

$$\begin{aligned}\bar{\mathbf{P}} = (\mathbf{I} - \mathbf{K}\mathbf{H})E\{[\mathbf{x}_1 - E\{\mathbf{x}_1\}][\mathbf{x}_1 - E\{\mathbf{x}_1\}]^T\}(\mathbf{I} - \mathbf{K}\mathbf{H})^T \\ + \mathbf{K}E\{[\mathbf{z}_2 - E\{\mathbf{z}_2\}][\mathbf{z}_2 - E\{\mathbf{z}_2\}]^T\}\mathbf{K}^T\end{aligned} \tag{4.24}$$

Defining the covariance of $\mathbf{x}_1$ to be $\mathbf{P}$ and the covariance of $\mathbf{y}_2$ to be $\mathbf{R}$,

$$\bar{\mathbf{P}} = (\mathbf{I} - \mathbf{K}\mathbf{H})\mathbf{P}(\mathbf{I} - \mathbf{K}\mathbf{H})^T + \mathbf{K}\mathbf{R}\mathbf{K}^T \tag{4.25}$$

which can be expanded to give,

$$\bar{\mathbf{P}} = \mathbf{P} + \mathbf{K}(\mathbf{H}\mathbf{P}\mathbf{H}^T + \mathbf{R})\mathbf{K}^T - \mathbf{K}(\mathbf{H}\mathbf{P}) - (\mathbf{H}\mathbf{P})^T\mathbf{K}^T \tag{4.26}$$

We must now determine the value of $\mathbf{K}$ that will minimize $\bar{\mathbf{P}}$. Consider the relation,

$$(\mathbf{K}\mathbf{S} - \mathbf{D})(\mathbf{K}\mathbf{S} - \mathbf{D})^T = \mathbf{K}(\mathbf{S}\mathbf{S}^T)\mathbf{K}^T - \mathbf{K}(\mathbf{S}\mathbf{D}^T) - (\mathbf{S}\mathbf{D}^T)^T\mathbf{K}^T + \mathbf{D}\mathbf{D}^T \tag{4.27}$$

If we define the matrices $\mathbf{S}$ and $\mathbf{D}$ such that,

$$\mathbf{S}\mathbf{S}^T = \mathbf{H}\mathbf{P}\mathbf{H}^T + \mathbf{R} \tag{4.28}$$

$$\mathbf{SD}^T = \mathbf{HP} \tag{4.29}$$

then

$$\mathbf{DD}^T = (\mathbf{DS}^T)(\mathbf{SS}^T)^{-1}(\mathbf{SD}^T) = \mathbf{PH}^T(\mathbf{HPH}^T+\mathbf{R})^{-1}\mathbf{HP} \tag{4.30}$$

and substitution into Equation (4.26) gives,

$$\bar{\mathbf{P}} = \mathbf{P} + (\mathbf{KS}-\mathbf{D})(\mathbf{KS}-\mathbf{D})^T - \mathbf{PH}^T(\mathbf{HPH}^T+\mathbf{R})^{-1}\mathbf{HP} \tag{4.31}$$

From this relationship, we see that, with respect to the matrix $\mathbf{K}$, $\bar{\mathbf{P}}$ is minimized when $(\mathbf{KS}-\mathbf{D})=\mathbf{0}$. Therefore,

$$\mathbf{K} = \mathbf{DS}^{-1} = (\mathbf{DS}^T)(\mathbf{SS}^T)^{-1} = \mathbf{PH}^T(\mathbf{HPH}^T+\mathbf{R})^{-1} \tag{4.32}$$

Substituting into Equation (4.31),

$$\bar{\mathbf{P}} = \mathbf{P} - \mathbf{KHP} \tag{4.33}$$

which is the covariance for the best estimate of $\mathbf{x}$:

$$\bar{\mathbf{x}} = \mathbf{x}_1 - \mathbf{K}(\mathbf{z}_2-\mathbf{H}\mathbf{x}_1) \tag{4.34}$$

This equation represents the basic structure of the linear Kalman filter. The matrix $\mathbf{K}$ is known as the Kalman gain matrix. The first term on the right-hand-side is a prediction of the states based on a dynamic model, while the second term corrects the prediction, depending on how much the predicted values of the measurements differ from the actual values. This *predictor-corrector* structure is illustrated in Figure 4.1.

Because the covariance in Equation (4.23) is analagous to the performance

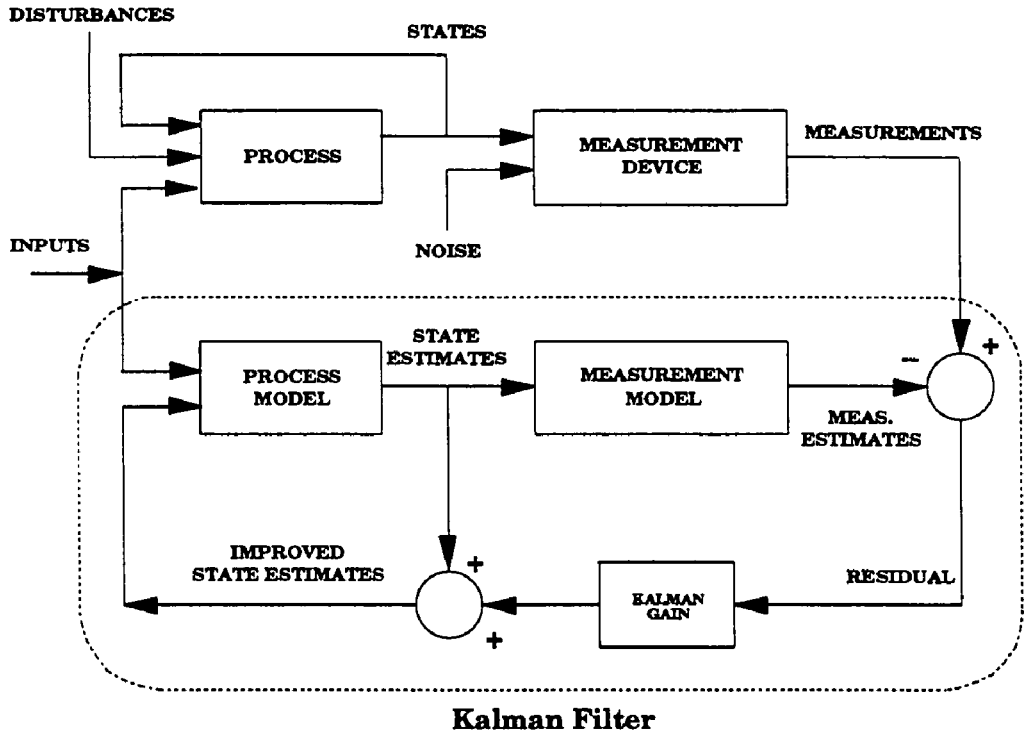

Figure 4.1: Structure of the Kalman Filter

index that is minimized in optimal control theory (Takahashi *et al.*, 1972), the covariance matrix is found to satisfy the matrix Ricatti differential equation:

$$\dot{\mathbf{P}} = \mathbf{AP} + \mathbf{PA}^T + \mathbf{Q} - \mathbf{KHP} \tag{4.35}$$

The first three terms on the right-hand-side of Equation (4.35) predict the dynamic behavior of the covariance. The first two terms, $\mathbf{AP} + \mathbf{PA}^T$, are based on the model of the process and represent dissipation in the uncertainty as the model is propagated. The third term, $\mathbf{Q}$, accounts for the uncertainty in the model, increasing the error. The last term, which depends on the Kalman gain

matrix, is used to correct the covariance propagation when the state estimates are updated after availability of new measurements.

4.2.3 Hybrid Extended Kalman Filter

The standard Kalman filter presented in the previous section uses a linear model of the process. For nonlinear systems, a variation known as an *extended Kalman filter* (EKF) can be used. The extended filter uses a local linearization around the current state estimates for propagation. For sampled-data systems, where discrete measurements of a continuous process are taken, a *hybrid extended Kalman filter* (HEKF), which combines continuous propagation with discrete estimate corrections, is most appropriate (Stengel, 1986). The dynamic behavior of the states (order n) of a process are represented as:

$$\dot{\mathbf{x}}(t) = \mathbf{f}\{\mathbf{x}(t)\} + \mathbf{w}(t) \tag{4.36}$$

Available noise-corrupted measurements (order m) that are functions of the state variables are modeled as:

$$\mathbf{z}(t) = \mathbf{h}\{\mathbf{x}(t)\} + \mathbf{n}(t) \tag{4.37}$$

Equations (4.36) and (4.37) are the nonlinear equivalents of Equations (4.13) and (4.16), respectively.

Given an initial estimate of the system covariance, the estimates of the states, $\bar{\mathbf{x}}$, and the associated covariances, $\mathbf{P}$, are integrated using the process model across the sampling time interval:

State Estimate Propagation

$$\bar{\mathbf{x}}[t_k|t_{k-1}] = \bar{\mathbf{x}}[t_{k-1}|t_{k-1}] + \int_{t_{k-1}}^{t_k} \mathbf{f}\{\bar{\mathbf{x}}(\tau)\}\, d\tau \tag{4.38}$$

Covariance Estimate Propagation

$$\mathbf{P}[t_k|t_{k-1}] = \mathbf{P}[t_{k-1}|t_{k-1}] + \int_{t_{k-1}}^{t_k} [\mathbf{F}(\tau)\mathbf{P}(\tau) + \mathbf{P}(\tau)\mathbf{F}^T(\tau) + \mathbf{Q}(\tau)]\, d\tau \tag{4.39}$$

where $\mathbf{F}$ is the $n \times n$ Jacobian matrix of the dynamic process model with respect to the states:

$$\mathbf{F}(t) = \frac{\partial \mathbf{f}(\cdot)}{\partial \mathbf{x}} \tag{4.40}$$

and the partial derivative matrices are evaluated at current values of $\bar{\mathbf{x}}$. The time interval between t_{k-1} and t_k refers to the sampling interval. The notation $[t_k|t_{k-1}]$ represents propagation across the sampling interval, while $[t_k|t_k]$ indicates an estimate update at the end of the sampling interval. Equations (4.38) and (4.39) are subject to the initial conditions:

$$E\{\mathbf{x}(0)\} = \bar{\mathbf{x}}_0 \tag{4.41}$$

$$E\{[\mathbf{x}(0) - \bar{\mathbf{x}}_0][\mathbf{x}(0) - \bar{\mathbf{x}}_0]^T\} = \mathbf{P}_0 \tag{4.42}$$

When new measurements become available, the $n \times m$ Kalman gain matrix, $\mathbf{K}$, which weights the extent of the correction to the state vector estimate, is calculated:

Filter Gain Computation

$$\mathbf{K}(t_k) = \mathbf{P}[t_k|t_{k-1}]\mathbf{H}^T(t_k)\{\mathbf{H}(t_k)\mathbf{P}[t_k|t_{k-1}]\mathbf{H}^T(t_k) + \mathbf{R}(t_k)\}^{-1} \tag{4.43}$$

where $\mathbf{H}$ is the $m \times m$ Jacobian matrix of the observation model with respect to the states:

$$\mathbf{H}(t) = \frac{\partial \mathbf{h}(\cdot)}{\partial \mathbf{x}} \tag{4.44}$$

The difference between the measurement data ($\mathbf{z}$) and that predicted by the observation model ($\mathbf{h}$) is an indication of the error in the estimate. The Kalman filter uses this residual to update and improve its estimates:

State Estimate Update

$$\bar{\mathbf{x}}[t_k|t_k] = \bar{\mathbf{x}}[t_k|t_{k-1}] + \mathbf{K}(t_k)\{\mathbf{z}(t_k) - \mathbf{h}(\bar{\mathbf{x}}[t_k|t_{k-1}])\} \tag{4.45}$$

Covariance Estimate Update

$$\mathbf{P}[t_k(+)] = [\mathbf{I} - \mathbf{K}(t_k)\mathbf{H}(t_k)]\mathbf{P}[t_k|t_{k-1}] \tag{4.46}$$

The hybrid filter uses the linearized process and observation models for calculation of the covariance and gain matrices, but retains the nonlinear forms for state propagation and definition of the output vector.

4.2.4 Proportional-Integral State Estimation

The methodology of Kalman filtering is based on the assumption that the true process can deviate from the deterministic process model by a zero-mean, random component, which is represented through the addition of zero-mean, white noise. Sustained nonzero-mean (biased) disturbances do not fall in this category of deviations. In the presence of such a disturbance, the estimates from a standard Kalman filter, which is proportional by nature, will display a

certain degree of bias from the true values of the states (Asher *et al.*, 1976).

This type of behavior is also observed in proportional controllers. For zero-mean disturbances, the action from a P controller will bring the controlled variable back to its setpoint. However, for sustained disturbances or changes in setpoint, the controller action will result in offset from the setpoint. This bias is corrected through the addition of integral action, which drives the controlled variable back to its setpoint (Luyben, 1990).

Similar integral action can be included with a Kalman filter. This is accomplished by augmenting the state vector with a parameter vector:

$$\mathbf{x}_A(t) = \begin{bmatrix} \mathbf{x}(t) \\ \mathbf{p}(t) \end{bmatrix} \tag{4.47}$$

where $\mathbf{p}$ is a vector of parameters represented as random processes, used to account for the effect of unmeasured disturbances and modeling errors on the deterministic states (MacGregor *et al.*, 1986). The augmented system is of order p. The parameters can be poorly known (or unknown) model parameters (such as rate constants) or operating parameters that are subject to unmodeled disturbances, but should be selected so that the observability of the system is retained by their inclusion. In other words, the dynamic behavior of the states should be dependent on the parameters as well as on the states. When deciding which parameters to include, one should consider which parameters have the greatest influence on the values of the states or are the most susceptible to process disturbances.

The model of the augmented state vector is given by:

$$\dot{\mathbf{x}}_A(t) = \mathbf{f}_A[\mathbf{x}(t), \mathbf{p}(t)] + \mathbf{w}_A(t) \tag{4.48}$$

which can be separated in terms of the original state vector and the parameter

vector:

$$\dot{\mathbf{x}}(t) = \mathbf{f}_1\{\mathbf{x}(t), \mathbf{p}(t)\} + \mathbf{w}_1(t) \tag{4.49}$$

$$\dot{\mathbf{p}}(t) = \mathbf{w}_2(t) \tag{4.50}$$

where $\mathbf{w}_1$ and $\mathbf{w}_2$ are Gaussian, white noise processes. The additional parameters are represented as "random walk" processes. The observation equation, based on the augmented state vector, becomes:

$$\mathbf{z}(t) = \mathbf{h}_A\{\mathbf{x}(t), \mathbf{p}(t)\} + \mathbf{n}(t) \tag{4.51}$$

Therefore, the parameter vector, $\mathbf{p}(t)$, that is used in the process and measurement models (Equations (4.49) and (4.51)) is obtained through the integration of Equation (4.50). Thus the state augmentation has introduced integral action into the the estimation routine, as illustrated in Figure 4.2.

State propagation is carried out by integrating Equation (4.48) across the sampling interval,

State Estimate Propagation

$$\bar{\mathbf{x}}_A[t_k|t_{k-1}] = \bar{\mathbf{x}}_A[t_{k-1}|t_{k-1}] + \int_{t_{k-1}}^{t_k} \mathbf{f}_A\{\bar{\mathbf{x}}_A(\tau)\}\, d\tau \tag{4.52}$$

and the corresponding covariance integrated similarly,

Covariance Estimate Propagation

$$\mathbf{P}_A[t_k|t_{k-1}] = \mathbf{P}_A[t_{k-1}|t_{k-1}] + \int_{t_{k-1}}^{t_k} [\mathbf{F}_A(\tau)\mathbf{P}_A(\tau) + \mathbf{P}_A(\tau)\mathbf{F}_A{}^T(\tau) + \mathbf{Q}_A(\tau)]\, d\tau \tag{4.53}$$

where the augmented system's $p \times p$ Jacobian matrix $\mathbf{F}_A$ is defined by:

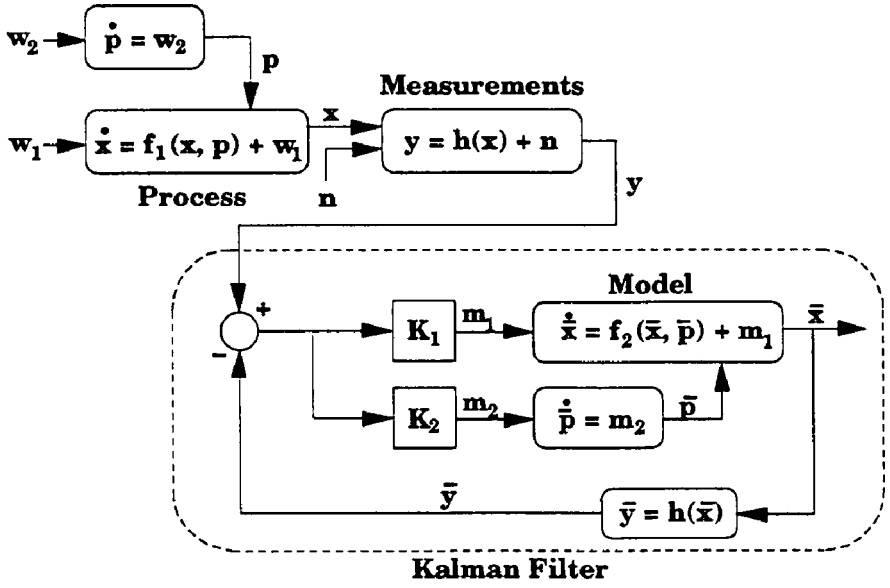

Figure 4.2: Proportional-Integral Kalman Filter

$$\mathbf{F}_A(t) = \begin{bmatrix} \mathbf{F}_1(t) & \mathbf{F}_2(t) \\ \mathbf{0} & \mathbf{0} \end{bmatrix} \tag{4.54}$$

For these equations, $\mathbf{F}_1$ is the Jacobian matrix defined in Equation (4.40), $\mathbf{F}_2$ is defined as:

$$\mathbf{F}_2(t) = \frac{\partial \mathbf{f}_A(\cdot)}{\partial \mathbf{p}} \tag{4.55}$$

At the end of the sampling interval, the augmented $p \times m$ Kalman gain matrix, defined by:

$$\mathbf{K}_A(t) = \begin{bmatrix} \mathbf{K}_1(t) \\ \mathbf{K}_2(t) \end{bmatrix} \tag{4.56}$$

is calculated as:

$$\mathbf{K}_A(t_k) = \mathbf{P}_A[t_k|t_{k-1}]\mathbf{H}_A{}^T(t_k)\{\mathbf{H}_A(t_k)\mathbf{P}_A[t_k|t_{k-1}]\mathbf{H}_A{}^T(t_k) + \mathbf{R}(t_k)\}^{-1} \tag{4.57}$$

with the augmented measurement Jacobian matrix, $\mathbf{H}_A$, defined as:

$$\mathbf{H}_A(t) = [\mathbf{H}_1(t) \quad \mathbf{H}_2(t)] \tag{4.58}$$

where $\mathbf{H}_1$ is the Jacobian matrix defined in Equation (4.44) and $\mathbf{H}_2$ is

$$\mathbf{H}_2(t) = \frac{\partial \mathbf{h}_A(\cdot)}{\partial \mathbf{p}} \tag{4.59}$$

When the measurements become available, the augmented state vector and covariance matrix are updated:

State Estimate Update

$$\bar{\mathbf{x}}_A[t_k|t_k] = \bar{\mathbf{x}}_A[t_k|t_{k-1}] + \mathbf{K}_A(t_k)\{\mathbf{z}(t_k) - \mathbf{h}_A(\bar{\mathbf{x}}_A[t_k|t_{k-1}])\} \tag{4.60}$$

Covariance Estimate Update

$$\mathbf{P}_A[t_k(+)] = [\mathbf{I} - \mathbf{K}_A(t_k)\mathbf{H}_A(t_k)]\mathbf{P}_A[t_k|t_{k-1}] \tag{4.61}$$

The performance of this *proportional-integral Kalman filter* (PIKF) is controlled through the definition of the noise vector $\mathbf{w}_2$. Small elements in this vector correspond to small values in $\mathbf{K}_2$, which will result in slow, smooth adaptation of the unknown parameters, while large elements will allow for a rapid but less smooth transition.

4.3 AVAILABLE MEASUREMENTS

Wet chemical etching is, by nature, associated with a degree of isotropic etching, as discussed in Chapter 2. The extent of the etch undercut can be controlled by limiting the contact between the etching solution and the boards. In order to accomplish this and etch consistent products, maintenance of a constant etch rate in the etch chambers is important. In order to control the etch rate, the Cu^{2+} and Cu^{+} concentrations in the sump tank must be known. Since these concentrations cannot be directly measured on-line, they must be estimated using a Kalman filter.

The available measurements are the final measured etch factors of the boards as they are removed from the process line and the oxidation-reduction potential (ORP) of the solution in the bulk tank and each of the sump tanks. The ORP of the reaction:

$$Cu^{2+} + e^{-} \rightarrow Cu^{+} \tag{4.62}$$

is related to the ratio of the cupric and cuprous ion concentrations by the Nernst equation (Atkins, 1982):

$$E = E' + \frac{RT}{F} ln \frac{[Cu^{2+}]}{[Cu^{+}]} \tag{4.63}$$

where E is the oxidation-reduction potential, E' is the potential at standard conditions, R is the ideal gas constant, T is the temperature in degrees Kelvin, and F is Faraday's constant.

With respect to the boards coming off of the line, the parameters that can be measured at selected sampling positions on the board are the top line width (*TLW*) and the bottom line width (*BLW*) on either side. Information associated

with the board are the mask line width (*MLW*) and plating thickness (*PT*). Both the top and bottom lines will have a certain degree of undercut, designated *TLU* and *BLU*, respectively. The etch undercut can in turn be related to the lateral etch rates:

$$TLU = \frac{MLW - TLW}{2} = \int_0^{t_{res}} r_{LET}\, d\tau \tag{4.64}$$

$$BLU = \frac{MLW - BLW}{2} = \int_{t_{BT}}^{t_{res}} r_{LEB}\, d\tau \tag{4.65}$$

The residence time is defined as,

$$t_{res} = \sum_{i=1}^{3} \frac{L_{Ei}}{u_{con}} \tag{4.66}$$

If the etch rates do not change significantly during the residence time of the boards in the etch line, the breakthrough time can be approximated by the relation,

$$t_{BT} = \frac{PT}{r_{VE}} \tag{4.67}$$

Substituting Equations (4.66) and (4.67) into Equations (4.64) and (4.65), expressions for the top and bottom width are as follow:

$$TLW = MLW - 2r_{LET}t_{res} = MLW - 2r_{LET}\sum_{i=1}^{3} \frac{L_{Ei}}{u_{con}} \tag{4.68}$$

$$BLW = MLW - 2r_{LEB}(t_{res} - t_{BT}) = MLW - 2r_{LEB}\left[\sum_{i=1}^{3} \frac{L_{Ei}}{u_{con}} - \frac{PT}{r_{VE}}\right] \tag{4.69}$$

The observation vector to be used will include the ORP in the three sumps and

in the bulk tank and the bottom and top line widths for both sides of the boards.

4.4 ISSUES IN FILTER DESIGN

Kalman filters have been used extensively for applications in navigation and tracking, where the models are well known and measurements are generally available continuously. However, they have only found limited usage for chemical engineering problems because of the differences in the nature of the applications. Some of the difficulties that have been encountered when applying the methodology to chemical reactor systems include accommodating infrequently sampled measurements, measurement lag, and process-model mismatch.

The on-line measurements of ORP are available continuously while off-line measurements of etch undercut and etch angle are less frequent. In addition to being infrequent, there is also a period of time between when the boards leave the etch chambers and when the measurements are actually available. This measurement lag is due to the time needed to strip off the photoresist, rinse the boards, remove them from the line, and optically examine and measure the etch profile. In order to account for the infrequency and delay of these measurements, the hybrid extended Kalman filter algorithm as described previously must be modified.

4.4.1 Combining Infrequent with Frequent Measurements

The problem of compensating for multirate measurement sampling was approached in a similar manner as was taken by Lennartson (1989), where different observation vectors containing the frequent measurements were defined that either included the infrequent measurements or not, depending on the sampling period. The augmented vector and its associated measurement covariance matrix are used periodically when the infrequent measurements become available.

Both the measurement Jacobian matrix **H** and the measurement covariance matrix **R** in Equation (4.43) correspond to the frequent measurements of ORP:

$$\mathbf{H}(t_k) = \mathbf{H}_F(t_k) \tag{4.70}$$

$$\mathbf{R}(t_k) = \mathbf{R}_F(t_k) \tag{4.71}$$

When the infrequent measurements become available and the observation vector (**z**) is augmented, both **H** and **R** must also be augmented:

$$\mathbf{H}(t_{IF}) = \begin{bmatrix} \mathbf{H}_F \\ \mathbf{H}_{IF} \end{bmatrix} \tag{4.72}$$

$$\mathbf{R}(t_{IF}) = \begin{bmatrix} \mathbf{R}_F & \mathbf{0} \\ \mathbf{0} & \mathbf{R}_{IF} \end{bmatrix} \tag{4.73}$$

where t_{IF} refers to the time at which the infrequent measurement is taken plus the measurement lag. These augmented matrices are then used in Equation (4.43) for calculation of the gain matrix:

$$\mathbf{K}(t_{IF}) = [\mathbf{K}_F \quad \mathbf{K}_{IF}] \tag{4.74}$$

An alternative approach to this issue is to adjust the Kalman filter

algorithm such that during the sampling times when the frequent measurements are taken but the infrequent measurements are not, the diagonal elements of $\mathbf{R}$ corresponding to the infrequent measurements are set to infinitely large values (Andrisani and Gau, 1987). These large terms in $\mathbf{R}$ will have the effect of informing the filter that no values are available for those particular measurements.

If we examine the structure of the gain matrix, we can find that these two methods are equivalent. Substituting Equations (4.74) and (4.73) into (4.43) at an instance when both sets of measurements are available,

$$\mathbf{K}(t_{IF}) = \mathbf{P}[\mathbf{H}_F^T \quad \mathbf{H}_{IF}^T]\begin{bmatrix}\mathbf{H}_F\mathbf{P}\mathbf{H}_F^T+\mathbf{R}_F & \mathbf{H}_F\mathbf{P}\mathbf{H}_{IF}^T \\ \mathbf{H}_{IF}\mathbf{P}\mathbf{H}_F^T & \mathbf{H}_{IF}\mathbf{P}\mathbf{H}_{IF}^T+\mathbf{R}_{IF}\end{bmatrix}^{-1} \tag{4.75}$$

The inverse of the partitioned matrix in this equation can be evaluated by considering the following matrix, $\mathbf{A}$:

$$\mathbf{A} = \begin{bmatrix}\mathbf{A}_{11} & \mathbf{A}_{12} \\ \mathbf{A}_{21} & \mathbf{A}_{22}\end{bmatrix} \tag{4.76}$$

Provided that $\mathbf{A}_{11}$ is nonsingular, the inverse of $\mathbf{A}$ is (Ayres, 1962):

$$\mathbf{A}^{-1} = \begin{bmatrix}\mathbf{A}_{11}^{-1}+(\mathbf{A}_{11}^{-1}\mathbf{A}_{12})\xi^{-1}(\mathbf{A}_{21}\mathbf{A}_{11}^{-1}) & -\xi^{-1}(\mathbf{A}_{21}\mathbf{A}_{11}^{-1}) \\ -(\mathbf{A}_{11}^{-1}\mathbf{A}_{12})\xi^{-1} & \xi^{-1}\end{bmatrix} \tag{4.77}$$

where $\xi = \mathbf{A}_{22}-\mathbf{A}_{21}(\mathbf{A}_{11}^{-1}\mathbf{A}_{12})$.

At any time when only the frequent measurements are available, the diagonal terms of $\mathbf{R}_{IF}$ (and hence, ξ from Equation (4.77)) can be taken to be infinitely large. Therefore, as $diag(\mathbf{R}_{IF}) \rightarrow \infty$,

$$\begin{bmatrix}\mathbf{H}_F\mathbf{P}\mathbf{H}_F^T+\mathbf{R}_F & \mathbf{H}_F\mathbf{P}\mathbf{H}_{IF}^T \\ \mathbf{H}_{IF}\mathbf{P}\mathbf{H}_F^T & \mathbf{H}_{IF}\mathbf{P}\mathbf{H}_{IF}^T+\mathbf{R}_{IF}\end{bmatrix}^{-1} \rightarrow \begin{bmatrix}\{\mathbf{H}_F\mathbf{P}\mathbf{H}_F^T+\mathbf{R}_F\}^{-1} & \mathbf{0} \\ \mathbf{0} & \mathbf{0}\end{bmatrix} \tag{4.78}$$

which, when substituted into Equation (4.75), reduces to Equation (4.70). Therefore the two methods are equivalent. Since the second method is computationally more demanding because of the larger matrices involved, we opted to use the former method.

4.4.2 Compensation for Measurement Lag

The issue of compensating for measurement lag is addressed by considering the following case. Assume the infrequent measurement is taken at $t=t_M$, while the actual value of this observation is not available until $t=t_U$. The previous update of the states and covariance had occurred at $t=t_0$. Throughout this time interval, frequent measurements are available and are used to update the states as best as possible. To simplify the notation for this section, any propagation steps will implicitly include the associated updates from the frequent measurements.

For the ideal situation, where there is no measurement lag, the states are propagated and updated by the frequent measurements over the infrequent measurement sampling interval,

$$\bar{\mathbf{x}}\,[t_M|t_0] = \bar{\mathbf{x}}\,[t_0|t_0] + \int_{t_0}^{t_M} \mathbf{f}\{\bar{\mathbf{x}}\,(\tau)\}\,d\tau \tag{4.79}$$

When the infrequent measurements are taken, they are used to immediately update the state estimates,

$$\bar{\mathbf{x}}\,[t_M|t_M] = \bar{\mathbf{x}}\,[t_M|t_0] + \mathbf{K}(t_M)\{\mathbf{z}(t_M) - \mathbf{h}(\bar{\mathbf{x}}\,[t_M|t_0])\} \tag{4.80}$$

where $\mathbf{K}$ is defined by Equation (4.43). and the states are then propagated to

$t=t_U$ using the updated states.

$$\bar{\mathbf{x}}\,[t_U|t_M] = \bar{\mathbf{x}}\,[t_M|t_M] + \int_{t_M}^{t_U} \mathbf{f}\{\bar{\mathbf{x}}\,(\tau)\}\,d\tau \tag{4.81}$$

As we used before, the notation $[t_k|t_{k-1}]$ represents propagation across the sampling interval, while $[t_k|t_k]$ indicates an estimate update at the end of the sampling interval.

In the presence of measurement lag, the states might be propagated with only the frequent measurements until the infrequent measurements are available (at $t=t_U$)

$$\bar{\mathbf{x}}\,[t_U|t_0] = \bar{\mathbf{x}}\,[t_0|t_0] + \int_{t_0}^{t_U} \mathbf{f}\{\bar{\mathbf{x}}\,(\tau)\}\,d\tau \tag{4.82}$$

at which point the infrequent update can be applied based on the residual from $t=t_M$:

$$\bar{\mathbf{x}}\,[t_U|t_U] = \bar{\mathbf{x}}\,[t_U|t_0] + \mathbf{K}(t_M)\{\mathbf{z}(t_M) - \mathbf{h}(\bar{\mathbf{x}}\,[t_M|t_0])\} \tag{4.83}$$

The effect of treating the measurement lag in this fashion is in the propagation that occurs between t_M and t_U. What is lost by the lag is the contribution of the infrequent measurement to the updated state values for the state propagation from t_M to t_U:

$$\Delta\mathbf{x} = \bar{\mathbf{x}}\,[t_U|t_M] - \bar{\mathbf{x}}\,[t_U|t_U] = \int_{t_M}^{t_U} \mathbf{f}\{\bar{\mathbf{x}}\,[\tau(+)]\} - \mathbf{f}\{\bar{\mathbf{x}}\,[\tau(-)]\}\,d\tau \tag{4.84}$$

where the notation (–) indicates that the infrequent update of the state and

covariance have not yet occured, while (+) indicates updated values based on the most recent measurements, both frequent and infrequent.

In order to treat the measurement lag rigorously, the state estimates at $t=t_M$ and all of the frequent measurements taken during the period between t_M and t_U would have to be stored. Then, as soon as the infrequent measurement becomes available at $t=t_U$, Equation (4.80) would be used to find the best estimates of $\bar{\mathbf{x}}(t_M)$ and Equation (4.81) would be used to propagate the states to $t=t_U$, including also the contributions of the stored frequent measurements in this interval. The need to include this correction factor is dependent on the extent of the dependence of the system dynamics on the states. This becomes important when working with nonlinear systems. Because of the slow dynamics associated with the spray etching system, Equations (4.82) and (4.83) were used for the infrequent measurement-based state updates.

4.4.3 Observability Considerations

A requirement for the successful design of any estimator of the states of a process is that the system be observable from the available measurements. Intuitively, a system is *cause-and-effect observable* if any change in each state has an effect on some output variable, which allows the cause to be detected. Being cause-and-effect observable is a necessary but not sufficient condition for deterministic observability. If a system does not satisfy cause-and-effect observability, this violation is sufficient to conclude that the system is unobservable. In these cases, more sensitive or additional measurements are necessary.

Deterministic observability can be determined by calculating the observability test matrix (Friedland, 1986):

$$\mathbf{G} = [\,\mathbf{H}^T \mid \mathbf{F}^T\mathbf{H}^T \mid (\mathbf{F}^T)^2\mathbf{H}^T \mid \cdots \mid (\mathbf{F}^T)^{n-1}\mathbf{H}^T\,] \tag{4.85}$$

where n is the order of the system. The system is observable if and only if the rank of $\mathbf{G}$ is equal to n. The most generally reliable method of determining the rank of a matrix numerically is through the use of singular value decomposition (Laub, 1985). The rank of the matrix $\mathbf{G}$ is equal to the number of nonzero singular values, which are the positive square roots of the eigenvalues of $\mathbf{G}\mathbf{G}^T$.

In addition to satisfying the conditions for deterministic observability, which indicates whether changes in the desired states can be detected by perfect measurements, we must also consider the issue of *stochastic observability*. This test for observability explicitly takes into account the uncertainty in the measurements by using the inverse covariance. A system that is "weakly" observable in a deterministic sense may become unobservable in the presence of measurement noise that is large enough in magnitude to render the changes in the states undetectable. Testing for stochastic observability requires the calculation of the *information matrix*, Λ (Jazwinski, 1970):

$$\Lambda(t_k,t_0) = \sum_{i=1}^{k} \Phi^T(t_k,t_0)\mathbf{H}^T(t)\mathbf{R}^{-1}(t)\mathbf{H}(t)\Phi(t_k,t_0) \tag{4.86}$$

where Φ is the *state transition matrix*, defined by the solutions of the following differential equation and initial condition:

$$\frac{d}{dt}\Phi(t,t_0) = \mathbf{F}(t)\Phi(t,t_0) \tag{4.87}$$

$$\Phi(t_0,t_0) = \mathbf{I} \tag{4.88}$$

Assuming $\mathbf{F}$ to be relatively constant over the sampling time interval, the solution to Equation (4.87) is:

$$\Phi(t,t_0) = e^{\mathbf{F}(t-t_0)} \tag{4.89}$$

where the matrix exponential is approximated through truncation of the series definition:

$$e^{\mathbf{F}(t-t_0)} = \mathbf{I} + \mathbf{F}(t-t_0) + \frac{1}{2!}\mathbf{F}^2(t-t_0)^2 + \cdots \tag{4.90}$$

The singular values of the information matrix indicate the preciseness of the state estimates. The larger the singular values of Λ, the smaller the eigenvalues of the covariance matrix, and the more precise the estimate. The information matrix must be of full rank for a system to be stochastically observable.

While observability is a prerequisite for acceptable state estimator design, it is not a sufficient condition for successful performance. Observability will only indicate whether changes in the states *as represented by the model* can be detected through the measurement model, given the extent of measurement uncertainty. Models used to represent any process will generally incorporate a number of assumptions for approximating reality into a mathematically manageable form. These assumptions and simplifications result in a certain degree of process-model mismatch, which is one of the issues that the state estimator must overcome in order to yield acceptable performance. Since the process itself is not used when determining observability, process-model mismatch is not taken into consideration. Using models that are deterministically and stochastically observable but poorly represent the actual process will degrade the performance of the filter and lead to filter divergence (Schlee *et al.*, 1967, Fitzgerald, 1971). Therefore care must be taken to ensure

the model is fairly accurate and is not overly simplified to the point where its usefulness to the filter is nullified.

4.5 RESULTS AND DISCUSSION

In the absence of actual plant data, separate versions of the model developed in the previous chapters are used to represent the "true" process and the process model. The difference between these two versions represent the process-model mismatch. Several different filter designs will be discussed in this chapter to accommodate different degrees of process-model mismatch.

For the results presented here, the sampling interval used for ORP measurements is 30 seconds, while etch profile measurements are taken every 20 minutes and subject to a 5 minute lag before these values are made available to the Kalman filter. This lag time is due to the time required for rinsing the boards, stripping the photoresist off the surface, drying the boards, and manually inspecting the line widths. These sampling intervals were selected as indicative of what is realistic in current practice. The states estimated are the concentrations of Cu^{2+} (A) and Cu^{+} (B) in each of the three sump tanks, the bulk tank, and the regenerator.

For each of the cases discussed, the scenario that is simulated is a 240 minute period during which three different board types are processed. The process is initially running at a conveyor speed of 1.75 m/min. The top and bottom spray pressures are 30 and 20 psi, respectively. Since the initial composition is not always precisely known (without performing a titration before every job), the initial conditions used by the filter are taken to be 80% of the true values used in the process. The initial conditions of the process and the filter are summarized in Table 4-1. The boards being etched have 20% of the

board area masked and an average mask line width of 140 μm. At t=90 minutes, the board type was switched to one with 25% masked area and an average mask line width of 160 μm, and at 150 minutes, the boards were switched again to boards with 10% masked area and 130 μm lines.

Table 4-1: Summary of Initial Conditions

	Process		Model	
Location	$[Cu^{2+}]$	$[Cu^{+}]$	$[Cu^{2+}]$	$[Cu^{+}]$
Sump Tank 1	5.580	0.300	4.464	0.240
Sump Tank 2	5.588	0.286	4.470	0.228
Sump Tank 3	5.606	0.248	4.486	0.198
Bulk Tank	5.658	0.144	4.526	0.115
Regenerator	5.700	0.102	4.560	0.082

To simulate possible nonuniformities in the plating process that precedes the etching process, white noise was added to the plating thickness used in the "true" process, while the model assumed *PT* to be constant and equal to 36 μm (1.4 mil). The extent of this process-model mismatch in plating thickness is shown in Figure 4.3.

4.5.1 Hybrid Extended Kalman Filter

As mentioned previously, the sampling interval for ORP is 30 seconds, while the measurements of *TLW* and *BLW* are taken every 20 minutes and subject to a 5 minute lag. Techniques used for tuning the Kalman filter will be discussed in depth in a later section. Using the criteria discussed in Section 4.4.3, the system was found to be observable, as summarized in Table 4-2.

Figures 4.4*a-d* compare the actual Cu^{2+} and Cu^{+} concentrations in the first

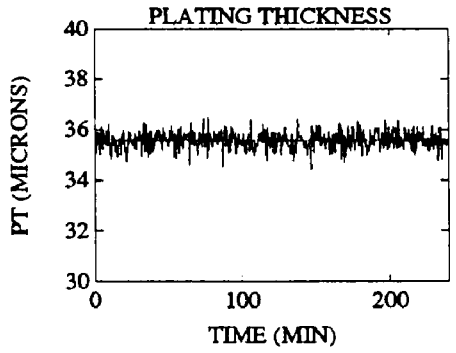

Figure 4.3: Process-Model Mismatch in Plating Thickness
Model assumes a constant 36 μm plating thickness.

Table 4-2: Tests for Observability
Hybrid Extended Kalman Filter

Observability Test Matrix Singular Values	Information Matrix Singular Values
4.53*E*–01	1.83*E*+05
2.29*E*–01	1.64*E*+05
2.28*E*–01	1.61*E*+05
2.24*E*–01	1.52*E*+05
2.73*E*–02	1.21*E*+01
3.93*E*–03	3.90*E*–01
2.21*E*–03	6.48*E*–04
6.94*E*–04	7.15*E*–06
3.54*E*–04	8.47*E*–07
1.22*E*–04	8.08*E*–09
Rank = 10	Rank = 10
Deterministically Observable	*Stochastically Observable*

sump tank and the bulk tank with the estimates of these concentrations as determined by the model alone (without measurements) and by the Kalman

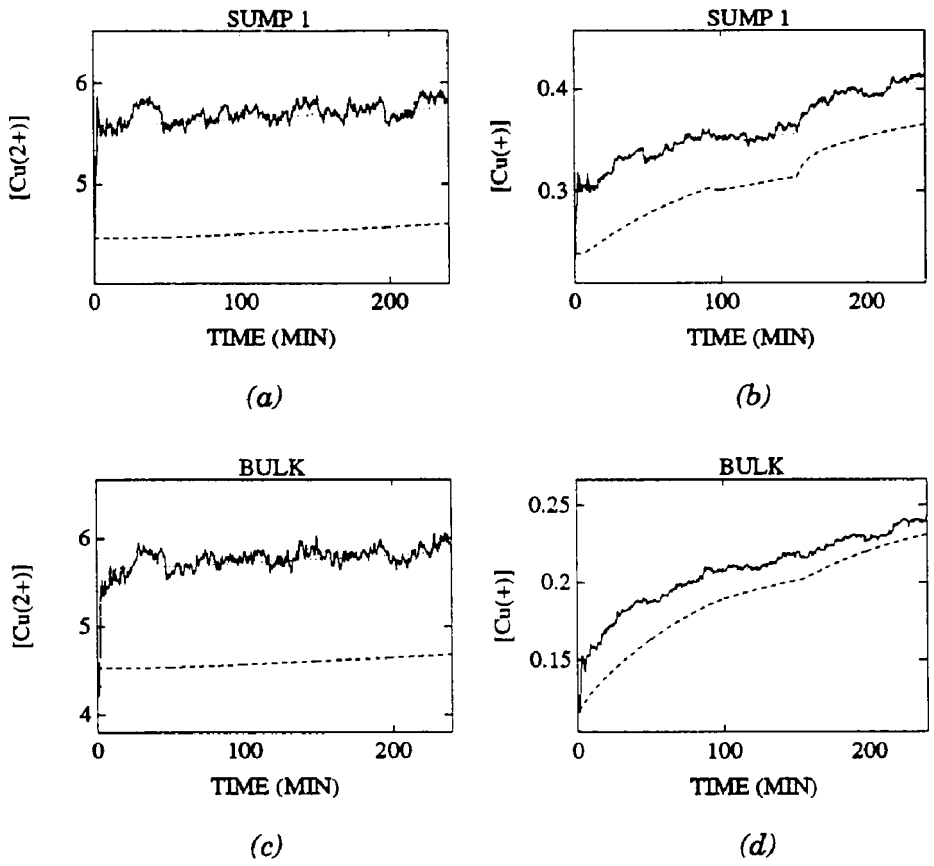

Figure 4.4: Estimation of Composition of Sump Tank 1 and Bulk Tank
Case KF1: Base Case
(· · · = true value, --- = model alone, — = KF estimate)

filter. The dotted line represents the actual values of the states, while the dashed line gives the prediction of the states strictly using the model. No measurements are used by the model to update its predictions. The state estimates from the Kalman filter, represented by the solid line, begins with the same initial values as the model. However, when given information about the measurements, the filter is able to detect the initial mismatch between the states and the state estimates and correct its estimates such that the filter converges on the true process values more quickly than the model alone

(without measurements). The predicted measurements of the ORP and line width profiles resulting from these state estimates are compared to the actual measurements in Figures 4.5*a*-*b* and 4.6*a*-*d*.

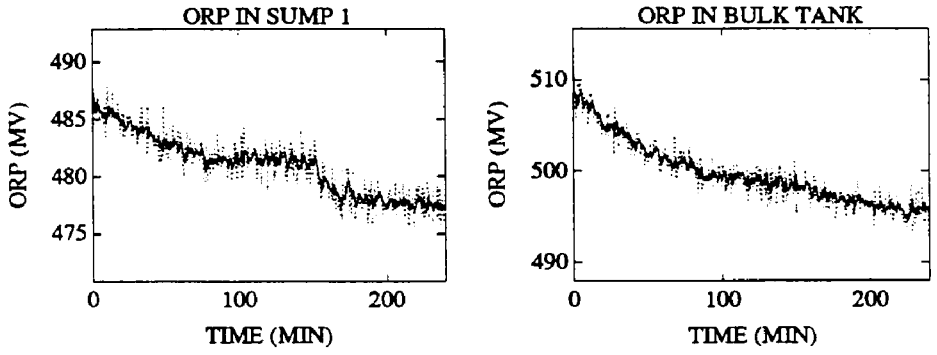

Figure 4.5: Estimation of ORP in Sump Tank 1 and Bulk Tank
(· · · = true value, --- = KF estimate)

The primary source of mismatch for this base case is the difference in the initial conditions. Because of their greater precision and stronger sensitivity to the values of the states, the extent of correction made by the filter to the state estimates is significantly larger when the infrequent etch profile measurements accompany the frequent ORP measurements than when only ORP readings are available. The filter is able to converge on the process states after two etch profile measurements, after which point the estimates remain very accurate for the remainder of the run, even in the presence of batch changes.

Quite often, accurate information about the board type will not be available. For instance, the percent masked area may be incorrect or there may be mismatch between the actual and specified mask line width. Consider the case where this additional process-model mismatch is introduced (Case KF2), as illustrated in Figures 4.7*a* and *b*. The board types used in the process will be

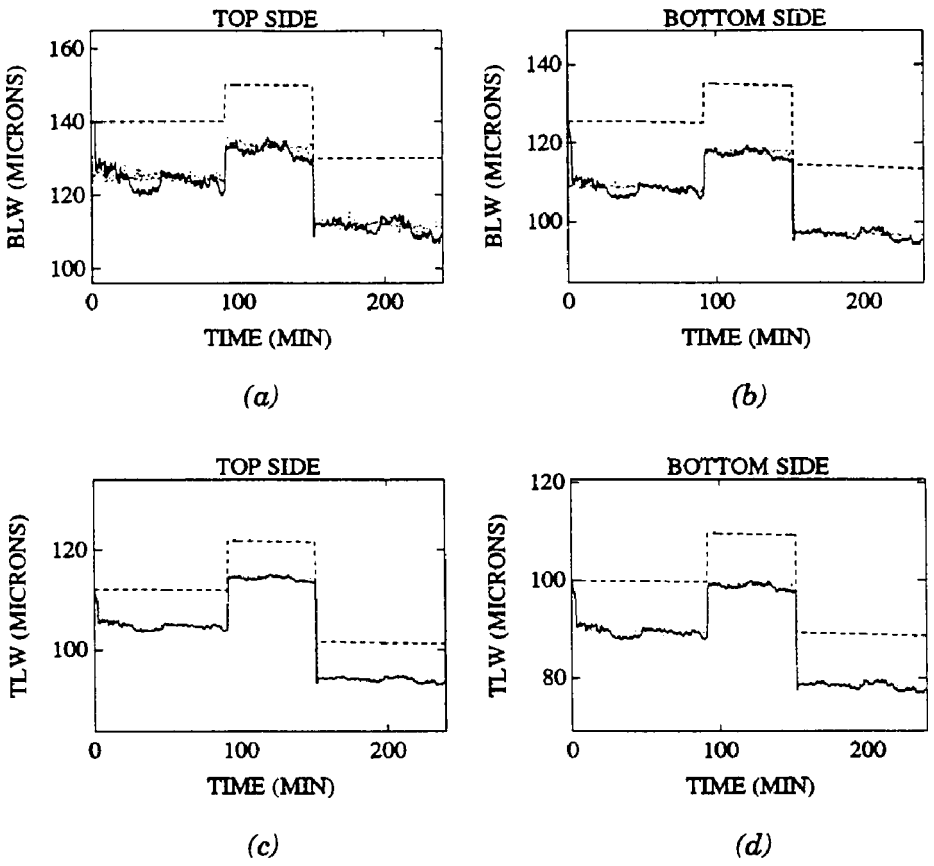

Figure 4.6: Estimation of Line Widths
Case KF1: Base Case
(· · · = true value, --- = model alone, — = KF estimate)

the same as in the base case (KF1), however the filter will assume the masked area to be constant at 15% for all three batches. In addition, the filter will be informed that the average line widths are 140, 150, and 135 μm when they are actually 140, 160, and 130 μm, respectively.

The resulting state estimates do appear to be converging, as shown in Figures 4.8*a-d*; however they are not converging on the true values of the process states. These estimates display a degree of offset, or *bias*, that is related to the amount of process-model mismatch in the board characterization. The

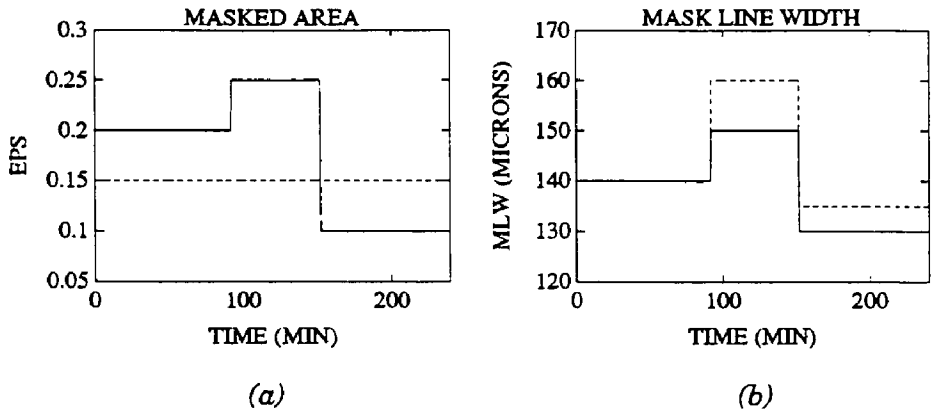

Figure 4.7: Case KF2: Process-Model Mismatch in Board Characterization
(· · · = true value, --- = model alone)

second batch (between t=90 and 150 min) has the greatest amount of mismatch associated with it (40% ε_M mismatch, 7% *MLW* mismatch) and displays the largest degree of bias. As a result of the biased state estimates, the measurement estimates are also biased (Figures 4.9*a-d*).

These results emphasize the point that I made in Section 4.4.3 with respect to the relationship between observability and filter performance. While it is a requirement that a system be observable in order to achieve good filter performance, *observability itself is not a guarantee that the estimates will be accurate*. The tests for observability can only indicate whether the model representing the process yields measurements that are sensitive to changes in the states. These tests cannot incorporate process-model mismatch into their evaluations, such as the differences in board characterization.

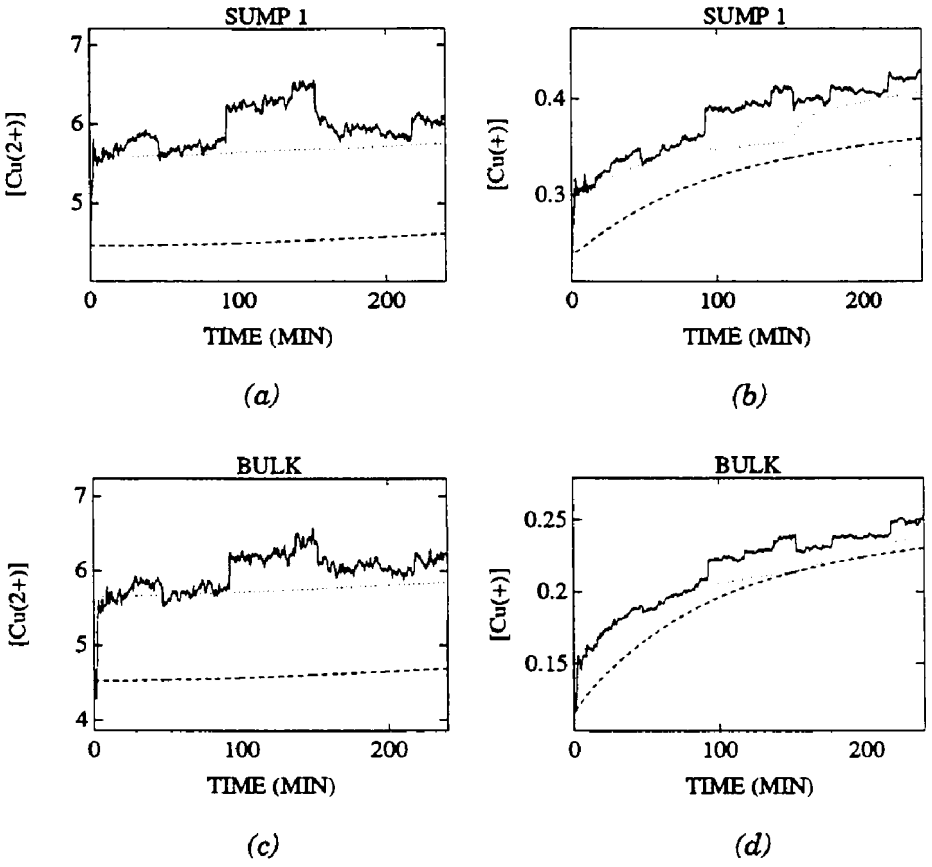

Figure 4.8: Estimation of Composition of Sump Tank 1 and Bulk Tank
Case KF2: Board Characterization Mismatch
(· · · = true value, --- = model alone, — = KF estimate)

4.5.2 Proportional-Integral Kalman Filter

In order to eliminate the bias in the state estimates resulting from excessive process-model mismatch, we can use the methodology presented in Section 4.2.4 and augment the state vector with a series of poorly known or unknown parameters. Selecting these parameters to be the percent masked area and the average mask line width, we can introduce these variables as stochastic processes. The augmented system was still found to be observable, as summarized in Table 4-3.

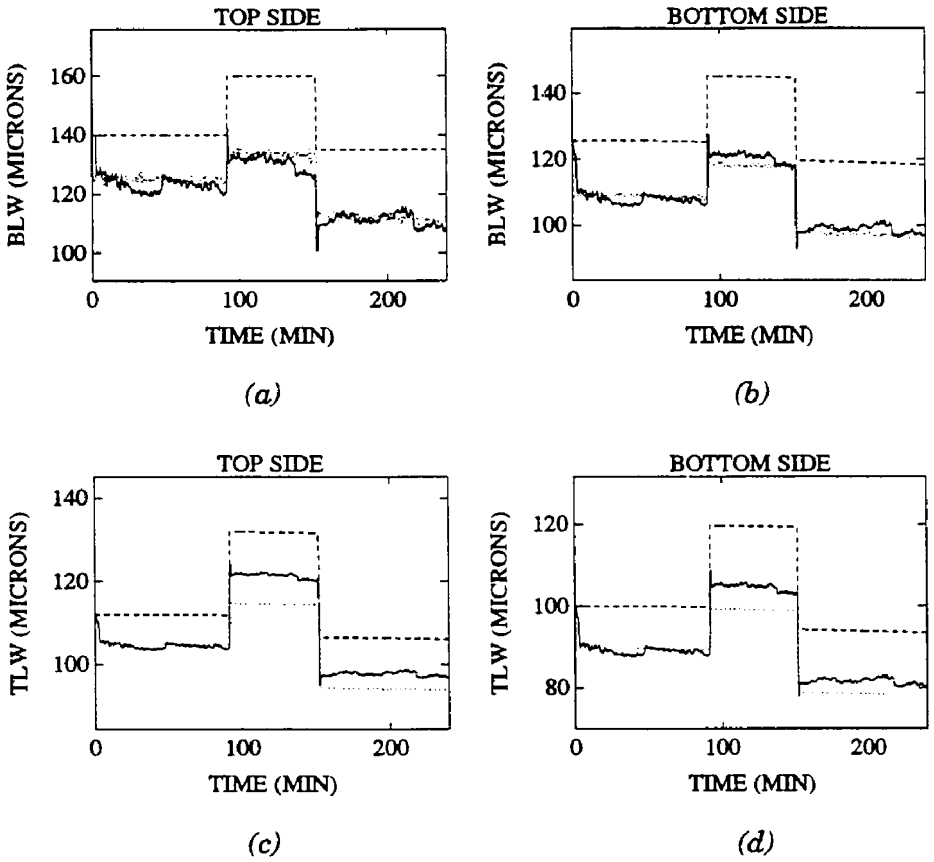

Figure 4.9: Estimation of Line Widths
Case KF2: Board Characterization Mismatch
(· · · = true value, --- = model alone, —— = KF estimate)

The task of the PI filter is to determine optimal estimates of the states, given the information that certain model parameters are poorly known and can therefore be "corrected" for the purpose of improving the state estimates. The resulting state and measurement estimates are shown in Figures 4.10 and 4.11. The corresponding estimates of the appended parameters are shown in Figures 4.12*a-b*. The PI filter has eliminated the bias in both the state and measurement estimates.

Table 4-3: Tests for Observability
Proportional-Integral Kalman Filter

Observability Test Matrix Singular Values	Information Matrix Singular Values
2.00*E*+00	1.24*E*+09
4.53*E*–01	6.99*E*+05
2.29*E*–01	1.73*E*+05
2.28*E*–01	1.70*E*+05
2.24*E*–01	1.61*E*+05
2.73*E*–02	8.39*E*+02
4.23*E*–03	4.93*E*+01
2.12*E*–03	6.60*E*+00
1.60*E*–03	1.59*E*+00
3.39*E*–04	8.73*E*–03
2.17*E*–04	8.14*E*–05
1.07*E*–04	8.38*E*–06
Rank = 12	Rank = 12
Deterministically Observable	*Stochastically Observable*

4.5.3 Filter Tuning

Tuning of the Kalman filter is accomplished through specification of the diagonal elements of the noise covariance matrices **Q** and **R**. The measurement noise covariance matrix, **R**, is specified by the precision of the measurement devices. These values may be determined from the manufacturer's specifications or through a calibration test. From either source, the variance, σ^2, can be calculated. The accuracy of the ORP meters was determined from a series of designed experiments (Covert *et al.*, 1989) to be σ=1.16 mV, while a value of σ=1.27 μm (0.05 mil) was used for the line width measurements. The values of σ^2 are used as the corresponding diagonal elements of **R**.

The initial covariance, $\mathbf{P}_0$, is an estimate of the uncertainty of the initial

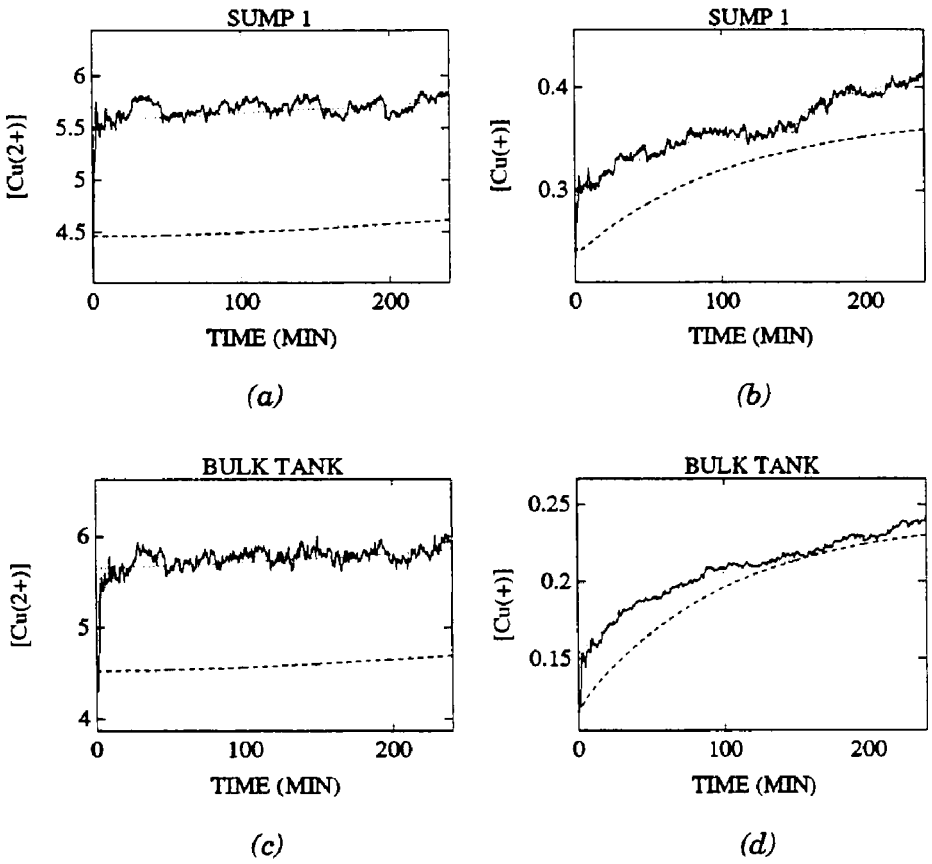

Figure 4.10: Estimation of Composition of Sump Tank 1 and Bulk Tank
Case KF3: PI Kalman Filter
(· · · = true value, --- = model alone, — = KF estimate)

values of the states. Its value affects the initial response of the filter, before a significant amount of measurements are available to aid the estimation routine. Larger initial values for **P** indicate significant uncertainty and, by corresponding to large values of the Kalman gain matrix, **K**, allows the filter to make rapid corrections to the states when measurements become available. Smaller values for $\mathbf{P}_0$ are to be used when one is fairly certain of the initial values of the states. For the results presented here, the initial uncertainty is set to be 50% of the initial state estimates, therefore the square of half the

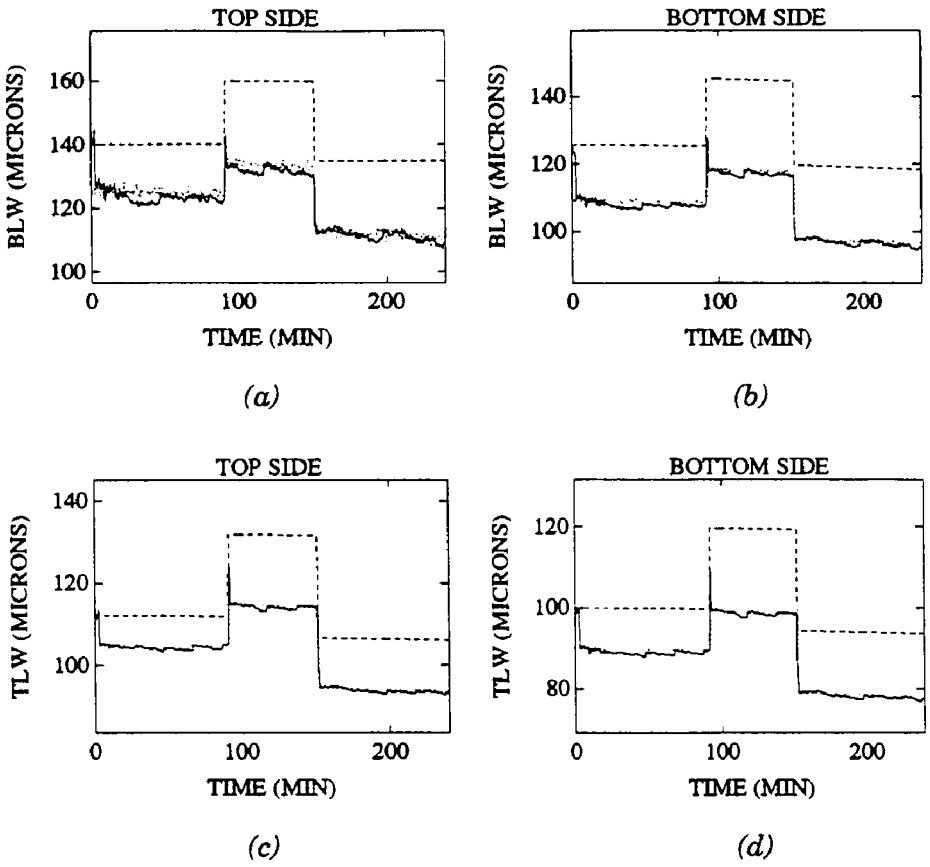

Figure 4.11: Estimation of Line Widths
Case KF3: PI Kalman Filter
(· · · = true value, --- = model alone, — = KF estimate)

initial value of each state is used as the corresponding diagonal value of $\mathbf{P}_0$.

A more significant tuning parameter than $\mathbf{P}_0$ is the process covariance matrix, $\mathbf{Q}$. The purpose of the $\mathbf{Q}$ matrix is to provide the filter with an estimate of the reliability of the model, which not only refers to process-model mismatch, but also with respect to any unmodeled disturbances. Therefore, in a stochastic environment, the diagonal elements of $\mathbf{Q}$ should *never* be set equal to zero, even if a perfect model exists. The filter would then have no freedom to alter the model to account for the effect of disturbances. The $\mathbf{Q}$ matrix diagonal elements

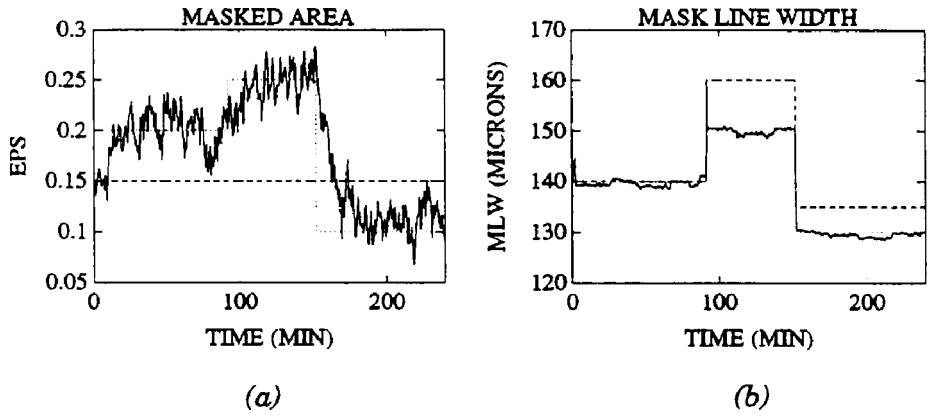

Figure 4.12: Estimation of Board Parameters
Case KF3: PI Kalman Filter
($\cdots$ = true value, --- = model alone, — = KF estimate)

should represent the expected variance (σ^2) for the probability distribution of the particular state.

Before setting the diagonal elements of $\mathbf{Q}$ equal to σ^2, first consider what is represented by this value. This is indicative of our best guess of the variance of the values the states, or the *discrete* variance, which we will represent by $\mathbf{Q}_{k-1}$. When incorporating this into the covariance propagation of the hybrid extended Kalman filter algorithm, $\mathbf{Q}$ is integrated along the sampling time interval, as shown in Equation (4.39). Therefore, it is the *continuous* variance, or $\mathbf{Q}_C$, that should be used. $\mathbf{Q}_C$ is known as the spectral density matrix for a white noise process. The relationship between the covariance matrix and the spectral density matrix depends on the system's state transition matrix, Φ: (Stengel, 1986)

$$\mathbf{Q}_{k-1} = \int_{t_{k-1}}^{t_k} \Phi(t_k,\tau)\mathbf{Q}_C(\tau)\Phi^T(t_k,\tau)\,d\tau \tag{4.91}$$

For small values of the sampling interval, $\Delta t = t_k - t_{k-1}$, the state transition matrix

approaches the identity matrix and

$$\mathbf{Q}_{k-1} \approx \mathbf{Q}_C \, \Delta t \tag{4.92}$$

Using this approximation, the integrated effect of the continuous disturbance is equal to the standard deviation. So the elements of $\mathbf{Q}_C$ are determined by,

$$diag(\mathbf{Q}_C) = \left(\frac{\sigma_1^2}{\Delta t}, \frac{\sigma_2^2}{\Delta t}, \cdots, \frac{\sigma_n^2}{\Delta t} \right) \tag{4.93}$$

and used as the corresponding diagonal elements for $\mathbf{Q}$ in Equation (4.53) as initial filter tuning parameters.

Given enough experimental data over a wide range of operating conditions for a statistical evaluation of the performance of the model, the maximum differences between the actual and predicted states can be assumed to statistically represent 99.7% of the normal distribution. Setting this uncertainty equal to 3σ, σ^2 is easily calculated (Taylor, 1982).

In the absence of such information, one can used the initial estimates of the states, $\bar{\mathbf{x}}_0$, for a preliminary tuning of $\mathbf{Q}$. Assuming the initial state estimates to be nonzero and of the correct order of magnitude of the steady state values, the standard deviation of the estimated values can be selected as a fraction of these initial values. Dividing the estimated variance by the sampling interval and defining the $\mathbf{Q}$ matrix diagonal elements, the filter is then tested with these values for a trial run. Depending on how smoothly the filter appears to be converging on values for the states, the $\mathbf{Q}$ elements are adjusted. If a particular state estimate demonstrates sluggish convergence, its corresponding variance should be increased to allow the filter greater freedom in adjusting the value of the state estimate based on the measurements. Similarly, if a

particular state estimate is extremely noisy, its variance should be decreased, placing increased confidence in the model.

Figures 4.13*a-c* show how the selection of the deviation in $[Cu^{2+}]$, σ_{A_i}, and in $[Cu^{+}]$, σ_{B_i}, which are used to calculate the elements of **Q**, affect the concentration estimates in the first sump tank, while the corresponding effects on the bottom line width predictions are given in Figures 4.14*a-c*. These plots show the performance assuming a standard deviation (σ) of 50%, 10%, and 2% of the initial state estimates. For large **Q** elements (Figures 4.13*a* and 4.14*a*), the filter has more freedom to correct the state estimates based on the measurements, which results in rapid but oscillatory response. Improvement of the estimates is obtained by decreasing the process covariance elements until no significant further improvement was noted. Figures 4.13*c* and 4.14*c*, which are the same as the results presented in Figures 4.8 and 4.9*a* and *b*, show the filter displaying relatively smooth (albeit biased) convergence.

When designing a proportional-integral Kalman filter to eliminate state estimate bias, the process covariance for the parameters used to augment the state vector must also be specified. These parameters should also be initialized to values on the same order of magnitude as the true values. If a parameter is initialized at a value that is off by, say, an order of magnitude from the actual value, the filter may try to converge on the value too rapidly and result is unacceptable oscillations and possibly unstable behavior. Again, the extent to which the filter "corrects" an individual parameter depends on the sensitivity of the states to that parameter. Improved approximations can be determined by noting in what direction the parameter in question appears to be heading and adjusting the initial guess appropriately.

When the proper range for each parameter has been determined, the process covariance associated with each parameter can be specified as a fraction

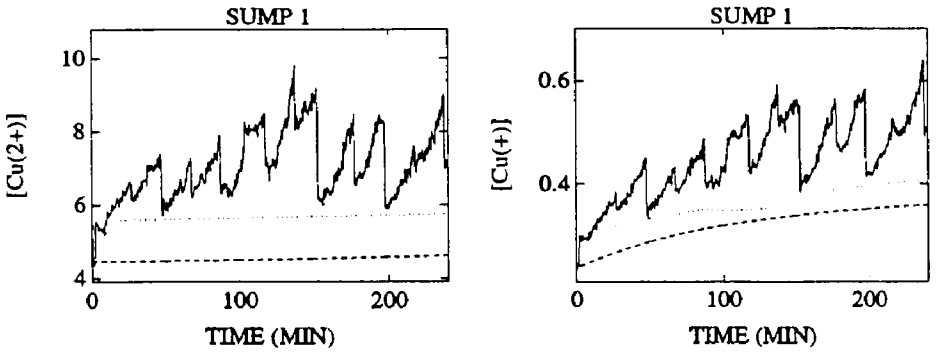

(a) $\sigma_{A_i} = 0.5A_i,\ \sigma_{B_i} = 0.5B_i$

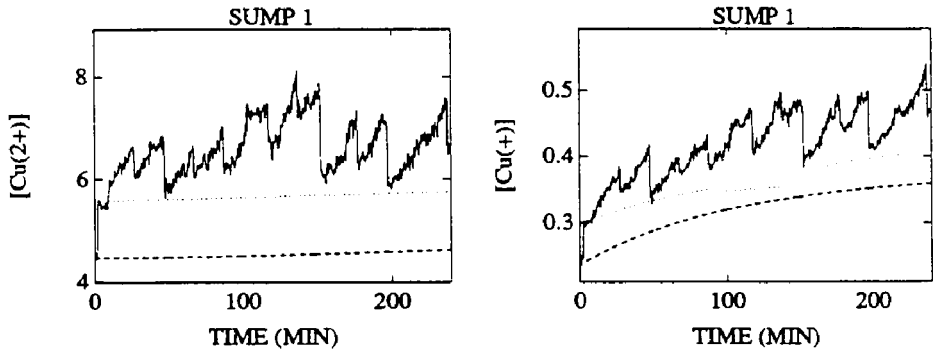

(b) $\sigma_{A_i} = 0.1A_i,\ \sigma_{B_i} = 0.1B_i$

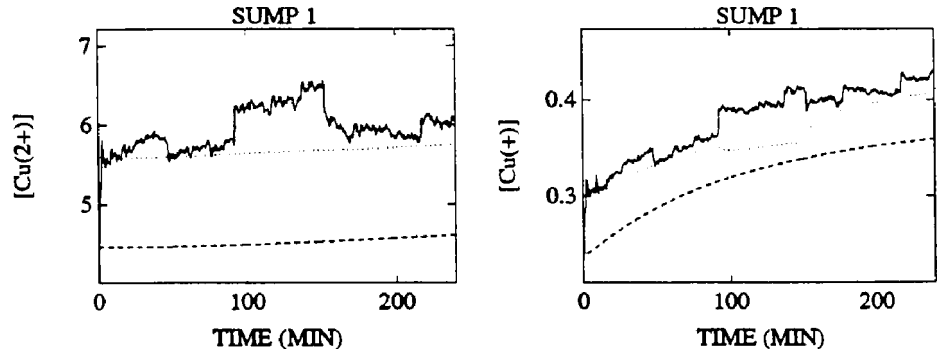

(c) $\sigma_{A_i} = 0.02A_i,\ \sigma_{B_i} = 0.02B_i$

Figure 4.13: Tuning a Hybrid Extended Kalman Filter
Effect of Q-Matrix Elements (σ_j) on State Estimates
(· · · = true value, --- = model alone, — = KF estimate)

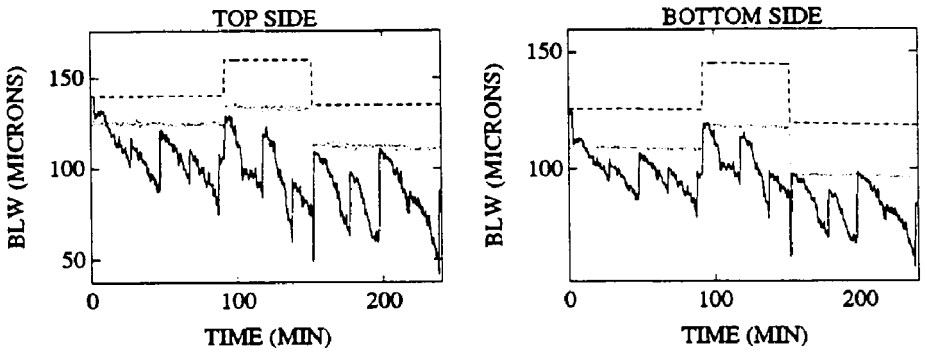

(a) $\sigma_{A_i} = 0.5A_i,\ \sigma_{B_i} = 0.5B_i$

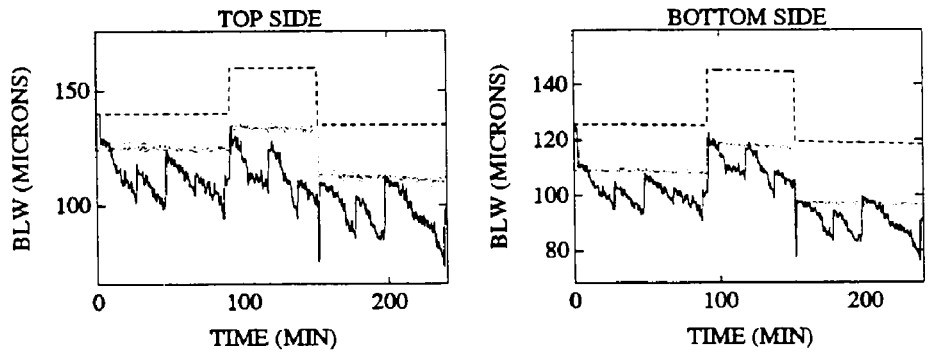

(b) $\sigma_{A_i} = 0.1A_i,\ \sigma_{B_i} = 0.1B_i$

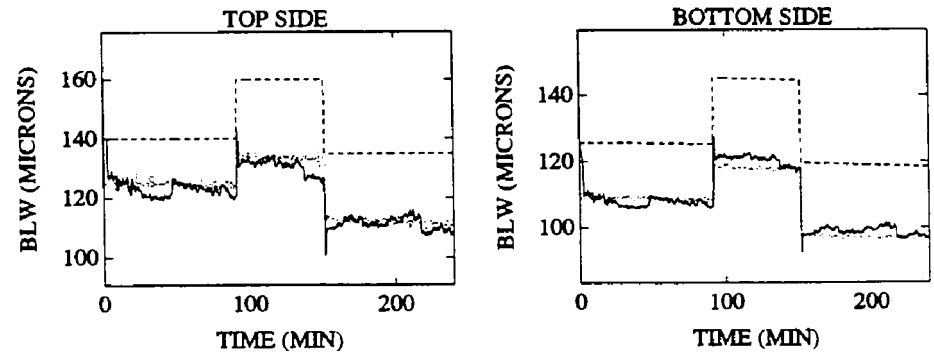

(c) $\sigma_{A_i} = 0.02A_i,\ \sigma_{B_i} = 0.02B_i$

Figure 4.14: Tuning a Hybrid Extended Kalman Filter
Effect of Q-Matrix Elements (σ_j) on Measurement Estimates
(· · · = true value, --- = model alone, — = KF estimate)

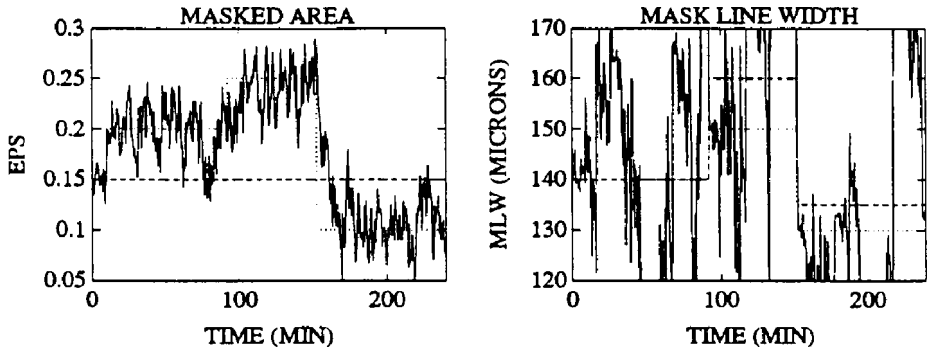

(a) $\sigma_{\varepsilon_M} = 0.5\varepsilon_M$, $\sigma_{MLW} = 0.5MLW$

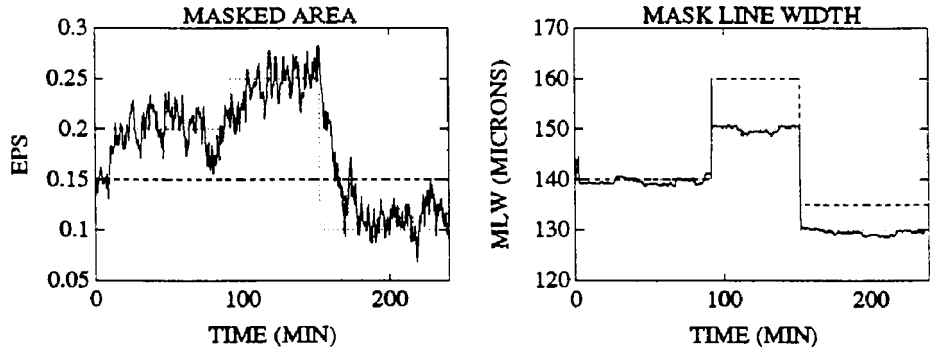

(b) $\sigma_{\varepsilon_M} = 0.3\varepsilon_M$, $\sigma_{MLW} = 0.06MLW$

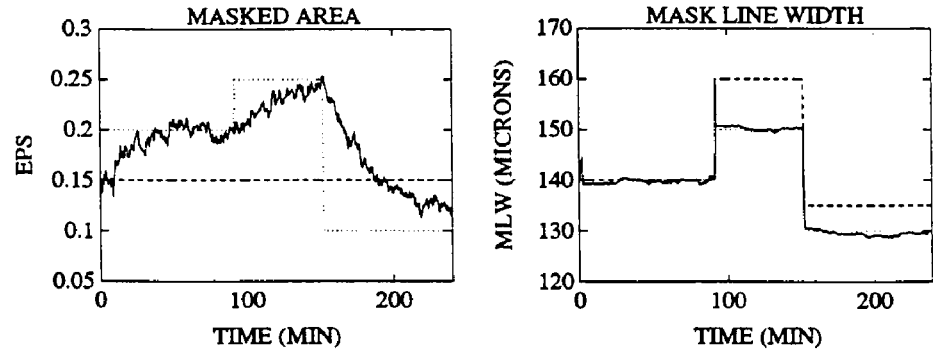

(c) $\sigma_{\varepsilon_M} = 0.04\varepsilon_M$, $\sigma_{MLW} = 0.06MLW$

Figure 4.15: Tuning a Proportional-Integral Kalman Filter
Effect of Q-Matrix Elements (σ_j) on Parameter Estimates
(· · · = true value, --- = model alone, — = KF estimate)

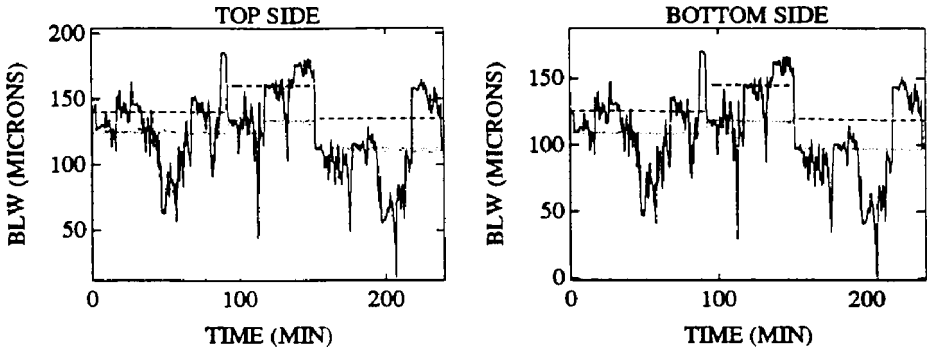

(a) $\sigma_{\varepsilon_M} = 0.5\varepsilon_M$, $\sigma_{MLW} = 0.5MLW$

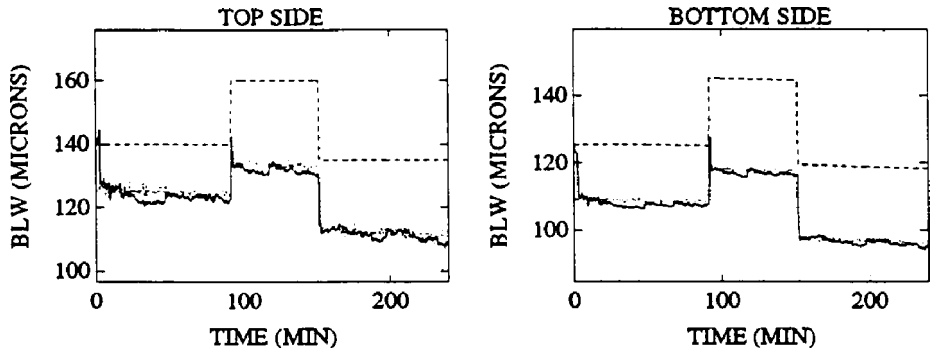

(b) $\sigma_{\varepsilon_M} = 0.3\varepsilon_M$, $\sigma_{MLW} = 0.06MLW$

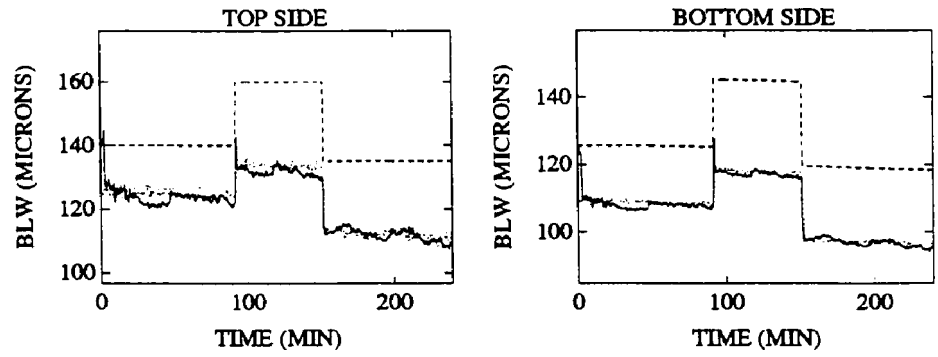

(c) $\sigma_{\varepsilon_M} = 0.04\varepsilon_M$, $\sigma_{MLW} = 0.06MLW$

Figure 4.16: Tuning a Proportional-Integral Kalman Filter
Effect of Q-Matrix Elements (σ_j) on Measurement Estimates
(· · · = true value, --- = model alone, — = KF estimate)

of the initial guess. Figures 4.15*a-c* show the effects of the deviation in masked area, σ_{ε_M}, and in mask line width, σ_{MLW}, on the parameter estimates and the associated line width estimates are shown in Figures 4.16*a-c*. The runs shown in Figures 4.15*a* and 4.16*a* used an initial estimated error of 50% of the initial parameter estimates. The result is an extremely unstable response, especially in the estimation of *MLW*. By noting the extent of the oscillatory filter output, the error can be reduced accordingly. From the plots in Figure 4.15*a*, it is apparant that the **Q** element corresponding to the estimated mask line width should be reduced by a greater extent than the estimated percent masked area. This gives an indication of the sensitivity of the state estimates to the selected parameters.

In Figures 4.15*b* and 4.16*b*, the uncertainty of the masked area is reduced to 30%, while the mask line width uncertainty is 6%. For these results, the estimation of the measurements are very good, as are the estimates of the parameters. These results coincide with those presented in Figures 4.10 and 4.11*a* and *b*.

The masked area still shows quite a bit of noise in its estimate, which is decreased by further reducing its uncertainty to 4% (Figure 4.15*c*), but at the expense of the dynamics of its estimate. The filter is now very slow to converge on the true value of this parameter, with negligible improvement of the line width measurements (Figure 4.16*c*). The reason for the insensitivity of the parameter ε_M is that its contribution to the value of the estimates of states and the measurements is not as significant as the parameter *MLW*. *MLW* has a direct effect on the line widths, while ε_M affects the system through the copper ion mass balances, which has a second order impact on the line widths.

The final tuning parameters that were used for the results presented in this chapter are summarized in Table 4-4.

Table 4-4: Kalman Filter Tuning Parameters

Process Covariance (**Q**)		Measurement Covariance (**R**)	
State/Parameter	σ^2	Measurement	σ^2
HEKF:			
$[Cu^{2+}]_{S1}$	5.54*E*–03	ORP_{S1} (V^2)	1.35*E*–06
$[Cu^{+}]_{S1}$	1.60*E*–05	ORP_{S2} (V^2)	1.35*E*–06
$[Cu^{2+}]_{S2}$	5.55*E*–03	ORP_{S3} (V^2)	1.35*E*–06
$[Cu^{+}]_{S2}$	1.44*E*–05	ORP_{B} (V^2)	1.35*E*–06
$[Cu^{2+}]_{S3}$	5.59*E*–03	BLW_{T} (cm^2)	1.61*E*–08
$[Cu^{+}]_{S3}$	1.09*E*–05	TLW_{T} (cm^2)	1.61*E*–08
$[Cu^{2+}]_{B}$	5.69*E*–03	BLW_{B} (cm^2)	1.61*E*–08
$[Cu^{+}]_{B}$	3.67*E*–06	TLW_{B} (cm^2)	1.61*E*–08
$[Cu^{2+}]_{R}$	5.78*E*–03		
$[Cu^{+}]_{R}$	1.87*E*–06		
PIKF:			
ε_M	2.50*E*–03		
MLW (cm^2)	4.36*E*–06		

4.5.4 Measurement Selection Evaluation

The observation that the extent of correction made by the filter to the state estimates when the infrequent etch profile measurements accompany the frequent ORP measurements is much greater than when only ORP readings are available (see Figures 4.4*a-d* and 4.10*a-d*) leads to the question of whether the ORP measurements are necessary.

This alternative is quickly dismissed through examination of the observability of the system using line width measurements only. As Table 4.5

Table 4-5: Tests for Observability
Hybrid Extended Kalman Filter - No ORP Measurements

Observability Test Matrix Singular Values
3.78*E*–03
1.06*E*–03
6.37*E*–05
1.72*E*–06
5.56*E*–07
2.06*E*–07
4.27*E*–21
7.54*E*–22
1.03*E*–23
0.00
Rank = 6
Deterministically Unobservable

indicates, the system is deterministically unobservable without the ORP measurements. While ORP is a less sensitive measurement than the etch profile, it is needed in order to give good estimates of the species concentrations, which are used to satisfy the mass balances.

4.5.5 Reduced Order PI Kalman Filter

An additional potential source of process-model mismatch that has not yet been addressed is with respect to the operation of the regenerator. The previous results all assume pseudo-steady state behavior in the regenerator and good knowledge of the regeneration rate constant. In order to improve its usefulness, the state estimator should also be able to compensate for regenerator process-model mismatch.

This can be accomplished by no longer estimating the concentrations of Cu^{2+} and Cu^{+} in the regenerator and treating the bulk tank concentrations as stochastic processes. This would entail the continued usage of the mass balances developed in Chapter 3.1 for the composition of the three sump tanks, but treating the bulk tank composition, which is needed to close the mass balances on the sump tanks, as augmented parameters.

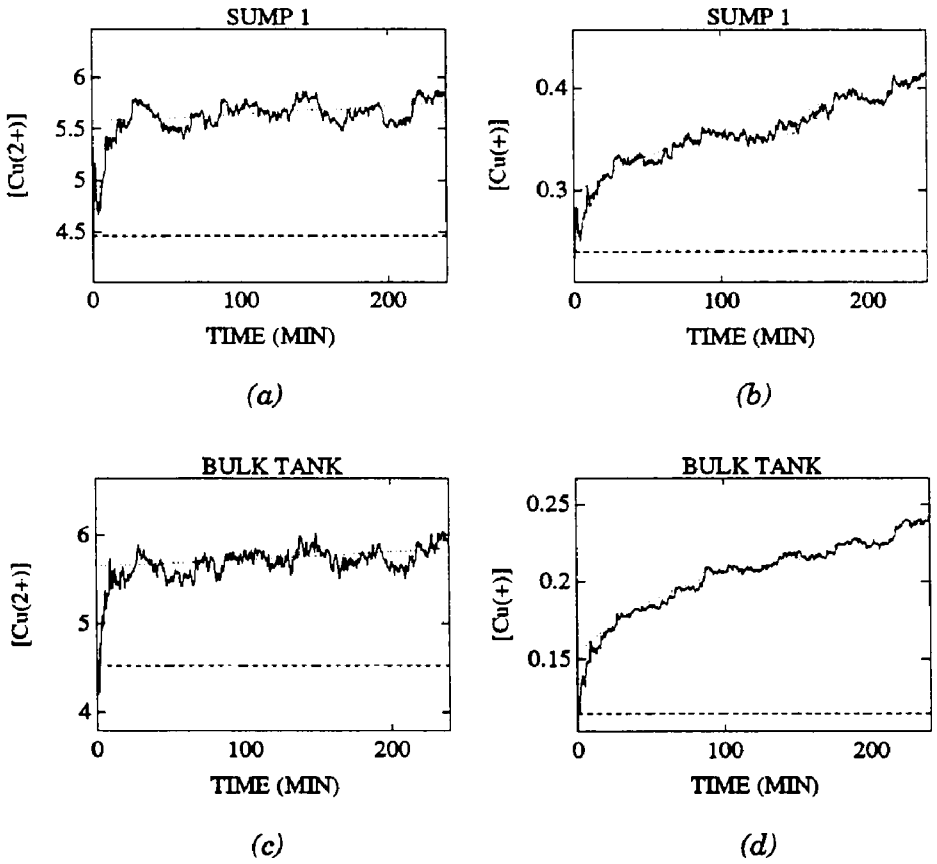

Figure 4.17: Estimation of Composition of Sump Tank 1 and Bulk Tank
Case KF4: Reduced Order PI Kalman Filter
(· · · = true value, --- = model alone, — = KF estimate)

Figures 4.17 and 4.18 show the results of estimating six states ($[Cu^{2+}]$ and $[Cu^{+}]$ in the three sump tanks) along with four parameters ($[Cu^{2+}]$ and $[Cu^{+}]$ in

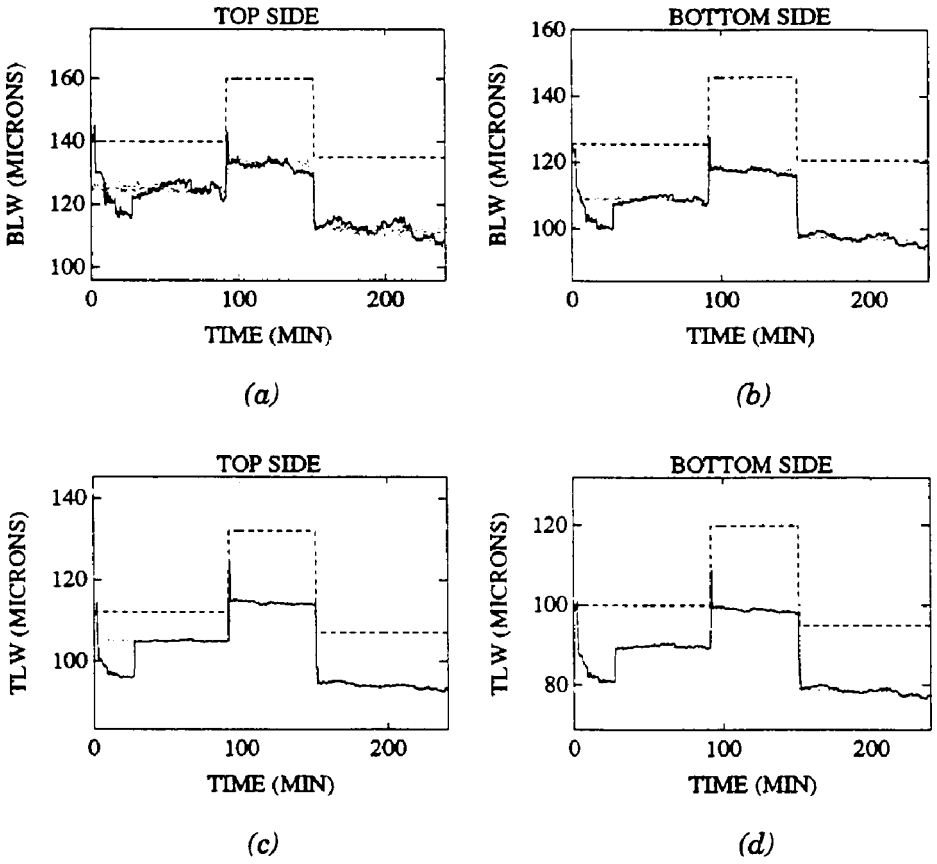

Figure 4.18: Estimation of Line Widths
Case KF4: Reduced Order PI Kalman Filter
($\cdots$ = true value, --- = model alone, — = KF estimate)

the bulk tank, ε_M, and *MLW*). The full model is still used to represent the process, however the filter no longer considers the regenerator or bulk tank dynamics for estimation purposes. Notice in the bulk tank how the model alone now assumes the composition to be constant.

The reduced order PI Kalman filter (KF4) yields estimation performance comparable to the full order PI filter (KF3). Both are able to overcome potential sources of process-model mismatch that are likely to be encountered under typical industrial conditions and eliminate the resulting bias. Having properly

designed and tuned the Kalman filter, we now have available for control purposes continuous estimates of the infrequently measured etch profiles, as well as the composition of the bulk and sump tanks. The next chapter will focus on the use of KF4 in order to manipulate the operating conditions to produce printed circuit panels with prespecified etch quality characteristics.

4.6 REFERENCES

Andrisani, D. and C. F. Gau, "Estimation Using a Multirate Filter", *IEEE Trans. Autom. Control*, **AC-32**(7), 653 (1987).

Asher, R. B., K. D. Herring, and J. C. Ryles, "Bias, Variance, and Estimation Error in Reduced Order Filters", *Automatica*, **12**, 589 (1976).

Athans, M. and E. Tse, "A Direct Derivation of the Optimal Linear Filter Using the Maximum Principle", *IEEE Trans. Autom. Control*, **AC-12**(6), 690 (1967).

Atkins, P. W., *Physical Chemistry*, 2nd ed., W. H. Freeman and Company, San Francisco (1982).

Ayres, Frank, *Theory and Problems of Matrices*, McGraw-Hill, New York (1962).

Barham, P. M. and D. E. Humphries, "Derivation of the Kalman Filtering Equations from Elementary Statistical Principles", In *Theory and Applications of Kalman Filtering*, C. T. Leondes (Ed.), NATO Advisory Group for Aerospace Research and Development, AGARDograph No. 139, University of California, Los Angeles (1970).

Battin, R. H. and G. M. Levine, "Application of Kalman Filtering Techniques to the Apollo Program", In *Theory and Applications of Kalman Filtering*, C. T. Leondes (Ed.), NATO Advisory Group for Aerospace Research and Development, AGARDograph No. 139, University of California, Los Angeles (1970).

Carroll, T. A. and W. F. Ramirez, "On-Line State and Parameter Identification of Positive Photoresist Development", *AIChE J.*, **36**(7), 1046 (1990).

Chattaway, T. and G. Stephanopoulos, "Adaptive Estimation of Bioreactors: Monitoring Plasmid Instability", *Chem. Eng. Sci.*, **44**(1), 41 (1989).

Covert, K. L., D. N. Light, and R. W. Keesler, "Etch Rate of Copper in Acidic Cupric Chloride: A Designed Experiment", IBM Technical Report TR 01.B275 (1989).

Dimitratos, J., C. Georgakis, M. S. El-Aasser, and A. Klein, "Dynamic Modeling and State Estimation for an Emulsion Copolymerization Reactor", *Computers Chem. Engng.*, **13**(1/2), 21 (1989).

Fitzgerald, R. J., "Divergence of the Kalman Filter", *IEEE Trans. Autom. Control*, **AC-16**(6), 736 (1971).

Friedland, B., *Control System Design: An Introduction to State-Space Methods*, McGraw-Hill, New York (1986).

Gelb, A., J. F. Kasper, R. A. Nash, C. F. Price, and A. A. Sutherland, *Applied Optimal Estimation*, MIT Press, Cambirdge, MA (1974).

Jazwinski, A. H., *Stochastic Process and Filtering Theory*, Academic Press, London" (1970).

Kalman, R. E., "A New Approach to Linear Filtering and Prediction Problems", *Trans. ASME, J. Basic Engrg.*, **82**, 35 (1960).

Kalman, R. E. and R. S. Bucy, "New Results in Linear Filtering and Predictions Theory", *Trans. ASME, J. Basic Engrg.*, **83**, 95 (1961).

King, R. and E. D. Gilles, "Multiple Filter Methods for Detection of Hazardous States in an Industrial Plant", *AIChE J.*, **36**(11), 1697 (1990).

Kiparissides, C., J. F. MacGregor, and A. E. Hamielec, "Suboptimal Stochastic Control of a Continuous Latex Reactor", *AIChE J.*, **27**(1), 13 (1981).

Kolmogorov, A. N., "Interpolation and Extrapolation of Stationary Random Sequences", *Bull. Acad. Sci., USSR, Math. Ser.*, **5**, 3 (1941).

Laub, A. J., "Numerical Linear Algebra Aspects of Control Design Computations", *IEEE Trans. Autom. Control*, **AC-30**(2), 97 (1985).

Lennartson, B. E. V., "Combining Infrequent and Indirect Measurements by Estimation and Control", *Ind. Eng. Chem. Res.*, **28**(11), 1653 (1989).

Luyben, W. L., *Process Modeling, Simulation and Control for Chemical Engineers*, 2nd ed., McGraw-Hill, New York (1990).

MacGregor, J. F., D. J. Kozub, A. Penlidis, and A. E. Hamielec, "State Estimation for Polymerization Reactors", In *IFAC Symp. On Dynamics and Control of Chemical Reactors and Distillation Columns*, Pergamon Press(1986).

Ramirez, W. F., "Optimal State and Parameter Identification - An Application to Batch Fermentation", *Chem. Eng. Sci.*, **42**, 2749 (1987).

Rhodes, I. B., "A Tutorial Introduction to Estimation and Filtering", *IEEE Trans. Autom. Control*, **AC-16**(6), 688 (1971).

Rutan, S. C. and S. D. Brown, "Adaptive Kalman Filtering Used to Compensate for Model Errors in Multicomponent Analysis", *Anal. Chim. Acta*, **160**, 99 (1984).

Schlee, F. H., C. J. Standish, and N. F. Toda, "Divergence in the Kalman Filter", *AIAA J.*, **5**(6), 1114 (1967).

Seinfeld, J. H., "Optimal Stochastic Control of Nonlinear Systems", *AIChE J.*, **16**(6), 1016 (1970).

Stengel, R. F., *Stochastic Optimal Control*, John Wiley & Sons, New York (1986).

Takahashi, Y., M. J. Rabins, and D. M. Auslander, *Control and Dynamic Systems*, Addison-Wesley, Reading, MA (1972).

Taylor, J. R., *An Introduction to Error Analysis*, University Science Books, Mill Valley, CA (1982).

Vakil, H. B., M. L. Michelsen, and A. S. Foss, "Fixed-Bed Reactor Control with State Estimation", *Ind. Eng. Chem. Fundam.*, **12**(3), 328 (1973).

Wells, C. H., "Application of Modern Estimation and Identification Techniques to Chemical Processes", *AIChE J.*, **17**(4), 966 (1971).

Wiener, N., *The Extrapolation, Interpolation, and Smoothing of Stationary Time Series*, John Wiley & Sons, New York (1949).

CHAPTER

FIVE

CONTROL STRATEGY

5.1 CONTROL OBJECTIVES

In the past, spray etching lines have been run according to very subjective and empirical rules. Productivity depended greatly on the operators working on the etch line, with the best production yields usually coming from those operators with the most experience. Boards are examined as they come off the etch line and, based on a visual inspection, changes in the operating conditions (such as the conveyor speed or the spray pressures) are made if necessary. What sets the more experienced operators apart from the newer people is the ability to draw from past experiences and stronger intuitions when making control decisions.

This form of "process control" has been adequate in the past, however it is very susceptible to human error. It will not be satisfactory for production trends of the future. With the personal computers having made such tremendous strides since first being introduced ten years ago and the increasingly widespread usage of workstations and supercomputers, further improvement seems to be limited by only the ability to physically produce increasingly

sophisticated circuit patterns. To properly respond to the desire to perform fine line etching with the existing equipment, we must turn to more sophisticated means of controlling the process.

The conventional method of automated process control is illustrated in Figure 5.1*a*. For any given process, which is a function of its states, system inputs, and outside disturbances, we wish to manipulate the inputs in a manner that results in desired values of the states. In general, these states will not be directly available for measurement. The measurements that are available are functions of the states, but subject to measurement noise. The controller uses a comparison of the actual measurements to the desired setpoint of the measurements and adjusts the inputs accordingly.

When will this methodology not be sufficient? The type of control system implemented on a system depends on the control objectives. If the controlled variables are the same as the measured variables and the measurements are available at a frequent rate, then the conventional method shown in Figure 5.1*a* will suffice. However, if one seeks to control the states that are not measured directly, or if the variables to be controlled are not measured at a frequent rate, the standard techniques must be modified.

For the spray etching processes that we wish to control, the available measurements are ORP (frequent) and etch profile (infrequent). Since the ORP measurements are available at a frequent rate, can the process be controlled by maintaining constant ORP? Figure 5.2 shows the dependency of ORP on the ratio of cupric/cuprous ions, as given by the Nernst equation. From this plot, it can be observed that in the operating range of interest (where acceptable etch rates are possible), the ORP is relatively insensitive to changes in composition. A change in $[Cu^{2+}]/[Cu^{+}]$ from 20 to 50 results in only an 8% change in ORP. Coupled with the noise and drift associated with ORP meters, it is apparant

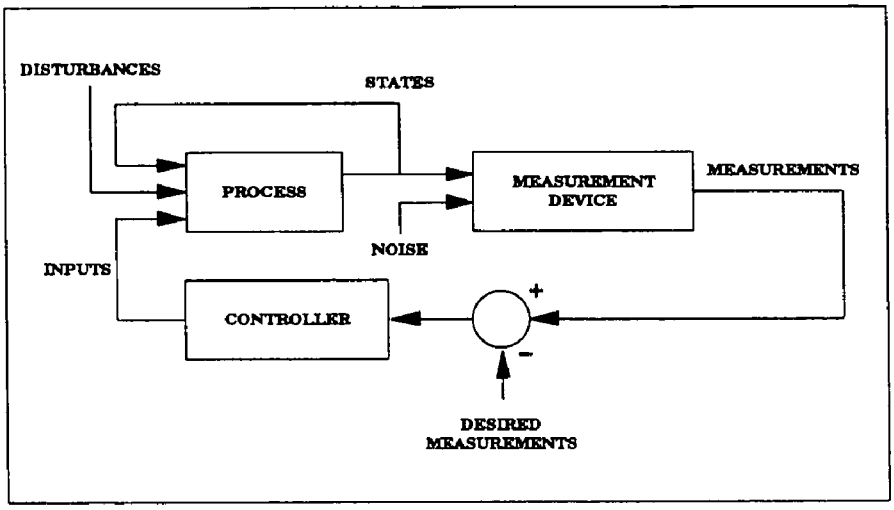

(a) Conventional Process Control

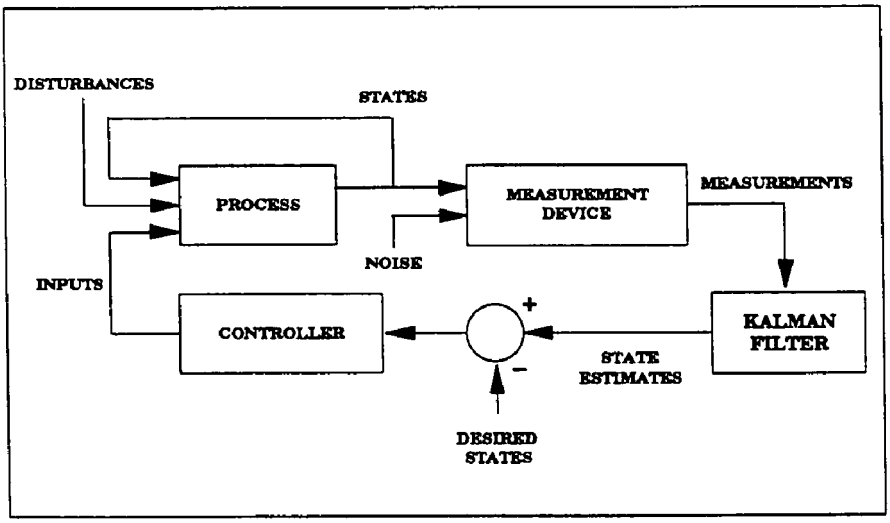

(b) State Estimation and Control

Figure 5.1: Comparison of Control Methodologies

that maintaining constant ORP in this operating range will not guarantee constant etch performance.

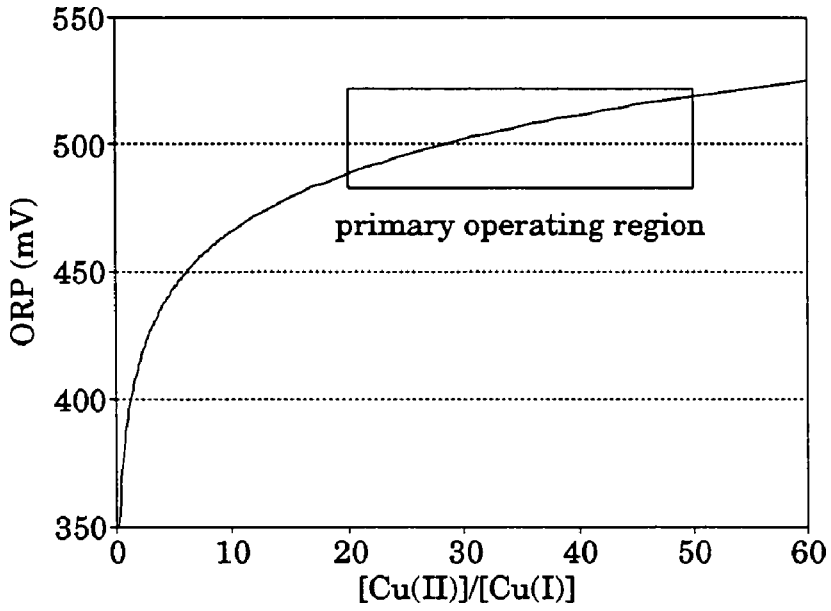

Figure 5.2: Sensitivity of ORP to Concentration Changes

By shifting the operating range to regions where ORP readings are more sensitive, etch rates will be severely reduced because of the decreased concentration of the etching species, Cu^{2+}, and the possible etch inhibition caused by increasing concentrations of Cu^{+}. Therefore etch productivity will be negatively affected by this option.

Another option is to design a sampled-data control system that takes periodic control actions when line width measurements are available. A typical sampling interval for line width measurements is once every 20 minutes (plus a 5 minute lag) and control actions can be taken at the most once every sampling interval. Open loop step response tests of the line widths revealed almost

instantaneous responses to step changes in the manipulated variables. The system was treated as a first order process with an open loop time constant equivalent to the residence time in the reactor system. The 20-minute sampling period is considerably longer than the open loop time constant. Therefore a conventional sampled-data control system will not suffice, since the sampling period must be smaller than the process time constant for acceptable controller performance (Luyben, 1990).

An alternative is to enhance the control system with a state estimation scheme, as illustrated in Figure 5.1*b*. In this scenario, the available measurements are processed (using a Kalman filter) to generate estimates of the unmeasured states. These can then be compared to desired values of the states and the appropriate control actions can be taken. Since the state estimates are determined by estimating the measurements and comparing these with the actual measurements, this scheme can also be used when measurements of the variables of interest *are* available, but not at a frequent enough rate for use with a controller.

Kalman filters are not necessarily the only type of state estimator available for use in this methodology. Other state estimation methods such as observers (Luenberger, 1971), recursive least squares (Astrom and Wittenmark, 1989), or Bayesian estimators (Ho and Lee, 1964) can also be used. However, in a stochastic environment, where states are subject to temporal and spatial variability, and when measurement noise, process disturbances, and modeling errors are taken into consideration, the Kalman filter has been shown to be the "best" (minimum error variance) state estimator (Maybeck, 1979).

5.2 CONTROL LOOP INTERACTION

The simplest way to design a multivariable control system is to treat the process as if it were a collection of isolated single variable processes. However, the resulting control loops often involve the same state variables, in which case a certain degree of interaction will exist between the loops. Control actions taken by one loop may have undesirable effects on a different loop, causing the individual controllers to "fight with each other", as each controller attempts to accomplish its own control objective.

A simple method of determining the extent of control loop interaction is a steady-state technique known as the *relative gain array* (Bristol, 1966). By analyzing the steady state model of a system, the effects of the control actions, denoted by the vector **u**, on the output variables, **y**, can be used to determine a steady state gain matrix. These variables are related to each other by the state variables, **x**. The dynamic system in state space form is:

$$\dot{\mathbf{x}} = \mathbf{Ax} + \mathbf{Bu} \tag{5.1}$$

$$\mathbf{y} = \mathbf{Cx} \tag{5.2}$$

At steady state, combining these equations gives,

$$\mathbf{y} = -\mathbf{CA}^{-1}\mathbf{Bu} = \mathbf{G(0)u} \tag{5.3}$$

where $\mathbf{G(0)}=-\mathbf{CA}^{-1}\mathbf{B}$ is the steady state gain matrix.

From Equation (5.3), we can calculate the relative gain, λ. The relative gain is a measure of the influence that one particular manipulated variable has over a controlled variable relative to that of other manipulated variables in the process. If a manipulated variable affects more than one control variable, the response of a particular control variable to changes in one manipulated variable

will depend on what the other manipulated variables are doing. To measure this interaction, the open loop gain of the loop in question should be evaluated first with all other loops open (constant manipulated variables). This gain should then be compared to the open loop gain reevaluated with all other loops closed (constant control variables). If there is little difference between these two gains, the effects of the other loops are negligible and the loop in question can be considered an isolated SISO control loop.

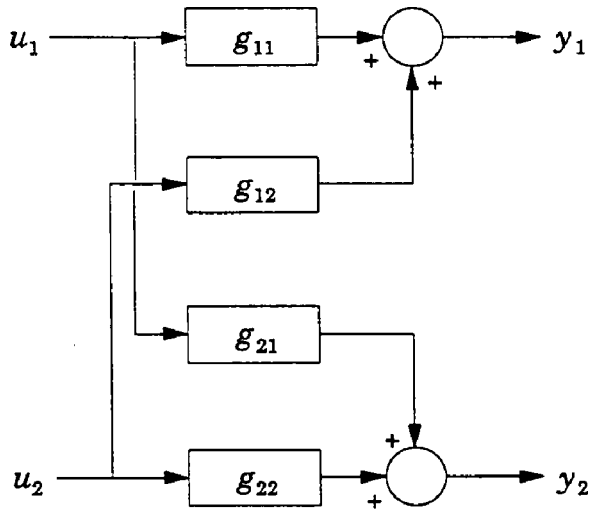

Figure 5.3: Control Loop Interaction for a 2 × 2 system
g_{ij} refer to elements of steady state gain matrix, **G(0)**

For a two-input, two-output system, such as the spray etching process, the interaction between control loops is illustrated in Figure 5.3. The relative gain, λ, can be written as:

$$\lambda = \frac{g_{11}}{g_{11} - g_{12}g_{22}^{-1}g_{21}} \tag{5.4}$$

As defined in Equation (5.4), λ is the interaction measure for the control

structure where y_1 is controlled by u_1 and y_2 is controlled by u_2 ($u_1 \rightarrow y_1, u_2 \rightarrow y_2$). The interaction measure is the ratio of the open loop gain between y_1 and u_1 when the second loop is open (u_2=0) over the open loop gain between y_1 and u_1 when the other loop is closed and perfect (y_2=0). A value of λ close to unity indicates no substantial steady state interaction between the $u_1 \rightarrow y_1$ loop and the $u_2 \rightarrow y_2$ loop, thus allowing the use of SISO controllers for the process. If λ is close to zero, there will still be little interaction between control loops, provided that a ($u_1 \rightarrow y_2, u_2 \rightarrow y_1$) control structure is used. The most difficult cases to control are when $\lambda \approx 0.5$ or when $\lambda \gg 1$.

The controllers for the spray etching system will control the line width on the top side of the boards by manipulating the conveyor speed, while the bottom spray pressure will be used to maintain the bottom side line widths at a desired value. Changes in the conveyor speed will affect the residence time of the boards in the etch chambers, thus both top and bottom side line widths are affected. The bottom spray pressure only affects the bottom side of the boards; therefore, g_{12} from Figure 5.3 is equal to zero and the relative gain, according to Equation (5.4), is unity. Thus, the two control loops can be designed and tuned separately.

5.3 RESULTS AND DISCUSSION

The same scenario that was used for the open loop state estimation in Chapter 4 will be used to test the controllers. Two PI controllers were designed to control the bottom line width on the top and bottom sides of the panels using the conveyor speed and bottom spray pressure, respectively, as the manipulated variables. The top spray pressure is maintained at a maximum value, selected here to be 30 psi. As the open loop results from Case KF4 showed, the average

bottom line widths for the three batches were 125, 134, and 112 μm on the top side and 109, 118, and 97 μm on the bottom side. The control objective for the results presented is to maintain the line width on both sides at 100 μm.

The open loop gain was found from the step responses. The closed loop time constant was chosen to be half the open loop time constant and a damping coefficient of 0.7 was selected for the design of both control loops. From the open loop transfer function, the tuning parameters were determined from the characteristic equation (Luyben, 1990). The final tuning parameters are given in Table 5-1.

Table 5-1: Summary of Controller Tuning Parameters

Controlled Variable	Manipulated Variable	Gain	Reset Time
BLW_T	u_{con}	4000 (cm/min)/cm	1.28 min^{-1}
BLW_B	BSP	-2500 psi/cm	1.09 min^{-1}

The filter was initialized with the same initial conditions that was used for the open loop scenarios from Chapter 4, which are different than the actual process values. The filter was then allowed to converge on the process states before the control system began to consider the line width measurements from the filter for control decisions.

The controlled line widths are shown in Figures 5.4*a* and *b*. The corresponding controller actions are shown in Figures 5.5*a* and *b*. The peaks between batches are caused by the boards that are in the etch line at the time of the significant controller changes. These can be avoided in practice by waiting until all of the boards from one batch have left the etch line before starting the

next batch. The average top and bottom side line widths, excluding the two transition peaks between batches, are 99.9 and 99.7 μm with standard deviations of 2.1 and 1.6 μm, respectively.

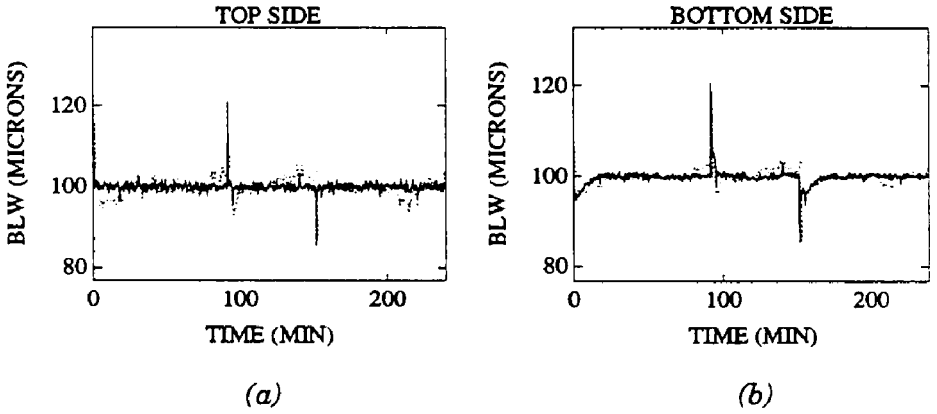

Figure 5.4: Controlled Bottom Line Widths Using KF Estimates
Setpoint = 100 μm
(· · · = true value, — = KF estimate)

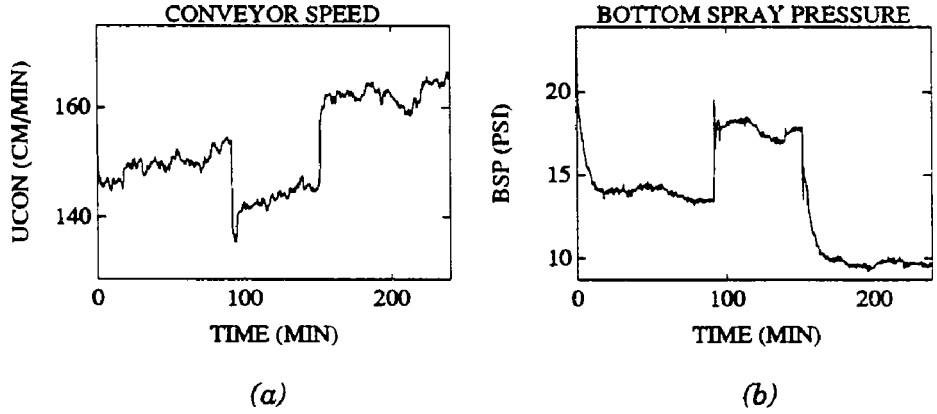

Figure 5.5: Controller Actions, Based on KF Estimates

For a comparison, a parallel case was run for the ideal case, where instrumentation is available for making frequent and accurate line width measurements at the end of the etch line. If the accuracy of these meters is

sufficient, this eliminates the need for off-line etch profile inspections. The results of using the designed control loops on this configuration are shown in Figures 5.6 and 5.7. The uncertainty of the optical line width measurements is ± 1.27 μm. The results are comparable with those obtained using the Kalman filter for state estimation.

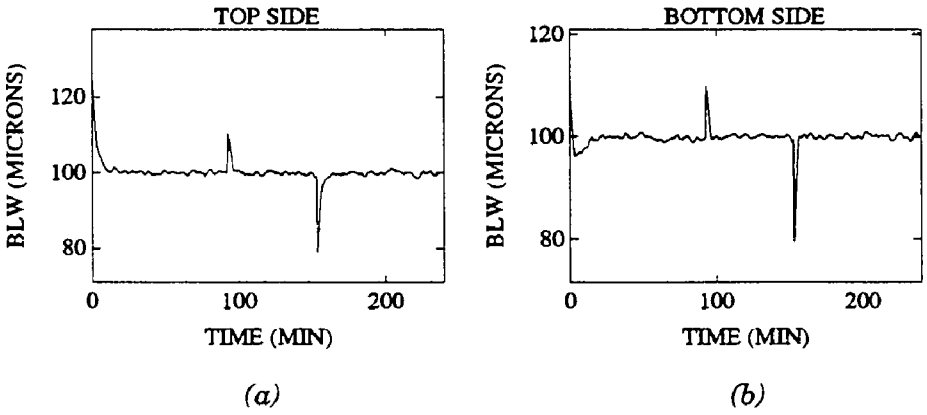

Figure 5.6: Controlled Line Widths Using Conventional Controllers
Frequent Line Width Measurements Available
Setpoint = 100 μm

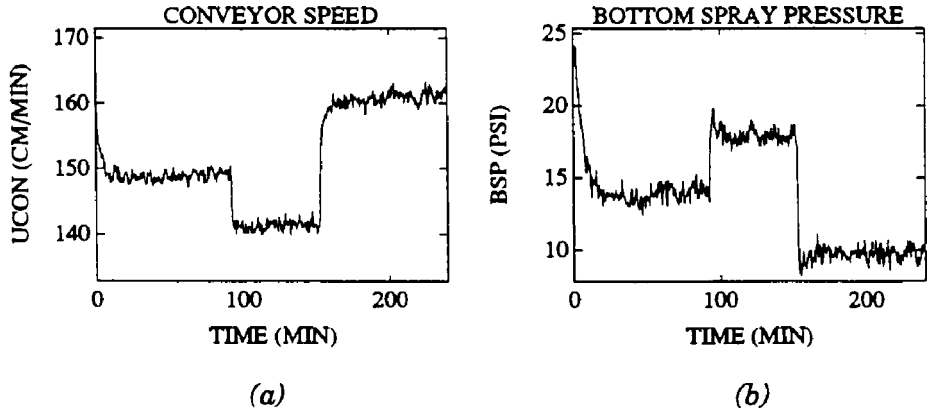

Figure 5.7: Controller Actions, Based on Frequent *BLW* Measurements

5.4 EXTENSIONS TO OTHER PROCESSES

The focus of this thesis is the application of state estimation and control techniques toward improved operation of spray etching processes. However, the main idea is not limited to this process. Any process that has the same difficulties of either trying to control states that are not measured or maintaining variables that are measured but at an infrequent rate can take advantage of the methodology presented here.

A general procedure is outlined below for designing a state estimation and control system for an electronic materials manufacturing process that involves the control of local properties that are not easily measured. This procedure can be summarized in the following steps:

1. ***Develop Global Process Model***
   This involves identifying all of the unit operations that are associated with the process (mixed tanks, absorption columns, etc.) and developing overall mass balances for the species of interest. Most unit operations are well understood, so the components of the global model will often be available in the literature or a variety of textbooks (Geankoplis, 1983, McCabe *et al.*, 1985).
2. ***Develop Local Reaction Model***
   This step will be the most dependent on the system. To be considered are the effects of mass transfer and chemical kinetics. Several experiments may be required to determine the extent of each of these contributions to the overall surface reaction.
3. ***Design Proportional-Integral Kalman Filter***
   The design of the state estimation scheme consists of two parts. First, the available measurements must be identified and the observability of the system checked. If the system is found to be unobservable, then more sensitive or additional measurments must be added before a successful control system can be designed. After the measurements have been identified, a hybrid extended Kalman filter can be developed. To eliminate estimate bias, the filter should be augmented with any poorly known parameters, such as uncertain parameters from the local reaction model. The resulting filter can then be tuned following the guidelines outlined in Chapter 4.5.3.
4. ***Design Control Loops***
   Once accurate estimates of the controlled variables are available

from the Kalman filter and the manipulated variables have been identified, the controllers can be designed. Controller design and tuning techniques are discussed extensively in a number of textbooks (Luyben, 1990, Stephanopoulos, 1984). For multivariable systems, first check the control loop interaction. If there is significant interaction, multivariable control techniques may be required.

5.5 REFERENCES

Astrom, K. J. and B. Wittenmark, *Adaptive Control*, Addison-Wesley, Reading, MA (1989).

Bristol, E. H., "On A New Measure of Interaction for Multivariable Process Control", *IEEE Trans. Autom. Control*, **AC-11**, 133 (1966).

Geankoplis, C. J., *Transport Processes and Unit Operations*, 2nd ed., Allyn and Bacon, Boston (1983).

Ho, Y. C. and R. C. K. Lee, "A Bayesian Approach to Problems in Stochastic Estimation and Control", *IEEE Trans. Autom. Control*, **AC-9**, 333 (1964).

Luenberger, D. G., "An Introduction to Observers", *IEEE Trans. Autom. Control*, **AC-16**(6), 596 (1971).

Luyben, W. L., *Process Modeling, Simulation and Control for Chemical Engineers*, 2nd ed., McGraw-Hill, New York (1990).

Maybeck, P. S., *Stochastic Models, Estimation, and Control: Volume 1*, Academic Press, New York (1979).

McCabe, W. L., J. C. Smith, and P. Harriott, *Unit Operations of Chemical Engineering*, 4th ed., McGraw Hill, New York (1985).

Stephanopoulos, G., *Chemical Process Control: An Introduction to Theory and Practice*, Prentice-Hall, Englewood Cliffs, NJ (1984).

This is a blank page

CHAPTER

SIX

CONCLUSIONS AND RECOMMENDATIONS

The goal of this work was to develop a better understanding of the fundamentals behind the operation of spray etching processes. Based on this investigation, we sought to develop an improved means of controlling the process such that the increasing demands for fine line etching with tighter geometric tolerances could be met.

The investigation of the fundamentals behind the process revealed several interesting phenomena that explain some of the difficulties encountered during operation. Higher spray pressures are required for the top sides than for the bottom sides in order to achieve equal amounts of etching on each side of the boards being processed. This is due to additional mass transfer limitations that are created when puddles of liquid collect on the top side of the boards.

Another phenomenon that was examined was the ability to produce lines with vertical walls. Nonvertical etch profiles are typical of wet etching processes because the top of the line is in contact with the etching solution for a longer period than the bottom, thus the top line width is generally smaller than the bottom line width. However, we found experimentally that the etch angle increases as the extent of etch undercut increases. This is due to the formation

of weak recirculating eddies underneath the mask, which inhibit mass transport at the top of the line and allow the bottom line width to "catch up" with the top line width. Therefore, vertical lines can be achieved (by overdesigning the mask line widths), but at the expense of line spacing. This tradeoff must be considered when designing a mask for a circuit design.

The local modeling effort for this process was limited by the lack of available equipment for performing a wide range of experiments. The model presented was the best possible, given the limited amount of experimental data collected. A worthwhile extension of this research would be to perform a more detailed analysis of the local phenomena occurring at the board surface. This would make possible a more rigorous representation of the relationship between the mass transfer limitations, the reaction kinetics, and the operating conditions. This should also examine the effect of circuit density on the mass transfer limitations, since different line spacings will result in varying degrees of etch undercut. This would be a valuable contribution, as experimental data of this nature in the literature are scarce.

Additionally, this extention would be useful for investigating nonuniform etching across the panel surface. While it was not a significant factor for the size of boards used in this work, larger panels do suffer from nonuniform etch rates in different regions on the board. This is due to additional mass transport limitations caused by puddles at the center of the board. At the edges, where drainage of the etchant solution occurs, there is a higher degree of contact with fresh etchant. A wide range of panel sizes should be used for the experimental investigation.

The control of the process is accomplished by defining the control objectives, which were taken to be a certain bottom line width on both sides of the panels, and using the available measurements to manipulate the process

inputs in order to reach these objectives. Conventional input-output methods have the problem of compensating for measurement noise. Deterministic model-based approaches are an improvement, but also have the problem of dealing with unmodeled process disturbances and modeling errors. The approach used for this process combined a deterministic model with a stochastic representation of the poorly known or unknown states and parameters. This was then used to design a Kalman filter for state estimation that combined the process model, all available measurements (regardless of precision or frequency), and information on the state probability distribution.

Several Kalman filter designs were developed and tested with the process model. A hybrid extended Kalman filter was found to yield biased estimates in the presence of process-model mismatch. This issue was resolved by augmenting the state vector with poorly known parameters and developing a proportional-integral Kalman filter. The same technique was used to develop a reduced order Kalman filter, which treated the bulk tank concentrations as stochastic processes. The resulting filter designs are capable of providing accurate estimates of the etching species concentrations as well as making available frequent estimates of the etch profile characteristics, which are only measured at infrequent intervals.

Based on the reduced order Kalman filter, a multivariable control strategy was "implemented" on the process model. The control system was able to maintain line widths at a 100 μm setpoint within ±2 μm. These results were found to be comparable to the ideal situation where frequent and accurate measurements of the etch profile were available, on which a control system can be based.

This is a blank page

APPENDIX

A

NOMENCLATURE

a_e	effective mass transfer area, cm^2/l
A_j	concentration of Cu^{2+} in unit j, mol/l
B_j	concentration of Cu^{+} in unit j, mol/l
BL	board length, cm
BLU	bottom line undercut, μm
BLW	bottom line width, μm
BSP	bottom spray pressure, psi
BW	board width, cm
C_0	liquid molar concentration, mol/l
Da	Damkoehler number
D_L	liquid phase diffusion coefficient, cm^2/s
E	oxidation-reduction potential (ORP), mV
E'	ORP at standard conditions, mV
F	Faraday's constant
F_{ij}	volumetric flow rate from unit i to j, l/min
F_B	total volumetric flow rate out of the bulk tank, l/min
F_{ij}^*	volumetric flow rate normalized by F_B
G	gas molar flux in regenerator, $mol/min/m^2$
H	Henry's Law constant, atm
k_{etch}	effective etch rate reaction constant, (cm/min)/(mol/l)
k_{LE}	effective lateral etch rate constant, (cm/min)/(mol/l)
k_{MT}	mass transfer coefficient, (cm/min)/(mol/l)

k_{regen}	regeneration rate constant
k_{rxn}	kinetic etch rate constant, (cm/min)/(mol/l)
k_R	equivalent first order regeneration rate constant, min^{-1}
k_{VE}	effective vertical etch rate constant, (cm/min)/(mol/l)
L_{Ei}	length of etcher i, m
MLW	mask line width, μm
MW	molecular weight of copper, g/mol
n	power of mass transfer power law
N	number of etcher/sump tanks in system
N_A	rate of cupric ions that goes into etching reaction, mol/min
n_L	number of lines on a board
N_{LE}	rate of copper removal by lateral etching, mol/min
N_{VE}	rate of copper removal by vertical etching, mol/min
P_0	pressure at regeneration column entrance, atm
PT	plating thickness, μm
R	ideal gas constant
r_{abs}	rate of absorption of oxygen, mol/min/cm^2
r_{etch}	etch rate, cm/min
r_{LEB}	lateral etch rate at bottom of line, cm/min
r_{LET}	lateral etch rate at top of line, cm/min
r_{regen}	molar regeneration rate per unit volume, mol/m^3/min
r_{VE}	vertical etch rate, cm/min
S_R	regenerator cross-sectional area, m^2
t_{BT}	breakthrough time when cavity bottom is cleared, min
t_{res}	residence time of boards in etch chambers, min
TLU	top line undercut, μ,
TLW	top line width, μm
TSP	top spray pressure, psi
u_{con}	conveyor speed, m/min
V_i	volume of unit i, l
V_i^*	volume of unit i normalized by bulk tank volume
y_{O_2}	mole fraction of oxygen in gas stream
z	height of regenerator, m
z_{BT}	breakthrough point, m

Greek

α	coefficient of mass transfer power law
α_{Ei}	ratio of liquid in etcher i to etcher volume
ε	void fraction in regenerator
ε_M	fraction of masked board surface
λ	relative gain
θ	etch angle
ρ	density of copper, g/cm^3
σ	standard deviation
τ	time normalized by bulk tank residence time

Subscripts

B	bulk tank
BS	associated with bottom side of boards
BT	breakthrough
D	dilution tank
Ei	etcher i, i=1, $\cdots$, N
F	corresponding to frequent measurements
IF	corresponding to infrequent measurements
R	regenerator
Si	sump tank i, i=1, $\cdots$, N
TS	associated with top side of boards

Vector Notation

$\mathbf{e}$	state estimate error vector
$\mathbf{F}$, $\mathbf{F_1}$	process model Jacobian matrix
$\mathbf{F_A}$	augmented process model Jacobian matrix
$\mathbf{f}$	process vector valued function
$\mathbf{f_2}$	process model vector valued function
Φ	state transition matrix
$\mathbf{G}$	observability test matrix
$\mathbf{G(0)}$	steady state gain matrix
$\mathbf{H}$	observation model Jacobian matrix

$\mathbf{H}_A$	augmented observation model Jacobian matrix
$\mathbf{h}$	observation model vector valued function
$\mathbf{I}$	identity matrix
$\mathbf{K}$	Kalman gain matrix
$\mathbf{K}_A$	augmented Kalman gain matrix
Λ	Information matrix
$\mathbf{n}$	measurement noise vector
$\mathbf{p}$	vector of stochastic parameters for state augmentation
$\mathbf{P}$	state covariance matrix estimate
$\mathbf{q}$	process noise sample vector
$\mathbf{Q}$	process noise covariance matrix
$\mathbf{r}$	observation noise sample vector
$\mathbf{R}$	measurement noise covariance matrix
$\mathbf{w}$, $\mathbf{w}_1$	process noise vector for original states
$\mathbf{w}_2$	process noise vector for augmented states
$\mathbf{x}$	state vector (order n)
$\mathbf{x}_A$	augmented state vector (order p)
$\bar{\mathbf{x}}$	state estimate vector
$\mathbf{z}$	observation vector (order m)

ABOUT THE AUTHOR

Alan Kao was born, never asked, on December 15, 1964. His life thus far can basically be separated into four different stages. There may have been more, but four is all that he can remember.

The first stage took place in Minneapolis, home of Prince, where he became the first and only son of Fa-ten and Betty Kao. This stage only lasted a couple weeks and he didn't remember very much. Shortly after his birth, his parents made the decision to move to Denver, Colorado. Since he couldn't walk or talk or function without their help, he went along.

For the next seventeen years, he lived in Denver. That's quite a long time and many things happened during this period. He learned to read and write. He learned to add and subtract. He learned how to "jinx" people. Over the course of time, he began to notice this peculiar "brown cloud" that had an annoying tendency to settle over the Denver skyline. This was particularly noticeable when driving back from the mountains, as it was such a striking contrast to the beauty of the Rocky Mountains. This stuck out in his mind, whereas much of his junior high and high school days he has forgotton.

In the fall of 1982, he entered the University of Colorado, located in the peaceful town of Boulder, where he had a very good time. He delivered pizzas. He waited tables. He sold cutlery. But he kept losing his keys and his wallet. It was during this stage that he began to realize that remembering things was

not something he was very good at. Subsequently, he switched from studying Molecular Biology, which is *all* memorization, to Chemical Engineering, whose teachers were kind enough to give open book exams. He liked this much better.

Eager to stay in school, he entered Lehigh University for graduate school in the fall of 1986. Swept away from the grandeur of the Rockies, he began to develop a deeper appreciation for little things. He became an avid hater of the Philadelphia Eagles. He discovered *Play It Again* and Rolling Rock. He enjoyed very much the charm of Bethlehem. While being a teaching assistant and working towards his Masters degree, he realized that he felt quite comfortable in the academic environment, so he took steps to further test this feeling. Upon completion of his MS, which involved an investigation of nonuniform etching in radial flow plasma etching reactors, he became a PhD candidate and sought out opportunities to teach. He taught two summer courses in Heat and Mass Transfer and also gave lectures on Air Pollution Control. He must have enjoyed these experiences, because upon graduation from Lehigh, his plans to pursue an academic career remain intact.

It's now time for the next stage. It's time for him to return to his earlier concerns with the polluted air that we breathe, and to do whatever he can to help improve the situation. Realizing that his name spelled backwards is "LA", he went there. What better setting for learning about air pollution? This is where stage five begins...

Mother Earth spoke to me and said I must wear very large, heavy sandals whilst I tread upon her.

---- Lauton